Molecular dynamics simulations of the electrical conductivities of high temperature metallurgical slags

Lehlohonolo Mongalo

University of Cape Town

February 2018

Molecular dynamics simulations of the electrical conductivities of high temperature metallurgical slags

a thesis submitted to the

University of Cape Town

in fulfilment of the requirements for the degree of

Doctor of Philosophy

by

Lehlohonolo Mongalo

Supervisor: Dr Gerhard A. Venter

Co-supervisor: Dr Anton S. Lopis

Department of Chemistry and

Scientific Computing Research Unit

University of Cape Town

South Africa

DECLARATION

I declare that the thesis "Molecular dynamics simulations of the electrical conductivities of high temperature metallurgical slags" is my own unaided work, both in concept and execution, and that apart from the normal guidance from my supervisors, I have received no other assistance. Neither the substance nor any part of this thesis has been submitted in the past, or is being, or is to be submitted for a degree at this university or at any other university.

Signed. Signed by candidate

Date: 01 February 2018

ACKNOWLEDGEMENTS

First, and most of all, I would like to express my sincere gratitude and appreciation to my supervisors Dr Gerhard A. Venter and Dr Anton S. Lopis for their guidance and constant support during the work of this doctoral thesis. I am grateful to Dr Quinn Reynolds for his comments and help with both technical and theoretical concerns during this project. I would like to thank the Center for High Performance Computing (CHPC) for computational resources and Dr Happy Sithole for letting me use CHPC office space. This work is based on research supported by the National Research Foundation (NRF) (grant no. IFR1203100525) and funded through a DST–NRF Professional Development Program (PDP) scholarship awarded to LM and hosted by Mintek. Special thanks to Dr Raji for fruitful discussions and valuable comments. Finally, I would also like to thank my family for their support.

PUBLICATIONS, CONFERENCE CONTRIBUTIONS AND AWARDS

Journal Articles

- L. Mongalo, A. S. Lopis and G. A. Venter, Molecular dynamics simulations of the structural properties and electrical conductivities of $CaO–MgO–Al_2O3–SiO_2$ melts. *J. Non-Cryst. Solids*, **2016**, 452, 194-202

- L. Mongalo, A. S. Lopis and G. A. Venter, Development of an Artificial Neural Network Model for the Prediction of $CaO–MgO–Al_2O_3–SiO_2$ Melt Ionic Conductivities, *in preparation*.

Conferences (Oral Contribution)

- L. Mongalo, A. S. Lopis and G. A. Venter, Atomistic Simulation of Pyrometallurgical Slags, *CHPC Research Day*, 16 October 2015, Pinelands, South Africa.

Conferences (Posters)

- L. Mongalo, A. S. Lopis and G. A. Venter, High Temperature Atomistic Simulation of Pyrometallurgical Slag Systems, *CHPC National Meeting*, 1-5 December 2014, Kruger National Park, South Africa.

- L. Mongalo, A. S. Lopis and G. A. Venter, High Temperature Atomistic Simulation of Pyrometallurgical Slag Systems, *CHPC National Meeting*, 2-6 December 2013, Cape Town, South Africa.

- L. Mongalo, A. S. Lopis and G. A. Venter, High Temperature Atomistic Simulation of Pyrometallurgical Slag Systems, *CHPC National Meeting*, 3-7 December 2012, Durban, South Africa.

ABSTRACT

The structural properties and electrical conductivities of nine $CaO-MgO-Al_2O_3-SiO_2$ slags with compositions in the peralkaline region have been calculated using molecular dynamics simulations. Where applicable, results were compared to those estimated from composition data alone. The proportion of nonbridging oxygen (NBO) and bridging oxygen (BO) atoms were determined from simulation and shown to be in reasonable agreement with theoretical prediction, with the number of NBOs increasing as the number of network modifying cations increase. Bridging oxygen atoms were classified into Si−O−Si, Si−O−Al or Al−O−Al linkages and the results used to establish whether the Al avoidance principle is applicable. Consistent with experimental and simulation results reported elsewhere for aluminosilicates, a surprisingly large number of fivefold–coordinated Al atoms were found, even though the simulated compositions contain CaO and MgO far in excess of the tectosilicate join. The number of bridging oxygens coordinated to tetrahedral $[SiO_4]^{4-}$ and $[AlO_4]^{5-}$ units, namely the Q^n distribution, was determined. Although a good comparison to the theoretical average Q was found at low basicity, at higher basicity greater deviation was seen. Finally, electrical conductivities calculated using the Einstein relation, taking cross–correlations into account, were in excellent agreement with experimentally measured values, although Nernst–Einstein conductivities, estimated from self–diffusion coefficients alone, showed large deviations. In doing these calculations, it is implicitly assumed that the total electrical conductivity of the slags results from motion of the ions alone and that there is no electronic component to the conductivity. Results therefore show that molecular dynamics simulations are able to reliably predict conductivity, but values calculated indirectly, i.e., using the Nernst–Einstein relationship, should be used with care. At low basicity theoretical predictions of structural disorder, based on Zachariasen's Random Network Model, are in reasonable agreement with simulation, but this agreement worsens as the proportion of network modifying cations increases. Artificial neural network (ANN) models for predicting electrical conductivities of slags, based on structural properties, were also successfully developed. Two layer multilayer perceptron (MLP) feedforward ANN models, using the resilient back propagation algorithm for training, were used to predict conductivities. The input and output parameters were calculated using molecular dynamics (MD) simulations and different combinations of input parameters, as well as number of hidden neurons, were used to find the best model. The best models were identified based on having low MSE errors, when applied on a test data set for

which experimental results are known. Using a subset of structural parameters (average Q^0, Q^1 distributions and the number of NBO atoms) yielded the best model with an MSE of 6.8 $(S/m)^2$. More general models using a greater set of structural parameters had MSEs in the range of 33.0 to 35.2 $(S/m)^2$. The artificial neural network models have demonstrated a reasonable agreement in predicting the MD calculated electrical conductivities of slags and hence, proved to be effective methods for the prediction of electrical conductivities of slags using structural properties as input parameters.

TABLE OF CONTENTS

AIMS AND OBJECTIVES

With respect to electrical conductivities, there is a lack of reliable data for slags due to the difficulties of performing high temperature measurements. In the optimization of a pyrometallurgical process, the electrical conductivity of slags is of great importance since the power supply requirements for the electric smelting process depend on knowing the electrical conductivities of these systems. The aim of this project is therefore to calculate electrical conductivities of metallurgical slags using molecular dynamics (MD) simulations and develop a general electrical conductivity model for CaO-MgO-Al_2O_3-SiO_2 (CMAS) slags based on structural properties of the silicate melt. The first objective of this work is to understand the relationship between the structural properties of slags and its transport properties and develop a reliable protocol for the calculation of electrical conductivity. The next objective is then to build on this information and developing computational tools (an artificial neural network) for slag properties (conductivity, in this case, but can be extended to other properties as well) that could provide reliable and mutually consistent data for the benefit of the South African mining industry.

The ionic conductivities were calculated in two ways, i.e., using an exact method based on the correlation function of the current density, where electrical conductivities take cross-correlations between atomic motion into account and the so-called Nernst–Einstein conductivities, which are based on diffusion coefficients alone with the assumption that ions migrate independently. Throughout this work, the electrical conductivity were taken to result solely from the ionic motion, with no electronic contribution. Once it has been shown that the electrical conductivities can be calculated with accuracy, it should be possible to establish a correlation between the transport and structural properties. The first successful theory of aluminosilicate melt structure, the Continuous Random Network (CRN) model, is well established and provides some broadly applicable conclusions that suggest a correlation between structure and transport properties (e.g., viscosity and conductivity) should exist. Thus, it should be possible to exploit the ease with which the structural properties can be calculated using MD and use this data to predict electrical conductivities using a machine learning approach, in particular using an artificial neural network model (ANN). Machine learning algorithms are able to build non-linear relationships and are successful in situations where clear relationships between variables are not evident. This also enabled generation of consistent structural and electrical conductivity data for complex slag systems.

The development of the electrical conductivity artificial neural model used structural properties calculated using MD simulations as input parameters, with a resilient back-propagation procedure for determining model parameters. In all cases, the models used the conductivity as the output variable and a combination of different structural properties as input variables. Combinations of different input variables helped to identify those parameters that best predict experimental electrical conductivities. The quality of the model were judged by how well it predicts experimentally measured electrical conductivities, where available. Particular attention was given to finding the minimum, or optimal, number of hidden layers and nodes required for a neural network to replicate experimental data. The scope of this research was limited to a defined range of slag compositions.

1. INTRODUCTION

The drive over the years to reduce energy consumption, improve environmental impact and cut cost by the smelting industry, has highlighted the need for understanding the properties of slag systems. Proper control of slag chemistry is a crucial part of modern smelting practice in order to optimise the process and drive cost cutting measures. In this regard understanding the relationship between composition and transport properties, such as conductivity, is one of the most important factors in the physical chemistry of slags. In this work, the link between structure and transport properties (electrical conductivities) at the molecular level was illustrated. The introduction therefore starts with a brief description of slags followed by the introduction into ores and oxides used in mineral processing. The ores and calcination process are first discussed. Then the iron and steel processing routes which takes place in the blast furnace (BF), basic oxygen furnace (BOF) and the electric arc furnace (EAF) are introduced. The reduction smelting, refining process and smelting by product are discussed in the context of BOFs and EAFs. The phases present in slags and electrical conductivity are discussed next. Finally, the modelling techniques applied to slags are discussed.

1.1. Metal Oxides and Natural Ores

Metals are produced from natural ores. The raw ores are extracted from the earth by blasting with explosive and used in the metal making process. The ores are crushed and ground into smaller pieces that range between 0.5 and 1.5 inches, in order to liberate the valued minerals from the host rock (Saheb 2012). The raw material used to produce steel is iron ore, which usually contains the mineral hematite (Fe_2O_3) and may also contain magnetite (Fe_3O_4). Aluminium metal is produced from the bauxite ($AlOH_3$), which is a hydroxide ore and one of the most abundant found in the earth's crust. Silicon is produced from quartz (SiO_2). Copper and nickel metals on the other hand, are produced mainly from sulphide ores. Other metals that are derived from sulphide ores include silver, gold, platinum, zinc, lead, mercury and molybdenum, as well as metalloids such as arsenic, antimony, selenium and tellurium. Sulphide ores often contain a mixture of copper sulphides and iron in small quantities. Iron can also be obtained from sulphide ores in the form of pyrite (FeS_2), but this serves only in exceptional circumstances as a source of iron in industry. In addition, the earth's crust also contains crystalline sulphide ores, which contain a number of different minerals such as chalcopyrite ($CuFeS_2$), sphalerite (Zn, Fe)S, galena (PbS) and silicates or other gauge minerals.

Since these ores typically contain a mixture metals, they are usually first treated to separate the different minerals, to give separate concentrates of copper, zinc, iron and lead, as well as to discharge the worthless gangue minerals (Rosenqvist 2004).

1.2. Refractory preparation (Calcination)

Before the production of any metal, there are pre-processing steps that are necessary before ores are charged into the furnace. One of these is the preparation of refractory oxides in the iron-making process. A number of decomposition reactions are important in metallurgy, e.g., the calcination of calcium carbonate, limestone and dolomite to oxides, which are used as refractory oxides. CaO is produced by calcination of limestone (primarily $CaCO_3$) in rotary, shaft, or rotary hearth–type kilns. The calcination reaction is given below:

$$CaCO_3 + \text{Heat} \rightarrow CaO + CO_2 \qquad \text{at } 827\ ^oC \qquad (1)$$

The calcination of limestone produces lime containing about 96 wt. % CaO, 1 wt. % MgO, and 1 wt. % SiO_2. An enormous amount of calcinated or burnt lime is charged into the BOF within a short period of time, which requires a careful selection of the lime quality to improve its reactivity (dissolution) in the slag (Li, Whitwood et al. 2014). The reactivity of lime with the slag promotes quick formation of a suitable slag, which could increase the process productivity and improve the steel quality at reduced cost. The general requirements for fluxing oxides is for the limestone to consist of small lump sizes, of about ½–1 inch, having high porosity, which promotes higher reactivity and rapid slag formation. It is common to have stone with uncalcined inner cores, excess fines and too low a reactivity resulting in quality problems in limestone. Magnesite (magnesium carbonate) is a source of magnesium oxide (MgO). When calcined, it decompose according to the following reaction:

$$MgCO_3 + \text{Heat} \rightarrow MgO + CO_2 \qquad \text{at } 827\ ^oC \qquad (2)$$

CaO and MgO can also be derived from the calcination of dolomite, which proceeds according to the following reactions:

$$CaCO_3{\bullet}MgCO_3 \rightarrow CaCO_3{\bullet}MgO + CO_2 \quad \text{at } 700–850\ ^oC \qquad (3)$$

$$CaCO_3{\bullet}MgO \rightarrow CaO{\bullet}MgO + CO_2 \quad \text{at } 850–950\ ^oC \qquad (4)$$

Typically, dolomite contains about 36–42 wt. % MgO and 55–59 wt. % CaO (Barker, Paules et al. 1998). When charged into the furnace, it saturates the slag with MgO, which leads to an increase of the slag viscosity that reduces the dissolution of furnace refractories into the slag, i.e., protects the furnace lining against a corrosive environment.

1.3. Iron making processes in a Blast Furnace (BF)

The purpose of a blast furnace (BF) is to chemically reduce and physically convert iron oxides into liquid iron, called hot metal or pig iron. Furnace constituents such as oxides, which come in the form of lumpy raw ore, pellets (small particles typically created by compressing original material) or sinter (high temperature fused powder), together with coke (a source for carbon in which all the volatile constituents in coal have been eliminated), dolomite, and limestone are charged from the top into the blast furnace in alternating layers in a continuous way. Once all the raw materials are in the furnace, heated air at supersonic speed is blown in through nozzles at the bottom of the furnace. The air burns the coke, which produces heat that is a requirement for the chemical reactions in the furnace and also to melt the ores. In addition, the carbon is oxidised to carbon monoxide. This is a critical reaction in the smelting as it is effectively the driving mechanism for the smelting process since sufficient thermal energy is generated to permit the oxidation process to self-propagate without additional external heating.

The melting process is called smelting, i.e., it is the metallurgical process of extracting metals from their ores, this is achieved by heating to higher temperatures in a furnace where melting and chemical reaction of furnace constituents takes place. The coke and carbon monoxide also reduces the iron ore into metallic iron and slag is formed from the gangue of the ore burden and the ash of coke and coal. This process is called reductive smelting as it takes place under reductive environment. The reduction of iron oxide is the most important reaction in metal production, since the production of iron occupies more than 90% of the tonnage of all metals produced (Seetharaman 2005). As mentioned earlier, iron ore occurs in nature predominantly as hematite (Fe_2O_3). In the blast furnace, hematite undergoes sequential reduction reactions by carbon monoxide, as shown in equation 5 - 7. It is step wise reduced to magnetite, wüstite and finally metallic iron, which melts and is tapped at the bottom of the furnace. The blast furnace diagram is shown in Figure 1.

$$3Fe_2O_3 + CO \rightarrow 2Fe_2O_4 + CO_2 \quad (5)$$

$$Fe_2O_4 + CO \rightarrow 3FeO + CO_2 \quad (6)$$

$$FeO + CO \rightarrow Fe + CO_2 \quad (7)$$

The resulting hot metal is then transported to the steelmaking plant to make steel, but before that, is has to undergo temperature and chemical adjustment. There are two main steelmaking

routes, these are the basic oxygen furnace (BOF) and an electric arc furnace (EAF) and were discussed next.

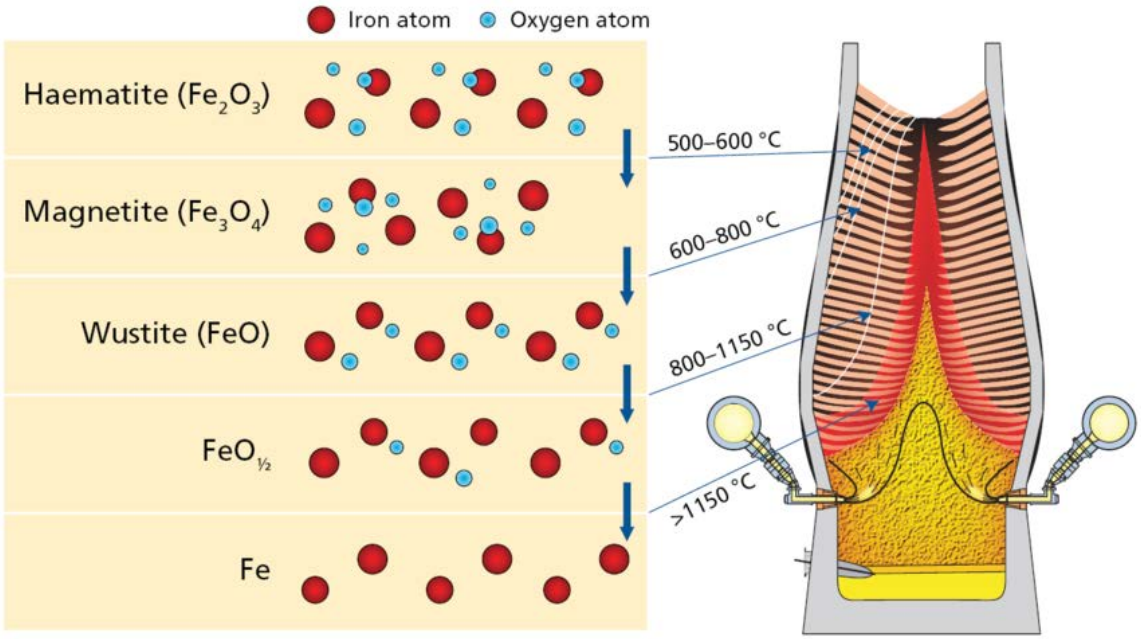

Figure 1: Reductive smelting of iron ore in the blast furnace (Geerdes, Chaigneau et al. 2015).

1.4. Steel making in a Basic Oxygen Furnace (BOF)

In the basic oxygen furnace steel making route, the liquid iron from the BF is charged with steel scrap into the BOF, also known as an oxygen converter. Once all the hot metal has been charged into the furnace, high purity oxygen air at supersonic speed is blown onto the surface of the iron bath through a water-cooled lance, which is suspended in the vessel and kept a few meters above the bath. This converts the hot metal into the crude steel. This process also oxidises some of metallic inclusions to form oxides. The non-metallic inclusions from oxidation are removed by being transported to the steel-slag interface, dissolve into the slag phase or separate across the interface. This steel processing route is named the BF-BOF. The hot metal that is charged into BOF is also subjected to the pre-treatment process (refinement) to remove impurities. These impurities are from iron ore, ash from the coal and refractory oxides, they are retained in hot metal therefore need to be removed. The pre-treatment (refinement) of hot metal can also be done in the BOF or externally in in the ladle furnace, tundish and continuous casting mould. The refinement process is discussed in in detail section 1.6.

1.5. Steel making in an Electric Arc Furnace (EAF)

An alternative method of making steel is through an electric arc furnace (EAF), using scrap metal. The carbon, lime and dolomite are normally charged with scrap metal into the EAF and heated to a liquid phase with an electric current. This melting of scrap and other constituents is called smelting. The slag then floats on top of the denser metal layer as in the BF and BOF. The EAF operate as follows: the electrode is lowered to strike an arc on the scrap and ores in the furnace, resulting in the melting of the furnace contents. The electrical energy is supplied via graphite electrodes, resulting in very intense mass and energy transfer, making this the largest contributor to in the melting operations. Plasma arc (a high-temperature ionised gas-like material) supplies the energy required for chemical reactions taking place in the EAF. The high turbulent conditions under the arc also promotes good mixing and fairly uniform temperature distribution across the molten bath of the furnace. The temperature of the plasma arc is somewhere between 10 000 and 20 000 °C. Once the ores or the recycled scrap have been melted, further processing is required to remove unwanted impurities as in the case of the BOF steelmaking. The EAF can either be alternating current (AC) or direct current (DC). The DC arc furnace as shown in Figure 2 is made up of a cylindrical steel shell that is lined with refractory materials just like other furnace designs. It has a central vertical graphite electrode that passes through the roof. The anode part of the furnace is embedded in the hearth at the base of the furnace where the metal layer is in direct electrical contact with the anode.

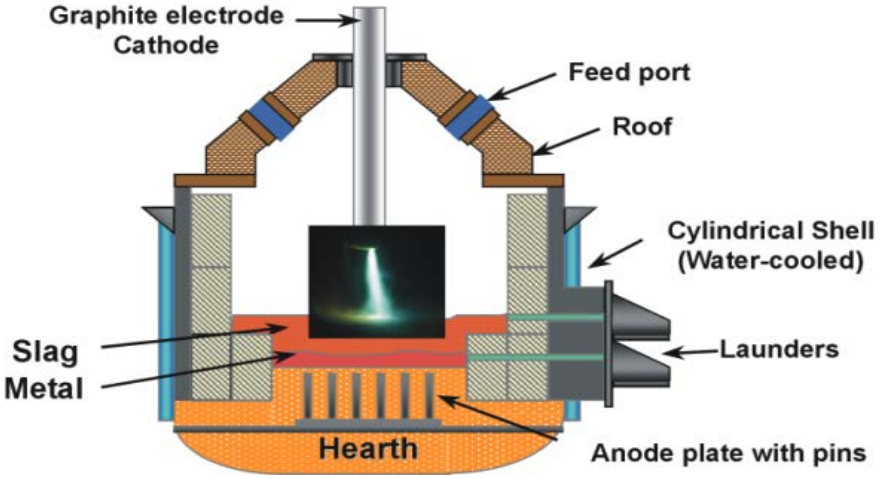

Figure 2: Schematic of the direct current (DC) electric arc furnace (Jones 2016).

1.6. The refining process

Once all the furnace charge has fully melted, the next processing step is refining. During this process, the final adjustment of steel properties is carried out. This involves controlling temperature and composition to meet the final steel specifications. Generally, in steel making process the elements that are removed are phosphorus, sulphur, aluminium, silicon, manganese and carbon. However, for most steelmaking refining in the EAF is limited to dephosphorisation, decarburisation, and temperature adjustment to produce specified steel type. The presence of impurities is detrimental to the quality of steel when present in high concentrations, therefore need to be reduced to accepted levels. It is normal to reduce the impurities to be lower than specification, alloying additions can be made later in the ladle to raise the composition to desired levels. Most of the impurities have higher affinity for oxygen, therefore oxygen preferentially react with these elements to form metallic oxides which end up floating out of steel into slag. The oxidation involves lancing oxygen directly into the molten metal bath as shown in Figure 3. The removal of silicon, phosphorus, manganese and carbon is mainly through oxidation processes.

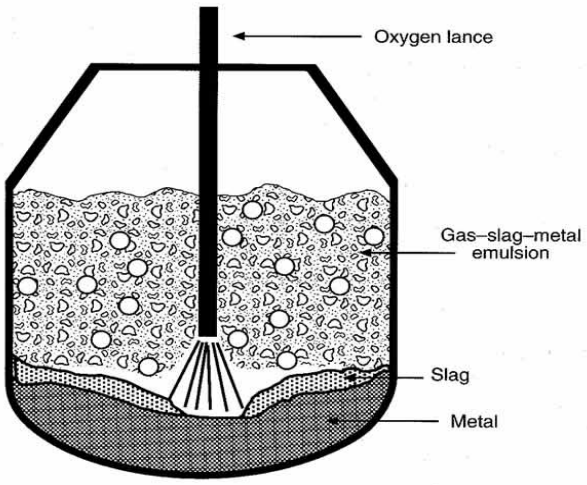

Figure 3 *:* **Schematic of the oxidation process during steel making process (Barker, Paules et al. 1998).**

1.7. By-products of the smelting process

Iron and steel slag is produced as the nonmetallic by-product of iron and steel production. Slag is made from the meltdown liquid of sinter, gangue material, lump, coke and flux. Slags is classified according to the type of process from which is produced: Blast Furnace (BF) iron slag, Basic Oxygen Furnace (BOF) steel slag, and Electric Arc Furnace (EAF) steel slag. In all

the three slag types, they are made up of metal oxides, powders and other furnace impurities used during the iron and steelmaking process. The primary constituents for BF slag is silica and alumina from the original ore with calcium and magnesium oxide from the added flux. Similarly, the slag compositions from the both BOF and EAF processes also contains fluxing agents and thus the chemical composition of slag from these processes is similar to BF slag. However, the BOF and EAF slags contains substantially higher amounts of iron and manganese contents. On cooling down of the slag, the metallic component is removed and fed back into the steel mill.

1.8. Heat transfer and distribution from the electrodes to the slag

The EAF steelmaking route is primarily based on recycled steel scrap where the electric energy is used to melt the contents of the furnace (Jones 2016). The slag is the most resistive part of the furnace constituents. The power supply requirements of many electric smelting processes are therefore determined by the electrical conductivity of the slag (Jones, Reynolds et al. 2011). The wrong specification of the power supply requirements can add to process cost that arise because of the need to purchase a new transformer. In addition, accurate prediction of the electrical conductivity of the slag prevent unnecessary over-conservative specification of power supply requirement that guarantee operation over a wide range of conditions. As a result of these factors, the ultimate success of the smelting process depends on accurate prediction of conductivity and the required voltage across the slag before specifying power supply of the new industrial furnace. The electrical resistance of the slag decreases as the charge becomes molten since the conductive path is created for the current flow between the electrodes. The slag resistivity in the furnace is much higher than that of the matte layer. This makes the slag a major source of heat generation within the furnace, which is also known as Joule or Ohm heating (Robiette 1973). For proper heat transfer, slag must meet certain physical and chemical requirements. Slag thickness plays a crucial role in controlling transfer within the furnace. A too thin slag is not desirable, as it would cause electrodes to be positioned too close to the matte layer, resulting in electrical current to pass on the matte layer leading to possible overheating of the hearth. On the other hand, a thick slag is desirable, as it allows deeper immersion of the electrodes, leading to a reduction in micro-arc resistance and enhanced higher energy release within the bath. However, excessively thicker slag is not desirable as leads to precipitation of the higher melting components in the lower, cooler layers of the slag. Heat transfer in the furnace must also be adequate in order for the slag viscosity to be low enough to allow metal droplets to pass through it and settle. The viscosity of the slag is a function of temperature and

composition, too low temperature results in low viscosity and too high temperature results in the opposite effect.

1.9. Oxide phases and phase diagrams

The phase relationship as a function of temperature and composition plays a crucial role in understanding the chemical and physical properties of slags. Slag systems can form multiple complex phases that can be presented in terms of a phase diagram. Phase diagrams convey a variety of thermodynamic data through equilibria among multiple phases as well as quantitative data on phase distributions in a specific system. Phase diagrams can represent the individual pure component oxides, binary systems, ternary systems, quaternary systems, and quinary systems. Basic features and interpretation are common to all diagrams, but the complexity increases with the number of components present. The slag system of interest in this work is a four component (quaternary) system, which is normally simplified by using a regular tetrahedron, with each corner representing one pure component. The tetrahedron is the basic structural unit of the slag system. The boundaries between surfaces represent two or more phases that coexists within the system, and the meeting of the different surfaces or regions in a point gives rise to an invariant point where two or more phases coexist and are in equilibrium.

Certain silicate minerals melt incongruently, i.e., upon heating they decompose to form another crystalline or amorphous phase plus a liquid, neither of which has the same composition as the original silicate. The compounds with incongruent melting points may have great significant in the properties slag melt such as transport properties (viscosities and electrical conductivities). In general, the knowledge of the thermodynamic properties of slags, including phase relations, can lead to an improved understanding of the smelting process and metal recovery.

1.10. Example of a binary phase diagram

In this section, a typical phase diagram is shown to illustrate the appearing of different macroscopic phases. Figure 4 is the equilibrium binary phase diagram for the $MgO\text{-}SiO_2$ system, showing the stabilities of solid and liquid phases as a function of temperature and composition. The invariant points are given in Table 1. The phase diagram is characterized by a fairly large liquid area over a wide temperature range and composition. The two crystalline phases pyroxene ($MgO\text{-}SiO_2$) and olivine ($2MgO\text{-}SiO_2$), formed by the binary $MgO\text{-}SiO_2$ system, are shown on the composition axis in the phase. At 1470 °C, pyroxene decomposes to form enstastite and tridymite crystal, upon heating to 1543 °C, it further decomposes to protoenstatite and cristobalite.

The cristobalite crystal and liquid coexists at 1659 °C, further heating to temperature above 1659 °C, the liquidus curve of cristobalite rises to the invariant point at which two liquid phases coexist in a silica rich region. The pyroxene melts incongruently to form forsterite and a more silicious liquid at 1557 °C, and becomes completely liquid on the forsterite liquidus curve. Olivine decomposes to periclase and forsterite below 1850 °C. Above 1850 °C, the olivine melts incongruently to form an MgO crystalline phase and a liquid richer in SiO_2.

Table 1: Invariant points in the MgO-SiO_2 binary system at different temperatures and compositions

Phase reaction	Temperature	Composition of liquid (%wt.)	
	°C	MgO	SiO_2
$MgO + 2MgO\text{-}SiO_2 \rightarrow L^{\dagger}$	1850	62.0	38.0
$2MgO\text{-}SiO_2 \rightarrow L^{\dagger}$	1890	57.3	42.7
$MgO\text{-}SiO_2 \rightarrow 2MgO\text{-}SiO_2 + L^{\dagger}$	1557	39.2	60.8
$MgO\text{-}SiO_2 + SiO_2$ (cristobalite) $\rightarrow L^{\dagger}$	1543	35.2	64.8
SiO_2 (cristobalite) $+L2^{\dagger} \rightarrow L1^{\dagger}$	(L1)1695	30.5	69.5
SiO_2 (cristobalite) $+ L2^{\dagger} \rightarrow L1^{\dagger}$	(L2) 1695	0.8	99.2

$^{\dagger}L$, L_1 and L_2 are liquid phases

The phase diagrams for other binary and higher order component (ternary, quaternary and quinary) systems can be interpreted or discussed in a similar manner as the above systems.

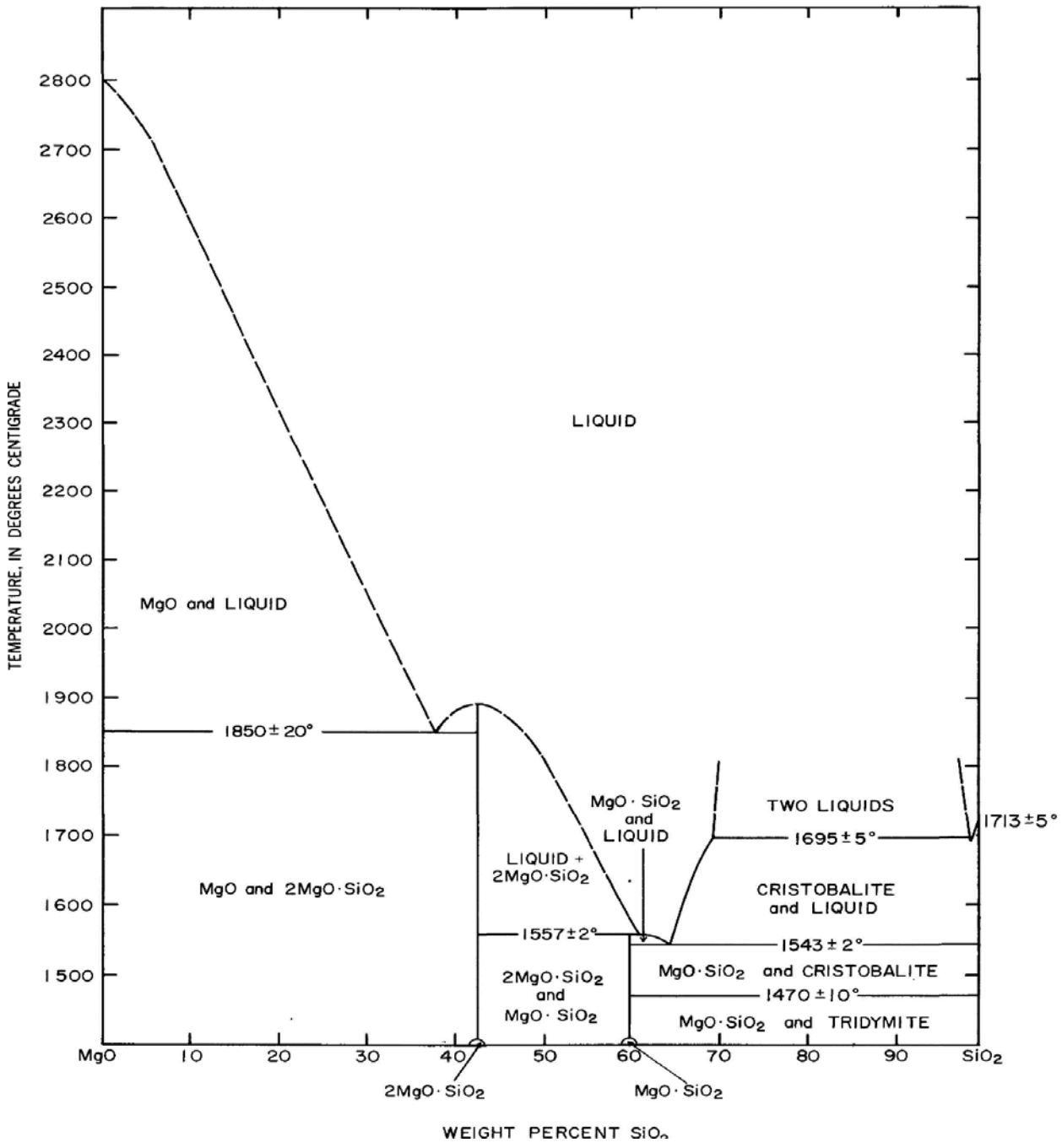

Figure 4: Phase diagram for the MgO-SiO_2 system (Fleischer 1962) .

1.11. Electrical conductivities of slags

The electrical conductivity in silicate melts is usually associated with the movement of cations while electronic conduction in systems with transition metals are also possible (as described in Section 1.12). Cations undertake the duty of transporting charge with an electric field applied and thus contribute to the electrical conductivity. The suspended clusters in the form of anions in silicate melts are polymeric, and do not move readily, therefore contribute less to the electrical conductivity of the slags. The electrical conductivity of molten silicate slags can be

affected by the presence of second phase or mixed phases which are functions of composition and temperatures. Above the liquidus temperature where there is no presence of a second phase, the conductivity of slags is expected to be higher as there is little or no hindrance to the movement of cations due to a decrease in the degree of polymerisation. Below the liquidus temperature where solid phases or regions with mixed phases are likely, the conductivity is likely to decrease because of the formation of a solid phase which hinders the movement of cations. Such a solid phase can impede the movement of conducting cations. Bockris et al. (Bockris, Kitchener et al. 1948, Bockris, Kitchener et al. 1952) studied the electrical conductivity of various binary silicate slags above and below their liquidus temperatures in order to determine the changes in electrical conductivity of melts during solidification. The electrical conductivity in the liquid phase was found to be higher than in the phase occurring below liquidus temperature (Bockris et al. 1952). Decreases in electrical conductivity below the liquidus temperatures were believed to be a result of the locking up of conducting cations during the formation of crystal lattices in the solidification process (Bockris, Kitchener et al. 1952). Generally, the relationship between electrical conductivity and temperature can be expressed in terms of the Arrhenius equation:

$$\ln \sigma = \ln A - E /(RT) \quad (8)$$

where σ is the electrical conductivity in S/m , A is a constant, E is the activation energy in J/mol, R is the gas constant, which is equal to 8.314 J/(mol K), and T is the absolute temperature in Kelvin.

The electrical conductivity of melts are composition and structure dependent. The accurate collection of electrical conductivity data is difficult since individual conductivity measurements are rarely published. Some results are presented as either equations (typically with an Arrhenius fit) or graphically and are therefore difficult to extract. The conductivity values reviewed here are those presented in the literature, either in tables or mentioned explicitly in the text. The conductivities that were reviewed are for pure, binary, ternary and quaternary slag systems.

1.11.1. CaO, MgO, Al_2O_3 and SiO_2 slag systems

The electrical conductivities for pure CaO, MgO, Al_2O_3 and SiO_2 are shown in Table 2. The electrical conductivities for CaO and MgO were reported Van Arkel et al. (Arkel, Flood et al. 1953). Multiple measurements for the conductivity of molten alumina (Al_2O_3) has been reported

by various authors. The electrical conductivity of pure liquid alumina was reported to range from around 0.8 to 1.3 S/cm, at temperatures from 2150 to 2500 °C respectively (Mills et al. 1995). On the other hand, measurements by Arkel et al. (Arkel, Flood et al. 1953) and Fay (Fay 1966) gave conductivities of 15 S/cm and 3.84 S/cm, respectively, at a temperature of approximately 2050 °C. Mackenzie (Mackenzie 1962) suggested that pure alumina is an ionic conductor, based on the low conductivity of the solid phase and sudden large increase in conductivity on fusion. There are few electrical conductivity values available in literature for liquid silica (SiO_2). The conductivity for this system over a wide range of temperature was measured by Panish (Panish 1959). The values range from approximately 10^{-5} to 10^{-4} S/cm, in the temperature range 1000 to 2700 °C.

Table 2: Electrical conductivity of pure oxides

Oxide	T (°C)	(Sm^{-1})
CaO	2580	40†
MgO	2800	35†
Al_2O_3	2050	15†
Al_2O_3	2150 – 2500	0.8 – 1.3‡
Al_2O_3	2050	3.84
SiO_2	1000 – 2700	10^{-5} – 10^{-4}

† van Arkel et al. 1953

‡ Mills et al. 1995

 Fay 1966

 Panish 1959

1.11.2. CaO-SiO_2 slag systems

The electrical conductivities of the CaO-SiO_2 systems have been reported by Mori and Matsushita (Mori and Matsushita 1952) , Bockris et al. (Bockris et al. 1948) and Keller et al. (Keller et al. 1979) in temperate ranges of 1400–1600, 1700 and 1500–1600 °C, respectively. Mori and Matsushita (Mori and Matsushita 1952) reported conductivities ranging from 0.1–1 S/cm while Bockris et al. (Bockris et al. 1948), higher conductivities ranging from 0.25–0.44 S/cm. Both authors observed an increase in electrical conductivities of these slags with increasing amounts of the basic oxide CaO. The increase in conductivity may be attributed to the fact that an increase in the basic oxide content results in a decrease of the degree of polymerisation leading to an increase in the movement of the metal cations which enhance

conductivity. Keller et al. (Keller et al. 1979) measured the electrical conductivity as a function of SiO_2 (0.634–0.448 wt.%) composition. The conductivity ranged from 0.108–0.456 S/cm in the temperature range of 1500 –1600 °C. According to (Keller et al. 1979), the electrical conductivity for the CaO-SiO_2 slags decreases with increasing silica content, due to an increase in the degree of depolymerisation resulting in an increase in the resistance to movement of cations.

1.11.3. MgO-SiO_2 slag systems

The electrical conductivity measured by Bockris and Potter (Bockris and Potter 1952) for four compositions increased from 0.34 to 1.00 S/cm, with MgO content ranging from 38.5 to 55 mol %, at 1750 °C. The addition of MgO would bring about depolymerisation of the silicate network and hence increase the conductivity.

1.11.4. CaO-MgO-SiO_2 slag systems

The measurements on the electrical conductivity of CaO-MgO-SiO_2 slags have been carried out by a few research groups. Schiefelbein and Sadoway (Schiefelbein and Sadoway 1997) studied two compositions denoted M and S at 1500 °C, where M is 50.95CaO-12.51-MgO-36.54-SiO_2 and S is 24.59-CaO-26.15-MgO-49.26-SiO_2. The conductivities measured for these compositions are shown in Table 3. The conductivities obtained by Kawahara et al. (Kawahara, Ozima et al. 1978) were higher than those from Schiefelbein and Sadoway (Schiefelbein and Sadoway 1997). The two groups of researchers used different techniques to measure electrical conductivities, and this might be the reason for significant differences between their results. It should be noted that the conductivities of basic oxide melts were found to be higher than those of acidic oxide melts by both groups. This is consistent with what is stated earlier – that is an increase of basic oxides promotes depolymerisation of a melt leading to an increase in electrical conductivity. Daněk and Ličko(Daněk and Ličko 1983) also substituted the CaO with MgO in the CaO-MgO-SiO_2 system and concluded that this only resulted in a slight decrease in electrical conductivity.

Table 3: Electrical conductivities of the CaO-MgO-SiO_2 system (Schiefelbein and Sadoway 1997 and Kawahara, Ozima et al. 1978)

Melt composition	Kawahara et al. (S/cm)	Schiefelbein and Sadoway (S/cm)
M	0.70	0.49
S	0.45	0.21

1.11.5. CaO-MgO-Al_2O_3-SiO_2 slag systems

The slag of interest in this thesis is the CaO-MgO-Al_2O_3-SiO_2 (CMAS) quaternary system. The electrical conductivity for this system has been studied by several researchers. The data of Adachi and Ogino (Adachi and Ogino 1957) , Rennie (Rennie 1972) and Sarkar (Sarkar 1989) are for high alumina containing slags ranging from 10 to 20 mol%. While data of Winterhager et al. (Winterhager et al. 1966), Nesterenko and Khomenko (Nesterenko and Khomenko 1985) were for slags with lower alumina contents (up to 3 mol%). Generally, the electrical conductivities for these systems increase with increasing basicity (Hundermark 2003, Wang, Wang et al. 2016). The ionic conduction in the silicate melt increases with increasing Ca^{2+} and Mg^{2+} content. This is because the disruption of the polymeric network with addition of the metal cations leads to enhanced mobilities of the cations and therefore greater electrical conductivity. Mills (Mills 1995) compiled and reviewed most of the published data on electrical conductivity of various slag systems, and hence the reader is referred to his comprehensive review. From this review, it becomes clear that developing predictive models for electrical conductivity is extremely advantageous due to the difficulty and significant random deviations of experiments.

1.12. Electronic conductivity

Some slag systems may have a significant electronic contribution to their electrical conductivity. The electronic conductivity arises as a result of electron exchange between transitional metal ions of differing valencies e.g., Fe^{2+} to Fe^{3+}. This is the case for some slags that contain transition metal oxides, where one needs to take into account the relative numbers of such metal cations present, the basicity and the oxidation states of such metal ions. Dickson and Dismukes (Dickson and Dismukes 1962) studied the electrical conductivity of FeO-CaO-

SiO_2 slag melts with a relatively low concentration of FeO. Owing to the lower conductivity in this system, it was concluded that the conductivity was essentially only ionic in nature. At sufficiently high levels of iron oxide, an increase in conductivity was attributed to electronic contributions and was reported to vary with the oxidation state (Hundermark, 2004, Jiao, 1988). Manganese slags have been studied by Jahanshahi (Jahanshahi 2004), and an increase of MnO oxide concentration was observed to lead to a similar increase in electrical conductivity as described for iron oxide above. It was also suggested by Jahanshahi (Jahanshahi 2004) that an increase in electrical conductivity was due to an electronic contribution in which a charge transfer process occurs between Mn^{2+} and Mn^{3+} within the slag. Other transition metal oxide slags such as chromium oxide (Cr_2O_3) are complicated to study, however it is assumed that similar electronic effects for such oxides contribute significantly to the electrical conductivity (Liutikov and Tsylev, 1963).

1.13. Modelling of Slag Properties

Metallurgical processing relies on the chemical reactions between liquid metal and top synthetic reducing slag, and the thermodynamics and kinetics of slag-metal reactions are very complex, which involve multiple simultaneous reactions of different constituents in liquid metal with slag. Because of complexity of reactions taking place in the furnace and difficulty in estimating the properties of slags, over the years, several models have been developed to predict slag properties. These modes are classified into five groups, i.e., numerical fits, neural network models, partial molar models and models based on structural parameters (Mills, Yuan et al. 2011).

1.13.1. Numerical fits

Numerical simulation for slags involves establishing an experimental data base over a wide range of compositions and temperatures for a property of interest. A numerical analysis is then carried out to obtain the best fit between different set of parameters, i.e., between the dependent variable and one or more explanatory variables (independent variables). For example, T_{liq} can be represented as $C_1(comp_1) + C_2(comp_2) + C_3(comp_3) + \ldots$ where C is a constant, composition (comp) can be in either mol% and numbers, 1,2,3, represent different components, e.g., SiO_2 (Mills, Yuan et al. 2011). This approach has been successfully applied in slag systems with a limited number of compositions, since a wide composition range of slags involve very complex and different phase equilibria (Sridhar, Mills et al. 2000, Mills 2011).

1.13.2. Artificial neural networks (ANN)

A neural network is a predictive modelling technique that processes information in a similar way to the biological nervous system. Input signals are processed through nodes (neurons) that are connected by links (synapses). A given neuron can process a signal and activate other neurons linked to it and the resulting pattern can be associated with a response. Just as an animal brain can learn how a specific range of inputs leads to a specific outcome, the artificial neural network can be taught which outcome to expect from a set if inputs. The ability of ANNs to recognise patterns from complicated data and detect trends has led to their application in science, engineering, finance and health (Sarma and Sarma 2000). In addition, neural network models have been used to calculate the viscosities of slags (Duchesne, Macchi et al. 2010). If trained properly by providing sample inputs and their associated output, an ANN can be an expert in the category of information it has been provided to analyse. It can then be used to predict the outcome of previously unseen, but related, input variables. ANNs are discussed in more details in Section 6.1.

1.13.3. Models based on structure

The majority of reported models are based on composition which in turn influence the transport and structural properties of slags (Zhang, Chou et al. 2009, Mills, Yuan et al. 2011, Zhang, Yan et al. 2011, Birol, Polat et al. 2015, Shu, Zhang et al. 2015)**.** These models tended to use basicity, e.g., ($CaO + MgO / SiO_2 + Al_2O_3$) ratios to represent and interpret the structure and transport properties. Basicity is defined as the ratio of basic oxides over acidic oxides**.** The other parameters used to represent structure models are the degree of polymerisation (NBO/T) or Q^n. Details of the depolymerisation model parameters are given in Section 2.4.

1.13.4. Atomistic modelling of slags

Computational atomistic modelling of materials, such as slags, is primarily concerned with determining the energy of a collection of atoms in a specific spatial configuration. Once the energy is known as a function of atomic coordinates, microscopic static/lattice properties can be investigated at a single configuration, or multiple configurations can be generated and coupled with the tools provided by statistical mechanics, to calculate macroscopic properties. Monte Carlo (MC) methods can be used to generate ensembles that follow Boltzmann statistics explicitly, or the laws of motion can be used in Molecular Dynamics (MD) to generate a time–dependent trajectory that follows Boltzmann statistics implicitly. Classical MD was used extensively in this thesis and is discussed in more detail in Section 3.

A critical feature of materials modelling is the branch of physics used to relate structure to energy and here two broad categories are commonly employed. The first category is simplified classical molecular mechanics (MM) methods that are empirical or semi-empirical in nature, since they deal with atoms as unified particles, either completely ignoring or approximately treating the electrons. These methods rely on the use of an empirically derived pair potential, which is a physics formula representing a collection of parameters that describe the interaction between different types of atoms in different chemical environments. Typically, the full interaction is broken up into two–body, three–body and many–body contributions, long–range and short–range terms, which have to be represented by suitable functional forms (see Section 3) (Salanne, Rotenberg et al. 2012). The main advantage of classical methods is that they are computationally efficient and fast and can be applied to large systems (thousands of atoms) or extended (>100 ns) trajectories) (Jahn and Madden 2007). A disadvantage of these methods is that they require parameterization by comparison to experiment or higher level of theories(Tangney and Scandolo 2002). Also, since the nature of the particles remain static during simulation, reacting systems cannot typically be described. Finally, the absence of an electronic structure means that excited states, which may be important in the high temperature regime of slags, cannot be modelled.

The second category uses the laws of quantum mechanics to calculate the energy and are often referred to as *ab initio* or first principles methods. These methods treat a material as a system of interacting nuclei and electrons, solving the Schrodinger's wave equation to obtain the energy and electronic structure. *Ab initio* methods use fundamental equations of quantum mechanics with a bare minimum of approximations. They do not rely on free parameters and no approximations are made regarding the nature of bonding or interatomic interaction. Methods can be either wavefunction–based, i.e., Hartree–Fock (HF) theory, or electron density–based, i.e., Density Functional Theory (DFT), with the latter dominating the field of *ab initio* simulations of slags (Salanne, Rotenberg et al. 2012). Quantum mechanical methods can describe bond breaking and forming and thus chemical reactions and have the ability to probe excited states. Additionally, these methods can be systematically improved by improving the treatment of electron correlation, which results from the instantaneous interaction between electrons. Mean–field approximations (such as HF theory) treat electronic interactions in an average way and in DFT, electron correlations enters as an approximation in the exchange–correlation functionals. A disadvantage of electronic structure calculations is that they are naturally computationally intensive and usually only feasible for relatively small systems or

short (< 1 ns) trajectories (Tangney and Scandolo 2002). Different classes of quantum MD (QMD) are briefly described in Section 3.

In the remainder of this section, a brief overview is given of typical applications of molecular dynamics in studying silicate slags. It should be noted that the complexity of classical MD simulations increases significantly as the number of components is increased. That is why most MD simulations of slags are limited to two or three components (e.g., see Benoit, Ispas et al. 2001). There are however, several studies which have been able to predict general trends that are consistent with experimental results (Huang and Cormack 1991, Delaye, Louis-Achille et al. 1997, Nevins and Spera 1998, Oviedo and Sanz 1998). The problem becomes acute on introduction of cations such as Na^+ or Ca^{2+} in silicate glasses (Benoit, Ispas et al. 2001). This is because it is difficult to find pair potentials that can accurately treat both the covalent and ionic nature of the interactions, which is important for describing the bond breaking and forming events that can occur in such chemically diverse environments.

Applications of molecular dynamics on silicate melts have been mainly focussed on predicting structural and dynamic properties of these systems in order to better understand their behaviour and improve metal, ceramic or glass production. Zhang, Sun et al. (Zhang, Sun et al. 2001) employed MD to study the effects of addition of Al_2O_3 on properties of the binary CaO-SiO_2 and ternary CaO-Al_2O_3-SiO_2 melts. It was found that the addition of alumina gradually replaces CaO in a polymer chain, resulting an increased amount of triclusters (three-coordinated oxygen). This information from MD simulations provided an insight and an improved understanding of the relationship between structure and properties of the silicate melts. In another study, Belashchenko, Ostrovski et al. (Belashchenko, Ostrovski et al. 2001) used MD simulation to study binary CaO-FeO, MgO-SiO_2, FeO-SiO_2, CaO-SiO_2 and ternary CaO-FeO-SiO_2 systems. They concluded that the thermodynamic properties depend strongly on the ionic potentials used to model the systems. Zhang, Zhang et al. (Zhang, Zhang et al. 2014) investigated the effect of basicity (CaO/SiO_2) on structural and transport properties of CaO-SiO_2-Al_2O_3-FeO slags. It was concluded that an increase in basicity lead to the depolymerisation of the slags. The diffusion coefficients were found to increase with an increasing basicity, while the viscosity values decreased with an increasing basicity. Zheng, Yang et al (Zheng, Yang et al. 2014) investigated the variation of self–diffusion coefficients in calcium aluminosilicate slags. The diffusion coefficients were found to be affected by the degree of polymerisation i.e., more depolymerised slags had higher diffusion rates. The order of diffusivity for atoms was found to be as follows: Ca > Al > O > Si. It was also concluded

that the diffusion coefficients of Al, Si and O share close values indicating that O atoms move cooperatively with network–forming atoms in SiO_4 and AlO_4 tetrahedra (Zheng, Yang et al. 2014). Yao, He et al. (Yao, He et al. 2017) investigated the structural properties of $CaO–SiO_2–TiO_2$ (CST) systems using classical molecular simulations. The addition of TiO_2 was found to increase the concentrations of 4–coordinated Si and 4–coordinated Ti. An increasing amount of CaO was found to decrease the proportion of bridging oxygen (BO) atoms and network connectivity Q^n. He et al. (Wu, He et al. 2015) studied the microstructure and transport properties of $CaO–SiO_2$ and $CaO–Al_2O_3$ binary systems also using molecular dynamics simulations. An increasing amount of CaO was found to increase the degree of depolymerisation of melt resulting in a decrease in viscosity and an increase in electrical conductivity of the melt.

Applications of first–principles approaches are widespread in materials science and are employed in areas where classical molecular dynamics simulations are insufficient. *Ab initio* MD studies of silica glass and its melt have demonstrated the ability of this approach to describe the local structure and dynamics of such systems with reasonable accuracy (Sarnthein, Pasquarello et al. 1995, Benoit, Ispas et al. 2001). The additional advantage of using *ab initio* MD to study slag systems is that it also allows access to the electronic properties of the system (Oviedo and Sanz 1998, Benoit, Ispas et al. 2000). Vuilleumier, Sator et al. (Vuilleumier, Sator et al. 2009) investigated structure and transport properties of silicate melts using both classical and *ab initio* MD. From these investigations, it was concluded that the structural parameters of the simulated melt vary little between the two approaches (*ab initio* versus empirical) and are in satisfactory agreement with the structural data available in the literature.

2. SLAG STRUCTURE AND PROPERTIES

2.1. Industrial slags

Slag is a useful by-product of the smelting process. It is made from the meltdown liquid of sinter, gangue material, lump, coke and flux. Slags typically can contain a mixture of refractory oxides (SiO_2, Al_2O_3, FeO, MgO and CaO), which are either present in the original ore, or a byproduct of reductive roasting (Shiau and Liu 2008, Shiau, Liu et al. 2012). Slag is less dense than the metal liquid and floats on top; this allows the ease for tapping the slags and the liquid metal from the furnace. The slags are tapped from the top and liquid metal is tapped from the bottom of the furnace.

2.2. Crystalline, glassy and molten slags

Slags can be classified as either glassy, crystalline, melt or a mixture of the two phases. Some of the factors determining the nature of the phases formed by the slag includes the degree of polymerisation and thermal history. As rough rule of thumb, glassy slags occur when Q > 2.5 and crystalline slags when Q = < 2 with Q being the degree of polymerisation (Mills, Yuan et al. 2011). Figure 5 shows the change in volume, V, of a silicate melt during cooling through the transition region, T_g. Rheologically, T_g is defined as the temperature at which viscosity is equal to 10^{12} Pa s for a cooling rate of the order 10 K/min.

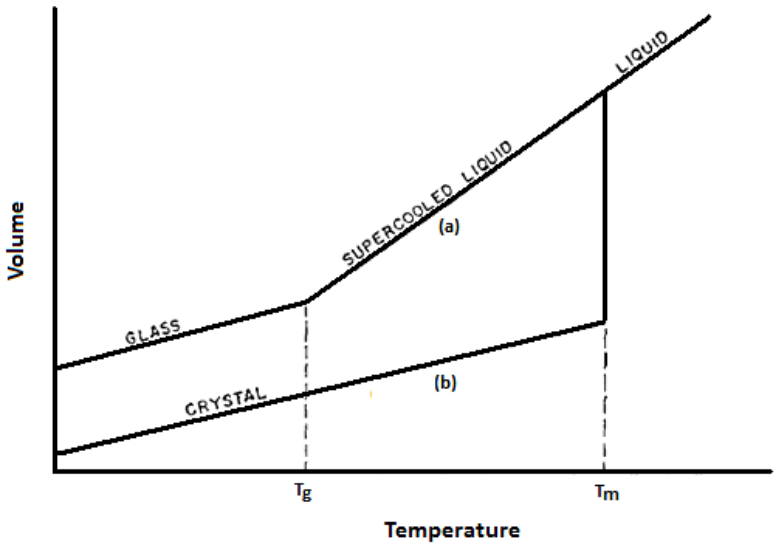

Figure 5. Schematic representation of (a) the glass transition and (b) crystallisation from liquid (Zanotto 1992).

The slow cooling of the melt (path b in Figure 5) may result in crystallisation at the melting point, T_m, leading to the formation of crystalline slag. The crystalline phase is made up of ions which are in fixed positions and are arranged in a regular manner; thus, in crystals, the disorder and entropy tend to be low. Fast cooling rate may prohibits crystal nucleation and growth resulting in a metastable supercooled liquid (scl) (path a in Figure 5)(Mills 2016). As the temperature drops, the time required to reach the equilibrium configuration of the liquid increases, and eventually the structural change is not fast enough to keep pace with the cooling rate. At this point, a transition temperature, T_g, is reached below which the atoms are frozen into fixed positions (only thermal vibrations remain) and a glassy or amorphous slag is formed. Therefore the glassy slag formation route from the liquid state is possible if path (a) is followed. The glassy slags and its melt phase lack regularity in arrangement of structural arrangement resulting a much higher level of disorder. When the glassy slag is heated to a temperature range falling between T_g and T_m, it tend to crystallise in order to achieve thermodynamic equilibrium. At T_g, a rapid thermodynamic property changes takes place, this include an abrupt change in the heat capacity (C_p) and thermal expansion (α) (Mills, Yuan et al. 2011). Similar to silicate glass, the silicate melt consist of 3-dimensional (3-D) interconnected networks of SO_4^{4-} tetrahedra in which silicon cations are joined by bonding with the oxygen atoms.

2.3. Silicate melt structure

The study of silicates is of importance and plays a role in such diverse fields as geosciences, material sciences and metallurgy. Greaves and Sen (Greaves and Sen, 2007) defined the glass as an amorphous solid that, unlike a crystal, lacks periodicity in its atomic structure. Understanding glass structure has been the subject of much research over many years. The reason is that the precise description of glass structure has been a challenge (Henderson 2005, Wright 2014). Owing to the amorphous nature of glass, determination of atomic-level structural details has been challenging to elucidate. The understanding of glass structure has been used to interpret and help understand the properties of other silicate melts such as slags (McMillan 1984).

Glasses have been widely used to study the silicate melts and related oxides such as slags and ceramics (Henderson 2005). In comparison with crystalline silicates, silicate glasses are amorphous and thus possess no long-range structural periodicity or symmetry. However, a refined structural ordering can be drawn from the inspection of local molecular structure where different scales of order have been defined as short-range (1.5-2.9 Å), medium-range (2.9-5.5Å), and more extended scale (5.5 Å and above) (Wright 1994, Wright 2014). The distance

beyond the long-range ordering in the radial distribution function becomes indistinguishable from the $4\pi r^2\rho_0$ function where r is interatomic separation and ρ_0 is the mean atom density. Slag is an essential by-product of the smelting process and most slags are silicates. The short range order of silicate melts is dominated by the structure of the SiO_4 rigid unit. Silicates are considered ionic materials in which a single anion, i.e. oxygen, is bonded to a variety of cations of different sizes and electrical charges (Mysen, Virgo et al. 1982, Mysen and Richet 2005). These systems are mainly defined by how cations fit in between oxygens due to the relatively large effective radius of the oxygen atom.

Crystallography of solid silica shows that silicon is coordinated by four oxygen atoms which occupies the corners of a tetrahedron. The oxygen atom at each corner is connected to two silicon atoms resulting in a polymer chain which extends in three dimensions. The corner sharing is such that the resulting stoichiometric formula of SiO_2 has a neutral charge. A Si ion has an electronic charge of 4+. Since each oxygen atom of the tetrahedron has an extra charge, this results in (SiO_4^{4-}) species (Shackelford and Doremus 2008). The tetrahedra are connected to one other by sharing common oxygen called bridging oxygen (BO). This leads to a stable structural element of SiO_4^{4-} structure which can polymerise and form networks, complex silicates or chains. Terminal oxygen connected to a cation that is not tetrahedrally coordinated is called non-bridging oxygen (NBO).

2.4. Structural models

There are several theories that have been used to describe the structure of amorphous SiO_2 and perhaps the continuous random network model (CRN), originally proposed by Zachariasen (Zachariasen 1932), is the most widely accepted model. The CRN model has to meet the following conditions:

- Oxygen atoms may not be linked to more than two cations, i.e., bridging oxygen (BO) atoms are shared between two adjacent silicon atoms
- At least three corners of each oxygen polyhedron must be shared for a three dimensional network
- The Si^{4+} cation coordination number must be four or less

Zachariasen classified the ions into three categories: network-formers (Al^{3+}, Si^{4+}, Ti^{4+}, Fe^{3+}), the network breaking alkali and alkaline earth metal cations (K^+, Na^+, Ca^{2+}, Mg^{2+} and Fe^{2+}) and intermediate oxides (Cr^{3+} and Er^{3+}). The continuous random network model predicted glass formation well and accurately predicted the main glass forming oxides such as SiO_2, GeO_2,

B_2O_3 and P_2O_3. The depiction of Zachariasen's two-dimensional schematic diagram of SiO_2 vitreous network showing a continuous random network is shown in Figure 6.

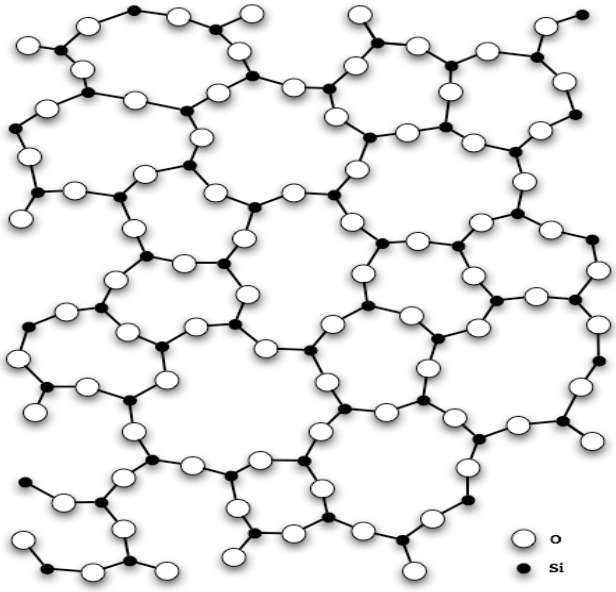

Figure 6. Depiction of Zachariasen's two-dimensional schematic diagram of an SiO_2 vitreous network showing a continuous random network where silicon atoms (closed circles) are connected by bridging oxygen atoms (open circles) adapted from (Zachariasen 1932) .

The Zachariasen model assumes that alkali ions enters holes in the 3-dimensional framework structure and form an ordered distribution within the glass. The CRN is not able to interpret and account for all the experimentally observed glass properties as it assumes that the introduction of network breakers does not alter structure and properties of the glass. Warren and Biscob's (Warren and Biscob 1938) X-Ray diffraction results on silicate glasses indicated that the introduction of alkali ions create singly bonded oxygens. It was also suggested that the alkali ions and NBO would be paired to maintain charge neutrality and would be randomly distributed.

Technologically significant glasses and silicate melts contain additional oxides such as alkali and alkali earth oxides that are introduced intentionally to effect changes in physical and structural properties of the melt. These were not well accounted for by the CRN, hence the modified random network (MRN) model was proposed by (Greaves 1985). In this model, it was proposed that the distribution of network-modifiers is not inhomogeneous as proposed by (Warren and Biscob 1938). Instead the alkali ions are homogeneously distributed and spatially

aggregated along with NBO resulting in alkali and NBO rich regions and silica rich regions (or alkali-poor) as shown in Figure 7. Therefore in a (MRN) model, the network-modifier regions would extend to percolation channels, when their volume fraction exceeds 16%, thus making the modifier cation diffusion easier in the glass structure (Calas, Cormier et al. 2002).

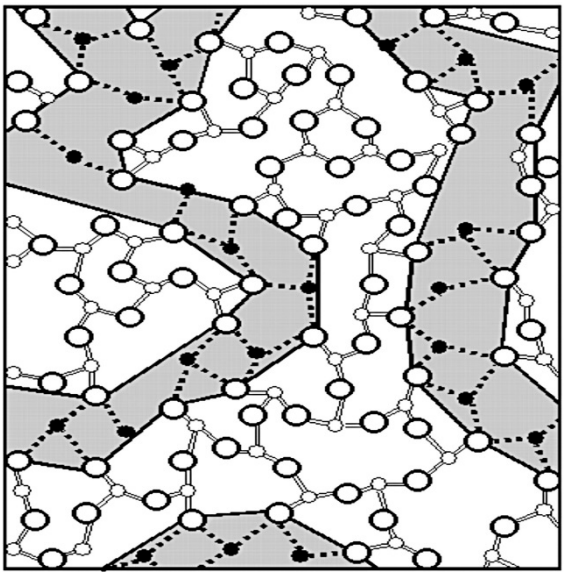

Figure 7. The modified random network, where modifier channels occur due to the addition of alkali or alkaline earth metals (closed circles) to the Si (small open circles) and O (large open circles) network (Wright 2014).

The bond breaking caused by network modifiers leads to the depolymerisation of the melt, thus increasing ion mobility and consequently impacts on the transport properties. Network modifiers increase the melt electrical conductivity (Segers, Fontana et al. 2013) while lowering viscosities and subsequently also the processing temperatures of the silicate melts (Mills 1993, Cormier and Neuville 2004). According to Mills (Mills, Yuan et al. 2011), temperature and composition affect the structural and transport properties of silicate melts.

One measure of silicate melt composition that can be related to properties is the basicity, which is the ratio of network breakers to network formers, viz. (MgO + CaO) / (SiO_2 + Al_2O_3). A higher ratio often indicates higher electrical conductivities and lower viscosities. A small change in temperature and composition may have a drastic effect on production and on quality of the metal produced. Hence, proper control and understanding of the effects of these parameters plays an important role in the production of silicate melts and the smelting process.

2.5. Aluminosilicates

Aluminium oxide (Al_2O_3) and silicon dioxide (SiO_2) are the two most important structural forming oxides in silicate melts (Mysen, Virgo et al. 1985). Therefore, in order to describe glasses and slags, it is important to understand the structural properties and influence of these oxides on structure and properties of aluminosilicate melts. The melts comprising these oxides have a wide range of industrial applications including ceramics, petrology and the glass industry. The Al^{3+} cation is generally considered to be a network former together with Si^{4+} cations. When Al_2O_3 is added to the SiO_2 system, some of the Al^{3+} cations assume a tetrahedral coordination and replace some of the Si^{4+} ions in the liquid network.

Basic oxides like CaO and MgO which are network breakers cause a progressive loosening of the polymeric chains of the melt and increase the amount of free ions and electrical conductivity. The network-former such as SiO_2 increase the degree of polymerisation of the melt by forming large and complex anions $[SiO_4]^{4-}$ which impede the movement of cations and lowers the electrical conductivity of the slag. As mentioned earlier, the amphoterics play a dual role when present in the slags i.e., they can either be network formers or breakers. When amphoteric oxide such as Al_2O_3 acts as a network former, it forms $[AlO_4^{5-}]$ tetrahedron and replace the $[SiO_4]^{4-}$ tetrahedron in the silicate polymer chain. Increasing the amount of Al_2O_3 in the silicate melt leads to an increase in the degree of polymerisation which in turn lowers the electrical conductivity of slag melt. In peralkaline region, where the proportion of alkali metals and/or alkaline earths exceeds that necessary for charge-balance of Al^{+3}, the Al^{+3} cation may exist in several coordination environments other than four and act as a network breaker leading to increased electrical conductivity of the melt.

Substituting Al_2O_3 for SiO_2 in a silicate melt results in a decrease in the number of NBOs while enhancing the degree of polymerisation, subject toif there being a sufficient number of network breakers in the melt (Stebbins and Xu 1997, Zhang and Chou 2013). The higher degree of polymerisation leads to a decrease in electrical conductivity of slag (Mills 2016, Mills 2011). The Al^{3+} cations ions are tetrahedrally coordinated by oxygens in the melt and enter the Si–O tetrahedron network as $[AlO_4]^{5-}$ (Rlebling 1964). Since the valence charge of aluminium ions in $[AlO_4]^{5-}$ units is +3, which is less than that of the silicon ion (4+), it requires charge-balancing. This apparent charge deficiency in a trivalent Al^{3+} cation is compensated by an alkali metal cation that sits near on aluminate tetrahedron or is shared between the two aluminate tetrahedra. The alkali or alkali earth metal cations therefore stabilize the tetrahedron by sharing

bridging oxygen atoms between the aluminate tetrahedra. The charge balancing cations therefore do not participate in network modification (Mysen and Virgo 1994, Mysen and Richet 2005) and the formation of NBOs. One mole of Al_2O_3 can form two moles of aluminium ions; substitution of one mole of SiO_2 by one mole of Al_2O_3 greatly decrease the number of free ions. This results in an increase in the number of tetrahedra, thus promoting re-polymerisation of the silicate melt. Figure 8 illustrates the SiO_2 substituted by Al_2O_3 and the charge balancing of an aluminate tetrahedron by an alkaline (Ca^{2+}) cation.

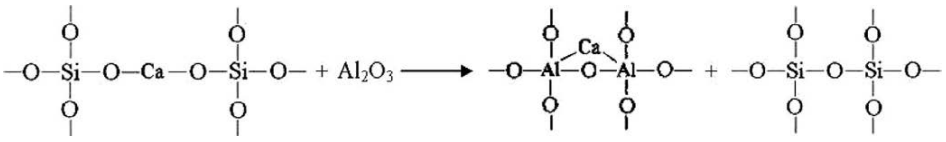

Figure 8. Depiction of SiO_4 displacement by Al_2O_3 and charge balancing of $[AlO_4]^{5-}$ tetrahedron by Ca^{2+}.

From the stoichiometry, one mole of Al_2O_3 needs one mole of CaO or MgO to achieve charge neutrality. The mole ratio of network modifiers over network formers, which is analogous to basicity, can be described as $R = (CaO + MgO) / (Al_2O_3 + SiO_2)$. If R is equal to 1, all Al^{3+} ions are charge balanced, resulting in an Al^{3+} becoming a network former. This implies that the melt composition is fully polymerised. An increase in Al_2O_3 concentration in silicate melts can lead to a larger fraction of alkali cations being closely attached to Al^{3+} cation. In a mixed alkali melt, the tendency of modifier cations to charge balance $[AlO_4]^{5-}$ tetrahedra units decreases with increasing ionic field strength, as $K^+ > Na^+ > Ca^{2+} > Mg^{2+}$ (Mysen 1987).

In the peraluminous composition range, i.e. for melts without a sufficient number of charge balancing cations, to maintain local charge neutrality, it has been proposed that either three bonded oxygen atoms (TBO) (Lacy 1963, Tossell and Horbach 2005) and/or high coordinated Al^{3+} cations having five or six oxygen ion neighbours are formed (Riebling 1966, Neuville, Cormier et al. 2008). TBOs occur when oxygen atoms bond to three network formers in order to achieve local charge neutrality. There are three possible types of TBOs in aluminosilicates, depending on which network formers the oxygen atoms are connected to: (1) one silicon and two aluminium atoms; (2) two silicon and one aluminium atoms; and (3) three aluminium atoms. Sites containing oxygen with three, highly charged, tetrahedral cations as first neighbors have been observed in Al-rich aluminosilicates and are called “triclusters” (Winkler, Horbach et al. 2003). Highly coordinated Al^{3+} cations can also occur through densification of silicate

melts under high pressure. These highly coordinated species affect transport properties such as viscosity and diffusion coefficients (Toplis and Dingwell 2004, Pfleiderer, Horbach et al. 2006). This further highlights the importance of Al^{3+} cations in terms of their influence on silicate melt properties.

2.6. Q^n ratios

The number of bridging oxygens atoms associated with each tetrahedrally coordinated Si^{4+} (or Al^{3+}) cation is an important descriptor of the polymerisation of the slag structure. Q^n is defined as the number (n) of BOs associated with a four coordinate Si atom. In addition, since Al is able to also play the role of structure former, a Q^n(Al) distribution for Al atoms can be similarly calculated. It should however, be kept in mind that Al atoms can produce $[AlO_5]^{7-}$ species in addition to the Si-like $[AlO_4]^{5-}$.

The degree of polymerisation of aluminosilicate melts may be represented by the NBO/T ratio and calculated as follows (Mills 1993),

$$Q = 4 - \frac{NBO}{T} = 4 - \frac{2O - 4T}{T} \tag{9}$$

This equation is based on the assumption that in the peralkaline region charge balance is provided by alkali–earth cations until all $[AlO_4]^{5-}$ tetrahedral are saturated, with the remainder then entering into the network as structure breakers. *NBO* refers to the number of non-bridging oxygens, *O* is the total number of oxygen atoms and *T* is the number of tetrahedrally coordinated network formers. A melt is fully polymerised when NBO/T = 0, and increasing NBO/T values indicate that the melt becomes more depolymerised. A decrease in NBO/T therefore mean an increase in polymerisation. Only Q^4 species are present in pure silica, while Q^2 and Q^3 species are found in modified glasses. The *Q* values imply the following Q^4 (NBO/Si = 0), Q^3 (NBO/Si = 1), Q^2 (NBO/ Si = 2), Q^1 (NBO/Si = 3), and Q^0 (NBO/Si = 4). The degree of polymerisation affects physical properties of silicate melts, with less polymerised melts generally having enhanced transport properties. However it should be mentioned that silicate melt properties depend on other factors including composition, temperature and pressure. Different network formers prefer to be localised in different Q^n environments in different silicate melt compositions (Tilocca, Cormack et al. 2007).

2.7. Coordination numbers

In order to better understand the structural and transport properties of materials, it is important to investigate the local environment of an atom in a disordered structure, especially at high temperatures. Coordination number, which is the number of atoms surrounding the central atom, may be determined by integrating the area under the first peak of the radial distribution function (RDF). The RDF is discussed further in section 4.2.

The silicon and aluminium cations, which are network formers, are usually 4–coordinated. However at higher pressures 5– and 6–coordinated Si and Al cations are formed (McMillan and Wilding 2009), while 5–coordinated network formers could serve as transition structures in microscopic diffusion in silicate melts (Neuville, Cormier et al. 2006). The highly coordinated network formers control the transport properties of the melt. Aluminum coordination also increases with a decreasing number of alkali and alkaline earth metal cations (i.e., when there is an insufficient number of charge compensation cations) in the melt, in order to achieve charge neutrality (Neuville, Cormier et al. 2006).

The coordination environment of magnesium (Mg) cations in silicate melts usually ranges from 4–8. In a mixed cation environment, the coordination of Mg cations depends on the ionic field strength of the competing cation (Shimoda, Nemoto et al. 2008, Shimoda, Tobu et al. 2008). Magnesium cations bind more strongly to oxygen anions than competing lower field strength ions (K^+ and Na^+), except in a melt with mixed alkali cations, where there is no binding strength difference between Ca^{2+} and Mg^{2+}. In the CaO-MgO-Al_2O_3-SiO_2 (CMAS) system, the Mg^{2+} cation are expected to diffuse faster than the Ca^{2+} cation because of its smaller cationic radius. The coordination environment of calcium cations in silicate melts (Ca^{2+}) ranges from 6 to 10 (Taniguchi, Okuno et al. 1997, Vuilleumier, Sator et al. 2009).

The implication of the high coordination environment of cations is lower diffusion coefficients and electrical conductivities owing to cationic movement being hindered by the surrounding environment (Mills 2016). The cation CN increases with increasing cation size. As mentioned earlier, the electrical conductivity of slag melt takes place through the movement of cation, the larger cations tend to move more sluggishly through melts than small cations (leading to lower diffusion coefficients and electrical conductivities). The small cations with lower CN are more mobile than larger cations and can slip through the holes in the network leading to higher electrical conductivities (Mills 2011, Zhang, 2010, Zhang, Yan et al. 2011). In general, the

effect of CN on electrical conductivity of the slags is smaller than the degree of polymerisation (Mills 2016). Factors contributing more to the electrical conductivities of slags are mainly the degree of polymerisation and cation ionic field strength ($K^+ < Na^+ < Li^+ < Ca^{2+} < Mg^{2+}$) which leads to a wider distribution of polymeric species Q^n and thus increase electrical conductivity (Mills 1993, Mills 2016).

2.8. Transport properties

As mentioned above, the silicate melt structure is of great importance in understanding metallurgical processes (Lee, Park et al. 2003). Structural arrangement in silicate melts is the dominant factor which determines transport properties such as viscosity, electrical and thermal conductivity. Transport coefficients, such as self-diffusion coefficients, shear viscosities and thermal conductivities may be defined in terms of the response of a system to a perturbation (Spera, Nevins et al. 2009).

2.8.1. Self-diffusion coefficients

The diffusion coefficient refers to a transport property that describes the movement of a specific species. The diffusion coefficient, *D*, in a continuous system can be defined Fick's second law, also called the diffusion equation (Atkins, Physical Chemistry) to give:

$$\frac{\partial C(r,t)}{\partial t} = D\frac{\partial^2 C(r,t)}{\partial t^2} \tag{10}$$

where *C(r,t)* is the space and time–dependent concentration of the atoms in questions.

In general, diffusion can be classified into three categories viz., self–diffusion, tracer diffusion and chemical diffusion (Hofmann 1980, Zhang 2010). In self–diffusion, no chemical potential is involved, the diffusion is observed by labelling the species with a stable isotope tracer. In tracer diffusion, a labelled tracer is introduced in the form of an isotope of a chemical element that is not present in the in the substance. However, the tracer concentration is so small that no appreciable concentration gradients are introduced in the system. Chemical diffusion on the other hand, occurs in the presence of a bulk chemical potential (Hofmann , Zhang, Ni et al. 2010). A summary of various kinds of diffusion can be found in (Zhang 2010, Zhang, Ni et al. 2010). The focus of this study is on the measurement of self–diffusion. Experimentally, measurements of self–diffusivity cannot be made without introducing an isotropic gradient, but

in molecular dynamics simulations, diffusion coefficients are readily available as the motion of individual particles can simply be traced. Hence there is no need to introduce an isotropic gradient.

Diffusion coefficients of the different atomic species in slags can depend on a number of factors, e.g. the physical conditions (temperature and pressure), the concentrations of the various components and finally also the nature of these components. Diffusivity for a given species in a melt increases rapidly with temperature (T), following an Arrhenius relationship,

$$D = D_0 \exp\left(-\frac{\Delta H_a}{RT}\right) = D_0 \exp\left(-\frac{E_a + P\Delta V_a}{RT}\right) \quad (11)$$

where D_0 is the pre-exponential factor, R is the gas constant, and ΔH_a, E_a, and ΔV_a are the activation enthalpy, the activation energy, and the activation volume, respectively.

At high pressure diffusion is expected to be lower, since the free volume between ions is reduced, which makes diffusion more difficult (Ni et al. 2015). The composition is also important. At higher concentrations of network formers, diffusion is expected to be lower, since network formers results in a more polymerised melt structure, which inhibits diffusion and higher pressure diminished free space (Ni et al. 2010, Pommier et al, 2008). On the other hand, addition of network modifiers results in an increase in the rate of diffusion within the melt. It is not only the nature of cations as modifiers or network formers that is important, but also the relative amounts of each. For example, Jambon and Carron found that the diffusion of Na is dependent on the ratio of both modifiers and that the diffusivity of Na decreases monotonically as the Na/K ratio drops. Impurities, such as water, can also affect diffusion. Water promotes depolymerisation in silicate melts and also increases ionic porosity, which reduces the hindrance of diffusing species (Ni et al. 2010).

The diffusion rates of atomic species are also governed by the valence charge (z) and size (radius r) (Zhang, Ni et al. 2010). In alkali and alkaline earth metal ions, for a given ionic charge, the diffusion rate is ion size dependent; it decreases with an increasing ionic size. Intuitively interpreted, this means that the diffusion is impeded by the relatively large size of a diffusing particle.

Self-diffusion coefficients of silicate melts have been studied using MD simulations. With MD simulations it is possible to calculate the diffusion coefficient by following the motion of the individual atoms or calculating the velocity autocorrelation function. Simulations are able to

provide results at physical conditions that are difficult or expensive to achieve experimentally, such as very high pressure or temperature. In MD simulations, at the limit of large times, *t*, the diffusion coefficient can be related to for the mean square displacement (MSD),

$$\frac{d}{dt}\sum_{i}^{N}\left[\vec{r}(t)-\vec{r}(0)\right]^2 \tag{12}$$

The average self–diffusion coefficient, D_i, of an ion of type *i*, is calculated from the average mean square displacement using the Einstein relation (Allen and Tildesley 1989). After an initial period of ballistic motion, at small values of *t*, the MSD increases linearly with time. In this linear regime, the slope of the curve yields the self–diffusion coefficient. Although there are several reports in the literature of MD simulations performed to determine the diffusion mechanism in silicate melts, discrepancies in diffusion coefficients are introduced by the use of different force fields. MD simulations are not only used to calculate diffusion coefficients but with insight provide with carefully parameterised potential functions or ideally quantum mechanical MD, can also be used to understand the mechanism of diffusion at an atomistic scale. For example, it is known that pure amorphous silica forms a network of corner–shared SiO_4 tetrahedra and MD simulations have shown that the diffusive motions are dominated by the existence of defects such as SiO_3 and SiO_5 units in the network (Winkler, Horbach et al. 2003).

Further examples and references of factors effecting diffusion, the values of diffusion coefficients and trends among ions, can be found in the reviews of Ni et al. (Ni et al. 2015) and Zhang et al. (Zhang et al. 2010)

2.8.2. Thermal conductivity

Thermal conductivity, λ (measured in W m^{-1} K^{-1}) is the ability of a material to conduct heat (energy). Thermal conductivity of slags and silicates is a transport property that is difficult to measure experimentally, owing to difficulties associated with high temperature measurements (Monaghan and Brooks 2013). Hence, there are relatively large variations in experimental results reported in the literature for this property. Heat transfer in liquid oxides is complex, as it involves both atomic vibrations (phonons) and radiative attenuation of photons (Monaghan and Brooks 2013). It is difficult to separate the atomic vibrations (phonons) components from the radiative attenuation of photons in measurement. The thermal conductivity (λ) of slags

involves phonon conduction, consequently, is very dependent on structure (Mills 1984, Zhang 2006).

Other properties affecting thermal conductivities of slags include temperature and chemical composition of the slag (Kang and Morita 2006). Most smelting processes involve heat transfer in which thermal properties and fluxes play a crucial role in improving the quality of the product and the process itself, i.e., the surface quality of the final product may be governed by heat transfer through mould flux (Kang and Morita 2006, Mills, Yuan et al. 2011).

The thermal conductivity of molten slags normally increases with increasing SiO_2 content, which is the opposite trend to that seen with electrical conductivity (Zhang, Chou et al. 2009). Since SiO_2 promotes polymerisation of the melt, it can be inferred that conduction occurs easily along the chains. In this case, heat transfer results from lattice conduction which occurs by lattice vibrations of specific modes. Therefore, thermal conduction in silicates is influenced by the structural arrangement within the melt. Acidic oxides (SiO_2 and Al_2O_3) form covalently bonded networks, while the basic oxides (CaO and MgO) disrupt the network by forming ionic bonds with anions. Thermal conductivity occurs more readily in covalent bonded networks than in ionic bonded networks (Kang and Morita 2006).

There are limited examples of the use of molecular dynamics simulation to calculate thermal conductivity of silicate melts. Salanne et al. (Salanne, Marrocchelli et al. 2011)have used classical MD to calculate the thermal conductivity of Mg_2SiO4 (forsterite) at temperatures where quantum effects are negligible (2800 K) and obtained values much larger than that for typical mafic melts at similar (ca. 2000 K) temperatures (Ni et al. 2015). Tikunof and Spera (Tikunoff and Spera 2014) on the other hand, used non–equilibrium classical MD to calculate thermal conductivity of Mg2SiO4, CaMgSi2O6 and NaAlSi3O8 liquids at high temperature, with values comparing well to estimates extrapolated from ambient conditions.

2.8.3. Electrical conductivity

Electrical conductivity (σ) of a silicate melt occurs via the movement of charge carriers when an electrical potential is applied. It is a measure of the rate of electrical charge transfer. ‘Loose’ particles, such as alkali or alkaline earth metal ions or impurities, have relatively high self-diffusion rates or relatively high polarisabilities compared to other species in the structure, resulting in higher contributions to electrical conductivity (Bagdassarov, Maumus et al. 2004) .

Electrical conductivity of silicate melts containing network breakers is usually ionic in nature. The conductivity via electronic means is, however, significant under specific conditions such as with low temperatures and iron-rich compositions or with other transition metal oxides (Barczynski and Murawski 2002, Mills, Yuan et al. 2011). The Arrhenius expression can be used to relate the dependency of electrical conductivity on temperature and pressure.

$$\sigma = \sigma_0 \exp\left(-\frac{H_a}{RT}\right) = \sigma_0 \exp\left(-\frac{E_a + P\Delta V_a}{RT}\right) \quad (13)$$

where σ_0 is a pre-exponential factor, R is the gas constant, and H_a, E_a, and ΔV_a are the activation enthalpy, the activation energy and the activation volume, respectively. From the above equation, it is evident that electrical conductivity is also a function of temperature i.e., it increases with an increasing temperature for a given composition. Two different temperature dependent electrical conductivity regimes have been observed in silicate melts. Below the glass transition temperature (T_g), silicate melts show Arrhenius type behaviour over a wide temperature range, while above T_g they show non-Arrhenius behaviour. In contrast to relaxation theory which predicts non-Arrhenius behaviour above the glass transition temperature, rhyolite exhibits Arrhenius behaviour (Dingwell and Webb 1990).

Several experimental studies on the electrical conductivities of silicate melts have demonstrated that this property is pressure dependent (Gaillard 2004, Ni, Keppler et al. 2011, Laumonier, Gaillard et al. 2015). However, in some studies carried out on multiphase systems and at high pressure (0.3 to 2 GPa), no influence on electrical conductivities was observed (Maumus, Bagdassarov et al. 2005). Hydrous silicate melts show enhanced conductivity, as shown by Gaillard (Gaillard 2004), who observed an increase in electrical conductivity and a decrease in activation energy with increasing water content. The influence of H_2O on transport properties within the slag is likely to arise from enhanced liquid dynamics and the mobility of ions exerted by this species.

Measuring electrical conductivity at high temperature is challenging as is the measurement of other properties at higher temperatures. Factors affecting the electrical conductivity include concentration of species, cation charges and sizes and the polymeric nature of the silicate melt. Small cation sizes and high cation concentrations lead to a higher number of cations slipping through the holes, voids and defects in the network. The more polymerised the structure of a silicate network, the lower the electrical conductivity because the movement of cations is

hindered (Sarkar 1989, Guillot and Sator 2007). Electrical conductivities are composition dependent as shown in studies of these systems by Van Der Colf (Van Der Colf 1979) .

Several studies have been published that investigate electrical conductivities of silicate melts over a wide range of compositions, conditions and environments. For example, Stein and Spera (Stein and Spera 1996) used Car–Parrinello molecular dynamics **(**CPMD) to predict electrical conductivity of Na in $NaAlSiO_4$ melts at temperature and pressure ranges of 2500–4000 K and 4 ± 1.5 GPa, respectively. Conventionally, Na is considered a dominant charge carrier in Na-bearing melts (Belashchenko, Ostrovski et al. 1998, Gaillard 2004). The resulting activation energy values for electrical conductivity was consistent with those experimentally measured for the same system but at much lower temperatures. MD results from Guillot and Sator 2007 (Guillot and Sator 2007) on Na-bearing melts have shown that the contribution of Na to electrical conductivities is composition dependent, decreasing from rhyolitic to andesitic to basaltic to ultramafic melts. Belashchenko and Ostrovski (Belashchenko, Ostrovski et al. 1998) estimated electrical conductivities of cryolite alumina (CaF_2^- and Al_2O_4) systems using MD. Their estimated conductivity values were also in good agreement with experimental values. MD has been successfully used to model electrical conductivity in ionic liquids (Rey-Castro and Vega 2006).

2.8.4. Viscosities

Viscosity (η) is the measure of the resistance of a fluid to flow when subjected to shear stress and is an important property that governs the rate of transport of matter and thus the energy in a metallurgical furnace (Santhy, Sowmya et al. 2005, Park 2012). It is therefore a very important parameter when studying the smelting process and its optimisation. Like other transport properties, viscosity is a function of composition, temperature and pressure (Prikhodko, Togobitskaya et al. 2010, Muller and Erwee 2011). The viscosity decreases with an increasing temperature for a given composition.

A major factor for the temperature dependence of viscosity is that an increase in temperature tends to break down the structure. An Arrhenius type equation is widely used to approximate the temperature dependence of viscosity;

$$\eta = \eta_0 \exp\left(\frac{E_a}{RT}\right) \tag{14}$$

where η_0 is the pre-exponential factor and E_a is the activation energy. Since viscosity is the resistance to flow of the material, the presence of large complexes of silicon, aluminium and oxygen ions increases the viscosity of the melt. The flow and mixing within furnace systems is strongly influenced by viscosity, and therefore these two phenomena need lower viscosity to yield better mixing and a thinner boundary layer in the furnace (Kondratiev, Jak et al. 2002). A lower viscosity also facilitates the movement of impurities from the metal melt to the slag (Agarwal 2012). Enhanced mobility of ionic species at lower viscosities is expected because of higher depolymerisation. Since the viscosity is controlled by the composition, it is therefore desirable to maintain an appropriate concentration of basic oxides and acidic oxides in slag systems in order to facilitate proper refining processes. The viscosity of the SiO_2-CaO-MgO-Al_2O_3 - FeO system has been found to decrease with increasing FeO content indicating that the FeO acts as a silicate bond breaker (Muller and Erwee 2011). Furthermore, viscosities of slag systems decrease with increasing basic content of the oxides (Kim, Kim et al. 2010).

2.8.5. Relationships between thermophysical transport properties

Viscosity and self-diffusivity of silicate melts can be related via the Eyring and Stokes-Einstein relations. These two relations are derived in completely different ways but relate to diffusion and viscosity in the same functional form. The relationship between viscosity and the self-diffusion coefficient, D, is given by the Eyring and Stokes-Einstein equations as follows:

$$\eta D = \frac{k_B T}{\lambda} \tag{15}$$

where D is the diffusion coefficient, T the temperature, k_B the Boltzmann constant, λ the ionic translation distance and η the shear viscosity. Studies relating viscosities and diffusion coefficients have been reported by several authors (Reid, Suzuki et al. 2003, Lacks, Rear et al. 2007).

The Nernst-Einstein equation is used to calculate and relate electrical conductivity to ionic self-diffusivity of an ion via (Einstein 1905, Chakraborty 1995);

$$\sigma_i = \frac{\sum D_i \, \mathrm{z}^2 q_i^2 N_i}{k_B T \, \mathrm{H_R}} \tag{16}$$

where z_i and N_i are the valence and number of ions of type i, q_i is the elementary charge, k_B is the Boltzmann constant, T is the temperature and H_R is the Haven ratio. The Nernst-Einstein

relation assumes that conductivity is purely ionic and does not take into account the contribution of ionic coupling within the melt. This results in higher predictions of electrical conductivities than observed experimentally. This correlation can be quantified by using the Haven ratio (Le Claire 1970), which is the ratio of the NE–approximated conductivity to the exact value,

$$H_R = \frac{\sigma^{\mathrm{NE}}}{\sigma^{\mathrm{exact}}} \tag{17}$$

The Haven ratio is determined by the diffusion mechanism and typically less than one for ionic solids (Haven and Verkerk 1965, Isard 1999) and greater than one for ionic liquids (Stolwijk and Obeidi 2009, Clay, Kuntz et al. 2012).

Huaiwei and Fei et al. (Huaiwei, Fei et al. 2012) studied the relationship between electrical conductivity and viscosity of melts containing iron oxide in the FeO/Fe_2O_3-SiO_2-CaO-Cu_2O system. This study found that the network formers (SiO_2 and Al_2O_3) increase the viscosity and decrease electrical conductivity while network breakers (such as MgO and CaO) have the opposite effect (Jiao and Themelis 1988, Ducret and Rankin 2002). These properties are interdependent and knowledge of them is important for successful processing of silicate melts.

3. MOLECULAR DYNAMICS (MD)

Molecular dynamics (MD) methods were introduced in the late 1950s by Alder and Wainwright to study the interactions between hard spheres (Alder and Wainwright 1957, Alder and Wainwright 1959). Their relatively simple study yielded insight into important behavioural traits such as phase transitions for simple liquids. However, the first realistic simulations using functional potentials for liquid water were carried out by Rahman and Stillinger (Rahman 1964, Rahman and Stillinger 1971). Briefly stated, MD simulates the real dynamics of a system of interest, from which the time averages of the properties of the system can be obtained. The atomic positions are obtained in sequence through the application of Newton's equations of motion. MD simulations are deterministic in nature, if the state of the system at any future time is known; it can then be predicted from its current state.

MD methods are broadly grouped into two categories based on the atomic model and the resulting underlying mathematical theory that is chosen to represent the physical system. In *classical* MD simulations, molecules and atoms are treated as classical objects, with features similar to a soft ball and elastic stick model. The balls represent atoms and the sticks, bonds. The dynamics of the system are defined by laws that govern classical mechanics. Where classical methods are inappropriate, i.e. where electronic effects such as excited states are important, the system can also be described using quantum mechanics, where solutions to the Schrödinger equation are used to describe both the electrons and nuclei. This approach is called *ab initio* MD. There are two typical practical ways of performing molecular dynamics using the wavefunction, i.e., Born–Oppenheimer molecular dynamics (BOMD) (Köuppel, Domcke et al. 1984) and Car–Parrinello molecular dynamics (CPMD) (Car and Parrinello 1985). In the BOMD approach, only the ground state wavefunction is used and it is variationally determined/minimized at each iteration of the dynamics. The nuclear degrees of freedom are propagated using ionic forces, which are estimated at each time step by approximately solving the electronic problem. On the other hand, CPMD is based on the concept of adiabaticity, where electrons follow atoms adiabatically due to their weights being significantly less than the nuclei. The CPMD approaches allows the use of a quantum mechanical description of the electronic degrees of freedom combined with a classical phase space trajectory involving a fictitious electronic mass parameter (Kuo, Mundy et al. 2006). The wave function is dynamically optimised to be consistent with the changing positions of the atomic nuclei.

The fictitious classical dynamics for electronic orbitals is explicitly introduced in CPMD method eliminating the need for an a priori defined and parameterized potential (Car and Parrinello1985). *Ab initio* MD allows the investigation of the electronic excited states which is not possible when using classical MD. Some examples of the excited states phenomenon which can be investigated using ab inito MD include: fluorescent microscopy, spectroscopy, labelling techniques, chemical lasers, photoactive enzymes, light-harvesting systems, optogenetics, photochemistry (Rydzewski and Nowak 2016).

Modern implementations of *ab initio* MD methods rely almost exclusively on Density Functional Theory (DFT), due to its favourable computational cost and improved accuracy through the careful selection of an appropriate exchange–correlation functional (Frauenheim, Seifert et al. 2000). *Ab initio* MD simulations are an important improvement over classical approaches, however, they are computationally expensive and can therefore only access relatively small systems and relatively short simulation times.

MD describes the solution of the classical equations of motion that is Newton's equations of motion, for a set of atoms or molecules within a simulation box. The Born Oppenheimer (BO) approximation assumes that the heavy nuclei are fixed or stationary and move slowly relative to electrons and electrons are not treated explicitly (Allen and Tildesley 1989, Frenkel and Smit 2001, Leach 2001). Therefore the motion of slow moving nuclei and fast moving electrons can be separated. The interatomic potential in classical MD consists of a set of equations defining the variation of the potential energy of the atomic system (e.g., a molecule or a crystal) with respect to the locations of its component atoms. A series of atom types used in a potential model can define the characteristics of an element in a particular chemical environment. The potential functions can be divided into three categories namely non-bonded, bonded and restraint interactions.

Non-bonded interactions are usually characterised by a repulsion term, a dispersion term and an electrostatic term. Bonded interactions are based on a fixed list of bonded atoms, unlike non-bonded interactions which may change during simulations and usually involve pair wise interactions, but may include 3- or 4-body interactions. For bonded interactions, the potential energy parameters typically include force constants for harmonic motion and structural parameters such as equilibrium bond lengths and equilibrium bond angles.

An atom’s type depends on hybridization, charge and the types of other atoms to which this atom is bonded. The electrons of the molecular system are not considered explicitly, instead,

the calculations are based on the net interactions between electrons and nuclei (Field, Bash et al. 1990). The electronic effects are, however, implicitly included in a force field via its parameterisation. A force field refers to analytical potential energy functions and parameter sets that is used to calculate the interactions between a set of atoms or molecules. This approximation makes classical MD techniques possible and this method is relatively inexpensive computationally and allows simulation of very large atomic systems, up to millions of atoms, for relatively long times of the order of 10^6–10^8 time steps (Schulz, Lindner et al. 2009). The results can only be as good as the force field employed. Also, not taking into account the contribution of electrons means that classical MD cannot treat or simulate chemical problems in which the electronic contribution or effects predominate, including processes such as bond forming and breaking. In such instances, *ab initio* first-principles MD should be used.

The use of quantum theory in classical MD is limited to the construction of the interaction potentials in relation to the BO approximation. The Hamiltonian for a system of *N* interacting atoms is gien in Eq. 11. The contributions of the electrons are included in terms of an effective potential acting on the nuclei. Hence it is possible to treat the atoms as point masses. This is the approach of classical MD as opposed to *ab initio* MD.

Assuming that the classical description is correct, the Hamiltonian, *H*, can be written as a sum of kinetic and potential energy functions,

$$H(r, p) = K(p) + U(r) \tag{18}$$

where

$$r = (r_1, r_2, \ldots\ldots\ldots N)$$

$$p = (p_1, p_2, \ldots\ldots\ldots, p_N)$$

This depends on the generalized coordinates $r = (r_1, \ldots, {}_N)$ and momenta $p = (p_1, \ldots, p_N)$ of each atom. The kinetic energy, *K* is usually defined by Eq. 19as:

$$K = -\frac{1}{2}\sum \frac{p_i^{\,2}}{m_i} \tag{19}$$

where m_i and p_i are the atomic mass and momentum of atom i, respectively. Information regarding the interactions between particles is contained in the pair potential, *U (equation 21)*. If the pair potential defines the particle interaction sufficiently well, it is possible to obtain

equations of motion from *H* that governs the time-evolution of the system. Generally, the equations of motion are classically defined, i.e., in Newtonian form, but can also be presented in Hamiltonian or Lagrangian form.

The classical MD approach for simulating materials involves the definition of interatomic potential functions to model the forces acting between the atoms. The total potential energy (*U*):

$$U = \sum v_i(r_i) + \sum \sum v_2(r_i, r_j) + \sum \sum \sum v_3(r_i, r_j, r_k) \quad (20)$$

can generally be broken down into pair, three-body, and higher order many body terms, depending on the properties of the system under study. The first term, $v_i(r_i)$, represents the effect of an external field on the system; the remaining terms represent inter-particle interactions. The interactions are to be modelled by pair wise and three body potentials, which by definition are functions of the positions of the nuclei. The pair potential depends only on the magnitude of the pair separation $r_{ij} = |r_i - r_j|$. The potential energy is usually written in terms of the distances between the atomic particles only, i.e,:

$$U(r_{ij}) = \sum_i \sum_{j>i} \Phi(r_{ij}) \quad (21)$$

where $\Phi(r_{ij})$ is the pair wise interaction. The potential to be implemented is determined by the system under investigation. The resulting force field is then expressed as a sum of pairwise interaction terms that represent changes of the (i) chemical bond lengths and bond angles of a molecule as harmonic or non-harmonic spring functions; and (ii) torsions as periodic functions (dihedral angles, or torsional rotation of atoms around a central bond); (iii) non-bonded electrostatic and van der Waals intra- and inter-molecular interactions, (iv) out –of-plane terms which are treated harmonically, and (v) the cross terms.

In a MD simulation, the atoms are allowed to interact for a period of time and the trajectory (the set of snapshots) of atoms in the simulation box is collected and analysed. Each trajectory is obtained by numerically solving Newton's equations of motion. For a known potential, the forces can be derived from the gradient of the potential with respect to the atomic displacements:

$$F_i = -\nabla r_i U\left(r_{i,}.....,r_N\right) = m_i a_i \tag{22}$$

where F is the force, U is the potential energy, N is the number of atoms in the system, r_i is atomic position, m_i and a_i are the mass and acceleration of atom i, respectively. If instantaneous atomic positions, r_i, are known at one time, t_0, the time evolution of the trajectories of the system can be computed at any successive time, t, by integrating the classical equations of motion as mentioned above. These equations can be solved using different numerical schemes, such as the Verlet and Leapfrog schemes (Verlet 1967), discussed next.

3.1. Integration of the equation of motion

The ability of an MD integrator to conserve the system's total energy over a long time interval is the key indicator of its numerical accuracy (Praprotnik and Janezic 2005). The second-order Leapfrog algorithm, which is defined by the Split Integration Symplectic Method (SISM), and its variants have been used for solving the classical equations of motion (Janezic, Praprotnik et al. 2005). However the Single time step (STS) explicit Verlet integrators are often employed in molecular dynamics simulation owing to their simplicity and ease of coding and implementation (Batcho, Case et al. 2001). The Verlet family has become the method of choice owing to its excellent conservation properties. To satisfy accuracy and stability for STS approaches, a time step of 0.5–1 fs is usually recommended (Batcho, Case et al. 2001).

3.2. Integration algorithms

The potential energy is a function of the atomic positions, often expressed in generalised Cartesian coordinates, X (X_1, X_2, X_3……X_{3N}, where N is the total number of atoms in the system). Since the equations of motion are coupled, an analytic solution is not possible and hence one needs to solve the differential equations numerically. The most common are Verlet, Leapfrog, Velocity-Verlet and Beeman's algorithm. Some important considerations choosing an algorithm is to ensure that the selected algorithm conserves energy and momentum, is computationally efficient and also permits a long time step for integration. The focus was on the Verlet and Velocity Verlet algorithms (Verlet 1967)), since these are the most popular time integration algorithms and are simpler to implement. All the above mentioned algorithms assume that the positions and dynamic properties such as velocity, acceleration and momentum can be approximated using Taylor series expansions. Integrating the equations of motion can

result in trajectories that describe the positions, velocities and acceleration of each atom as they change with time. After obtaining the positions, velocities and acceleration of each atom, the state of the system can then be predicted at any subsequent time. By solving the differential equations one obtains a trajectory, the integration can be broken down into small stages, i.e., the net force in the configuration at time t is the vector sum of its interactions with other particles. Once the net force on each of the atoms is known, the velocities can be estimated from Newton's law assuming that the forces are constant over a small time step and the new positions of each atom can be updated through very accurate integration algorithms. The Verlet algorithm proceeds in two steps. First, the new positions are calculated by:

$$r(t+\Delta t) = r(t) + (\Delta t)v(t) + \frac{1}{2}(\Delta t)^2 a(t) \tag{23}$$

where Δt denotes the size of the time step. In a second step, the velocities at $t + \Delta t$ are obtained by:

$$v(t+\Delta t) = v(t) + \frac{1}{2}\Delta t[a(t) + a(t+\Delta t)] \tag{24}$$

$$v(t+\frac{1}{2}\Delta t) = v(t) + \frac{1}{2}\Delta t a(t) \tag{25}$$

$$v(t) = \frac{[r(t+\Delta t) - r(t-\Delta t)]}{2\Delta t} \tag{26}$$

$$v(t+\frac{1}{2}\Delta t) = \frac{[r(t+\Delta t) - r(t)]}{\Delta t} \tag{27}$$

where v is the velocity, which is the first derivative of position with respect to time and a is the acceleration, which is the second derivative of position with respect to time. Between these two steps, the forces acting on an atom at $t + \Delta$t which change their relative positions each time frame are calculated at each time step. This algorithm is a symplectic integrator and hence, it conserves energy and total momentum of the system. The Verlet algorithm uses the positions and acceleration at time t and positions at the previous step $r(t - \Delta t)$ to calculate the new positions at time $t + \Delta t$, namely $r(t + \Delta t)$. The relationship between these quantities and velocities at time t can be written as follows:

$$r(t+\Delta t) = r(t) + v(t)\Delta t + \frac{1}{2}a(t)(\Delta t)^2 \tag{28}$$

$$r(t-\Delta t) = r(t) - v(t)\Delta t + \frac{1}{2}(\Delta t)^2 a(t) \tag{29}$$

Adding the two expressions, we finally obtain:

$$r(t+\Delta t) = 2r(t) - r(t-\Delta t) + a(t)\Delta t^2 \tag{30}$$

A problem with the Verlet algorithm is that it does not generate velocities explicitly; velocities are only available once the positions have been computed at the next step. Although they are not needed for time evolution, sometimes their knowledge is necessary, for example, for calculating properties of the system under study. A simple approach is to divide the difference in positions at time $t + \Delta t$ and $t - \Delta t$ by $2\Delta t$,

$$v(t) = \left[\frac{r(t+\Delta t) - r(t-\Delta t)}{2\Delta t}\right] \tag{31}$$

or alternatively, the velocities can be estimated at the half-step, $t + 1/2\Delta t$:

$$v(t+\frac{1}{2}\Delta t) = \left[\frac{r(t+\Delta t) - r(t)}{2\Delta t}\right] \tag{32}$$

Another disadvantage of this algorithm is that positions at $r\ (t + \Delta t)$ are obtained by adding a small term, $\Delta t^2 a(t)$, to the difference of two much larger terms, $2r(t)$ and $r(t - \Delta t)$. This may lead to a decrease in accuracy owing to potential numerical errors. Other variants have been developed to overcome the shortcomings of the simple Verlet algorithm, e.g., the velocity Verlet and Leapfrog algorithms. These algorithms give rise to exactly the same trajectory, but differ in terms of variables that are stored in memory and at what stage they are saved. The velocity Verlet algorithm computes positions at time $t + \Delta t$ using only positions at time t and their time derivatives. It computes positions, velocities and acceleration at time $t + \Delta t$.

$$r(t-\Delta t) = r(t) + v(t)\Delta t + \frac{1}{2}(t)(\Delta t)^2 \tag{33}$$

$$v(t+\Delta t) = v(t) + \frac{1}{2}\Delta t\left[a(t) + a(t+\Delta t)\right] \tag{34}$$

The implementation of the velocity Verlet algorithm is a 3-stage procedure and calculating the new velocities require the acceleration at both $t + \Delta t$. Thus, in the first step, the positions at $t + \Delta t$ are calculated according to equation 23 using the velocities and acceleration at time t. The velocities at time $t + 1/2\Delta t$ are then determined using the following expression:

$$v(t+\frac{1}{2}\Delta t) = v(t)+\frac{1}{2}a(t)\Delta t \tag{35}$$

New forces are next computed from the current position set at time t, thus giving *a(t + Δt).*

In the third and final step, the velocities at time $t + \Delta t$ are determined using the following expression:

$$v(t+\Delta t) = v\left(t+\frac{1}{2}\Delta t\right)+\left[\frac{1}{2}a\Delta t(t+\Delta t)\right] \tag{36}$$

The leapfrog scheme involves calculation of atomic velocities at half time steps, i.e., it produces the position r_i at integer time steps and the velocity v_i at half integer time steps so that r_i and v_i "leapfrog" over each other. The leapfrog algorithm uses the following relationships:

$$v(t+\frac{1}{2}\Delta t) = v\left(t-\frac{1}{2}\Delta tv\right)+\left[a(t)\Delta t\right] \tag{37}$$

$$r(t+\Delta t) = r(t)+\Delta tv\left[\left(t+\frac{1}{2}\Delta t\right)\right] \tag{38}$$

In the implementation of this algorithm, the velocities $v(t + 1/2t)$ are first calculated from the velocities at time $t - 1/2\Delta t$ and the accelerations at time *t*. The positions $r\ (t + \Delta t)$ are then deduced from the velocities just calculated together with the positions at time $r(t)$. The velocities at time *t* are then calculated from the following expression:

$$v(t) = \frac{1}{2}\Delta tv+\left[v\Delta ta(t)\right] \tag{39}$$

The velocities in the leapfrog algorithm are first calculated over positions at time $t + 1/2\Delta t$. Then, the resulting velocities are used to calculate positions r, at time $t + \Delta t$. This results in velocities leaping over the positions, and then positions leaping over the velocities. This algorithm has two advantages over the standard Verlet algorithm: velocities are explicitly included and it also does not require the calculation of the differences between small and large numbers. Its disadvantage is that the positions and velocities are not synchronized. This then does not allow the kinetic energy contribution to the total energy to be calculated at the same time as the positions are defined from which the potential energy is determined. The velocity Verlet algorithm provides both the atomic positions and velocities at the same instant of time and therefore is regarded as a more complete form of the Verlet algorithm than the leap frog approach (Biswas, Djomehri et al. 2005).

3.3. Interatomic interactions and force fields

The interaction of atoms during MD simulations is described by a force field or interatomic potential. Force fields are used to calculate the forces acting on the particles, which in turn are used to solve the equations of motion. For classical MD, empirical potentials are used to describe inter-atomic interactions, while *ab initio* MD describe the electronic interactions which entails calculation of forces acting on the nuclei from the electronic structure calculations performed on the fly while generating MD trajectories. This ensures that the electronic contributions are considered as active degrees of freedom. As mentioned earlier, the success of any atomistic simulation depends on how accurately it predicts the properties of the systems of interest as well as its transferability. Force fields are used to describe physical interactions such as bond stretching, bond angle bending, torsion and non-bonded interactions. The potential energy function that describes the inter-atomic interactions within the simulation box is therefore a sum of energy terms, and depends on the atomic positions of the *N* atoms in the system. Since the interactions can be categorized into bonded and non-bonded interactions, the potential energy can be written as equation 20.

Potentials that only use v_2 (the second term of equation 20) and neglect any higher term contributions are called pair potentials. These potentials are characterised by their simplicity and can provide an accurate description for some materials if used within their range of applicability or region in which they were parametrised. The simplicity of these potentials dates back to times when the computer resources were severely limited. The v_2 form of the interacting potential is normally denoted as a single function $\varphi(r_{ij})$. Usually systems consist of more than one type of atom and are thus labelled as $\varphi(_{s\_i\_s\_j})$, where s_i denotes the species of atom *i*. The s in the index of the potential function φ is usually omitted for reasons of simplicity and we therefore write φ_{ij}. The pairwise potentials such as Lennard-Jones, Buckingham and the Morse potentials can accurately describe interactions between a pair of atoms. These potentials incorporate a description of a repulsive part due to the Pauli Exclusion Principle and an attractive part to mimic van der Waals forces. When the v_3 or higher terms of Equation 20 are used, the potential forms are referred to as three- or many-body interactions. An overview of empirical many-body potentials is given by Erkoç (Erkoç 1997).

The choice of inter-atomic potential is the central core of molecular dynamics simulations since they determine the success or failure of simulations (Schaible 1999). An interaction results from the subtle interplay of electrons and nuclei (Hernández 2008) and can be described using

a potential function that depends on the relative atomic positions and a series of parameters. These parameters are then fitted in order to reproduce as closely as possible some relevant properties of the system or quantum mechanical data.

In *ab initio* MD based approaches, the forces acting on the nuclei are computed from electronic structure ‘‘on the fly’’ as the simulation proceeds (Kaplan, Murrell et al. 2002, Malerba, Ackland et al. 2010). This offers the ability to calculate dynamics based on forces which are not parameterised for particular systems. However, *ab initio* techniques are computationally expensive, and are therefore limited to systems containing less than 100 atoms and in simulations with durations less than 100 ps (Elstner, Frauenheim et al. 2000, Malerba, Ackland et al. 2010) . With improvements in computing and high performance computing (HPC), bigger systems and timescales are nowadays possible. The *ab initio* technique employs the Self Consistent Field (SCF) equations which are parametrically dependent on the atomic positions. The computational time for solving these SCF equations increases rapidly with the number of electrons in the system and hence this type of technique rapidly becomes unmanageable for larger systems and longer time scales.

One of the requirements for the potential model is that it should have some degree of transferability. A potential model developed to incorporate available experimental data for model compound is considered transferable if it can be applied successfully to MD predictions of other systems belonging to the same chemical subgroups. Parameterisation of the potential model is a difficult task and the combination of required parameters may be large.

3.4. Typical potential models

The general establishment of the starting equation for non-binding pair potential for spherically symmetric systems, i.e., Φ(r) = Φ(r) with r = |ri − rj | is of the following form (Steinhauser 2007, Steinhauser and Hiermaier 2009):

$$\Phi_{nb}(r) = \Phi_{coulumb}(r) + \left(\frac{C_1}{r}\right)^{12} - \left(\frac{C_2}{r}\right)^{6} \tag{40}$$

C_1 and C_2 are parameters of the repulsive and attractive interactions, respectively, and the first term is the electrostatic contribution between the particles and is given by the following expression:

$$\Phi_{coulomb}(r) = \frac{1}{\varepsilon}\kappa \cdot \sum_{i} \sum_{i>j} \frac{z_i z_j e^2}{\left|\vec{r}_i - \vec{r}_j\right|} \tag{41}$$

The constant $\kappa = 1$ is in the cgs-system of units and ϵ is the dielectric constant of the medium. The z_i denotes the charge of individual ions and e is the electric charge of an electron. The inclusion of Coulomb interactions permits ionic bonds to be modelled.

The Lennard-Jones LJ 6-12 potential for the interaction between two particles with interatomic distance $r = |\vec{r}i - \vec{r}j|$ is most often used (Lim 2003, Tadmor and Miller 2011). The LJ 6-12 potential has been used to simulate two neutral atoms which are bound by van der Waals interactions and has the form:

$$\Phi_{L,J}(r) = 4\varepsilon\left[\left(\frac{\sigma_0}{r}\right)^{12} - \left(\frac{\sigma_0}{r}\right)^{6}\right] \tag{42}$$

where σ_0 is the atomic diameter, and ε, the well depth. The two-part Lennard-Jones potential includes an attraction proportional to $1/r^6$, and repulsion proportional to $1/r^{12}$. It is mathematically equivalent to Equation 41 if the Coulombic term is excluded.

3.5. Periodic boundary conditions (PBC)

During MD simulations, molecules at the surface of the simulation box experience different forces than those in the bulk (Haile 1992, Rapaport 2004). In order to avoid surface effects and conserve the composition of the simulation cell, periodic boundary conditions are commonly applied. This technique allows the use of relatively small system sizes; hence simulation times can be significantly reduced. In periodic boundary conditions (PBC), a supercell is employed and one has to track only the motion of the N particles present in this primary cell. The supercell is surrounded by infinitely replicated, periodic images of itself as shown in Figure 9. Particles not only interact with those in the same supercell (only interactions within a specified distance or cut off radius are included in MD as discussed later) but also with particles in the adjacent images of the supercell. The particles are, however, contained within the primary simulation box. When a particle leaves one side of the box, it re-enters from the opposite side keeping the number of atoms in the central box constant.

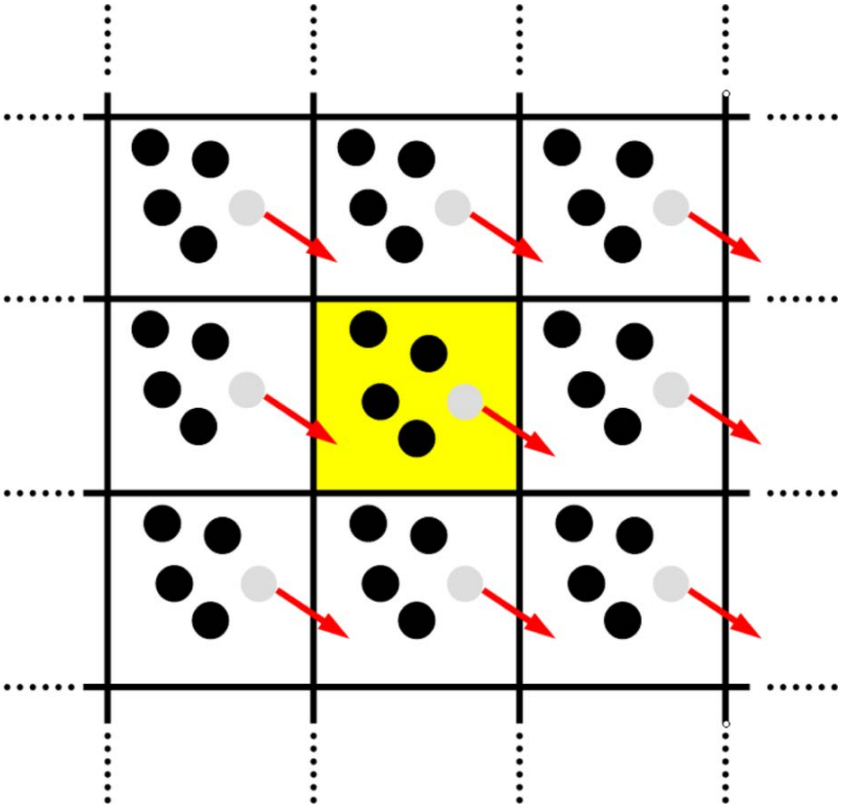

Figure 9. Two-dimensional schematic of periodic boundary conditions. The particle trajectories in the central simulation box are copied in every direction (Steinhauser and Hiermaier 2009).

PBC are used in conjunction with the minimum image convention (MIC) for short-range forces. The MIC ensures that each particle in the super cell is interacting not only with other particles in the super cell, but also with particle images in adjacent cells. Since self-interactions need to be avoided an appropriate choice of cell size and cut off radius (r_c) is required – for example when a cubic simulation cell is used, the cell must have a side length at least twice as large as r_c. This also prevents duplicate interactions. Using the minimum image convention ensures that the distance between two particles varies continuously as particles move out of the central simulation box and reappear at the opposite side.

3.6. Long range interactions

To obtain the initial energy of a system of atoms or molecules, the non-bonded interactions need to be calculated between each atoms pairs and some interactions, such as Coulombic interactions, may be long-range in nature. Whereas non-bonded interactions may be weak between each individual pair, they make an important contribution to the overall energy of the system. Coulombic forces play an important role in ionic systems, but are problematic because

they are long-ranged and decay as 1/*r* (where r is the interatomic separation). Theoretically, all molecular interactions can be derived from Coulomb's law and the principles of quantum mechanics, both of which are included in the Schrödinger equation.

Most force fields in use today include describe electrostatic interactions using classical formulations and point charges because at long range, complex interactions having their origin in QM are negligible, and molecular interactions can therefore be well approximated classically. Since non-bonded dispersion and repulsion interactions have a relatively short range and decay rapidly, the calculation of van der Waals interactions can be well approximated by only including interactions between neighbouring pairs within a typical cut off radius (r_c) of between 8 and 10 Å. The long-range electrostatic interactions, however, do not decay rapidly and convergence may be slow since the number of interaction terms increase with r^2. Hence a similar cut off approximation is inappropriate because non-negligible force and energy contributions occur beyond r_c. To overcome this problem Ewald summation is employed. The sum over all pairs can be rewritten into sums over all ions, with a factor 1/2 in front of the sum to avoid double counting.

$$U = \frac{1}{2}\sum_{n}^{l}\sum_{i=1}^{N}\sum_{j=1}^{N}\frac{q_i q_j}{r_{ij,n}} \tag{43}$$

U is the total Coulomb interaction energy, *n* is the box index vector and *l* represents the characteristic length of the supercell. The charges on the atoms are q_i and q_j , respectively, $r_{ij,n}$ is the real distance between the charges and not the minimum image and N is the total number of ions in the system. The Ewald summation is used to handle long range interactions in periodic boundary conditions (Ewald 1921, Darden, York et al. 1993, Essmann, Perera et al. 1995, Toukmaji and Board 1996). The Ewald sum involves splitting the slowly convergent equation 43 into two series which can be computed much faster.

This involves splitting the interaction 1/r as

$$\frac{1}{r} = \frac{f(r)}{r} - \frac{1-f(r)}{r} \tag{44}$$

An error function which decreases monotonically as r increases is the chosen function and is defined by $f(r) = erfc(\alpha r)$ Here α is the Ewald splitting parameter and we therefore have the well-known Ewald formula for the energy of the super cell . The Ewald summation is therefore written as the sum of four contributions, namely $U^{(r)}$ the short real space contribution, $U^{(k)}$ the

long rang contribution calculated in reciprocal space contribution, $U^{(self)}$ the self-energy, and $U^{(dipolar)}$ which accounts for the dipolar correction.

$$U = U^{(r)} + U^{(k)} + U^{(self)} + U^{(dipolar)} \tag{45}$$

A neutral periodic system is normally modelled using charged point ions mutually interacting via the Coulombic potential. The Ewald summation makes two amendments to this model. First, at long range each ion is effectively neutralized by the superimposition of a spherical Gaussian cloud of opposite charge centred at each ion. The combined assembly of point ions and Gaussian charges becomes the real space part of the Ewald sum, which is now short-ranged and treatable within the minimum image convention. Second, another set of Gaussian charges is superimposed with the same charges as the original point ions and again centered at the point ions, which nullifies the effect of the first set of Gaussians. The potential due to the second set of Gaussians is obtained from Poisson's equation, which is solved as a Fourier series in reciprocal space. The complete Ewald summation requires an additional correction term, known as the self-energy correction, which arises from a Gaussian acting on its own site, and is calculated as a constant. Ewald's method therefore replaces an infinite non-converging summation in real-space by two rapidly converging summations: one in real-space and another in reciprocal-space, with the addition of the self-energy correction.

3.7. Thermostats and barostats

In the process of running a MD simulation, the temperature of the system has to be carefully controlled to reduce the fluctuations occurring in the system. The sources of fluctuations are drift during equilibration, drift as a result of force truncation (owing to omission of interactions beyond r_c) and integration errors, and heating due to external frictional forces. In this work I used the weak coupling scheme of Berendsen (Berendsen, Postma et al. 1984) and the extended ensemble Nose–Hoover scheme (Evans and Holian 1985) for temperature control. The Berendsen thermostat is efficient for relaxing a system to the target temperature and conserving the momentum, but once your system has reached equilibrium, it might be more important to probe a correct canonical ensemble and conserve energy of the system which can be achieved using the Nose–Hoover scheme.

3.8. Berendsen temperature coupling

The Berendsen algorithm mimics weak coupling with first–order kinetics to an external heat bath at a given temperature T_0. In this algorithm, the deviation of the temperature of the system from T_0 is slowly corrected according to:

$$\frac{dT}{dt} = \frac{T_0 - T}{\tau} \tag{46}$$

This implies that temperature decays exponentially with the time constant τ. The advantage of this coupling technique is that it can be easily varied and adapted according to the user's requirements.

Heat flow into and out of the system is achieved by scaling the velocities of each particle at each time step with a time-dependent factor λ, given by:

$$\lambda = \left[1 + \frac{\Delta t}{\tau_T} \left\{ \frac{T_0}{T\left(t - \frac{\Delta t}{2} \right)} - 1 \right\} \right]^{\frac{1}{2}} \tag{47}$$

where Δt is the time step, parameter τ_T is the temperature coupling constant and is close to the time constant of the temperature coupling, τ, but not exactly equal; τ is given by:

$$\tau = \frac{2C_v \tau_T}{N_{df} k} \tag{48}$$

where C_v is the total heat capacity of the system, k is the Boltzmann constant and N_{df} is the total number of degrees of freedom. The change in kinetic energy due to scaling of velocities is redistributed between both kinetic and potential energy, hence the change in temperature is less than the scaling energy, resulting in $\tau \neq \tau_T$. To compute the scaling factor, the temperature T is required at time t. However this is not available at this stage in the integration algorithm. Therefore in practice, the temperature at the previous time step is used, and this is acceptable because the coupling time constant is much longer than one time step. The Berendsen algorithm is stable up to $\tau T \approx \Delta t$.

3.9. Nosé-Hoover temperature coupling

The efficiency of the Berendsen weak coupling algorithm is generally accepted in terms of its efficiency for relaxing a chemical system to its target temperature. However, once the system has reached equilibrium, it is important to probe the correct canonical ensemble. Weak coupling schemes are however unable to probe the canonical ensemble environment. In Nosé-Hoover coupling (Evans and Holian 1985, Hoover 1985) the system Hamiltonian is extended by introducing a thermal reservoir and friction term in the equations of motion. This frictional force is equal to the product of each particle's velocity and fiction parameter ξ. This heat bath variable ξ is a fully dynamic quantity with its own equations of motion. The equations of motion for an atom are given by:

$$\tau \frac{d^2 r_i}{dt^2} = \frac{F_i}{m_i} \xi \frac{dr_i}{dt} \tag{49}$$

The heat bath parameter ξ is as:

$$\frac{d\xi}{dt} = \frac{1}{Q}\left(T - T_0\right) \tag{50}$$

where, T_0 denotes the reference temperature and T is the current instantaneous temperature of the system. The constant *Q* is a mass parameter of the reservoir, which determines the strength of the coupling in combination with the reference temperature. The difference between the Berendsen and the Nosé-Hoover algorithms is that the weak coupling associated with the Berendsen thermostat produces a strongly damped exponential relaxation, while the latter approach gives an oscillatory relaxation. In contrast to exponential relaxation, the oscillatory relaxation means that the time constant possible for the latter is normally 4 to 5 times larger than the relaxation time used with weak coupling.

3.10. Pressure coupling

Similar to temperature coupling the change in size of the simulation cell may be dynamically adjusted by coupling the system to a pressure bath, that is barostat, to obtain the desired pressure. Again the Berendsen algorithm can be used to scale the coordinates and simulation cell vectors at appropriate time steps. This can also be combined with temperature coupling methods mentioned above.

$$\frac{dP}{dt} = \frac{P_0 - P}{\tau} \tag{51}$$

The scaling matrix is given by:

$$\chi = 1 - \beta_T \frac{\Delta t}{\tau_p}\left(P_d - P_0\right) \tag{52}$$

where τ_p is the time constant for the coupling, P_0 is the reference pressure and P_d is the current pressure, Δt is the time step, β_T is isothermal compressibility of the system.The isothermal compressibility is generally not known during simulation and it does not affect the average pressure only the non-critical time constant of pressure relation and therefore it is usually estimated during the simulation (van der Spoel, Lindahl et al. 2008). Most liquids have a isothermal compressibility similar to that of water at room temperature which is 4.6×10^{-10} Pa^{-1} (van der Spoel, Lindahl et al. 2008).

4. PROPERTY CALCULATIONS

4.1. Correlation functions

The correlation function is a powerful analysis tool in MD simulations which can be used to analyse time dependent data. A direct dynamic output of the simulation is the numerical trajectory, i.e., snapshots, which may include coordinates, velocities and forces taken at equal time intervals τ (Allen and Tildesley 1989, Frenkel and Smit 2001). For any dynamic variable, $A(\tau)$, the time correlation function, C_A, is defined as:

$$C_A(t) = \langle A(\tau)A(0) \rangle \tag{53}$$

This function correlates the property $A(\tau)$ to itself at two different times separated by the time interval τ, averaged over the whole trajectory. Similarly, an ensemble average between two quantities A and B, the cross correlation function, is given by $C_{AB}(\tau)$ as a function of their separation in time τ :

$$C_{AB}(\tau) = \langle A(\tau)B(0) \rangle \tag{54}$$

In practice, the correlation function is calculated by averaging the terms $\langle A(\tau + s)B(s) \rangle$ while moving s along the trajectory (Becker, MacKerell Jr et al. 2001). The time difference, $\boldsymbol{\tau}$, is chosen such that the time difference between the onsets of two consecutive time frames have their initial states not correlated to each other. If the correlation function decays slowly, the calculation of properties that are represented in terms of correlation function can be computationally expensive especially in terms of requiring long MD runs.

Macroscopic transport coefficients such as diffusion coefficients, viscosities and electrical conductivities can be represented by Green-Kubo integral formulas or their corresponding Einstein relations using time-correlation function theory.

$$\gamma = \int_0^\infty \left\langle \dot{A}(\tau)\dot{A}(0) \right\rangle dt. \tag{55}$$

In this Green-Kubo integral above γ is the transport coefficient and A is a variable appearing in the perturbation term in the Hamiltonian. An associated expression is the Einstein formula:

$$\gamma = \frac{1}{2}_{t\to\infty} \frac{d}{dt} \left\langle [A(\tau) - A(0)]^2 \right\rangle \tag{56}$$

which is valid for relatively large values of t compared to the correlation time of A.

4.2. Radial distribution functions (RDF)

It is customary in MD simulations to also examine static properties of atomic systems. The radial distribution function (RDF) describes how density varies as a function of distance from a reference particle and can therefore be used to distinguish between crystalline and amorphous materials. The RDF describes the structure of the system in real space and is given by:

$$g(r) = \frac{V}{4\pi r^2 N^2}\left\langle \sum_{i}^{N}\sum_{j\neq i}\delta(\vec{r} - \vec{r}_{ij}) \right\rangle \tag{57}$$

where V is the volume of the MD cell, N is the number of particles, r is position at which the RDF is being calculated and the brackets denote an ensemble average. Thus, $g(r)$ is the probability of finding a particle at a distance r away from a reference position. RDF curves are shown in Figure 10. In fluids where r is much larger than the range of the inter-particle potential, the RDF approaches the ideal-gas limit of 1, that is, one is equally likely to find the particle at this or any larger distance, i.e., $\lim_{r\to\infty} g(r) = 1$.

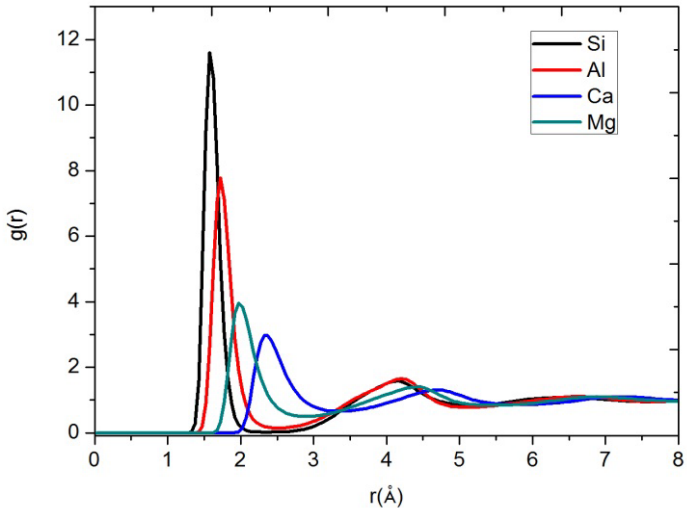

Figure 10. The ion–oxygen pair distribution function curves (PDF) showing the first peak and the minima following the peak representing the bond length and cut off values of the cation-oxygen nearest neighbour for Si–O, Al–O, Mg–O and Ca–O in the N1 system in Table 4.

The meaningful interpretation of the RDF is restricted to a maximum value of r, typically half the size of the box. Above this value, unresolved peaks appear as a result of the multiple counting of the interparticle distances and self–correlation contributions. A more detailed

investigation of the structure of slag systems can be obtained from radial distribution function (RDF) analyses of spatial atomic correlations.

4.3. Coordination numbers

In order to understand the structure and transport properties of materials, it is important to investigate the local environment of an atom in a disordered structure, especially at high temperatures. The coordination number (CN) is given by the area under each peak in the RDF curve. In other words, CN is computed as the running integral of the radial distribution function $g(r)$ (red curve in Figure 11) given by:

$$N(r) = 4\pi\rho\int_0^r r^2\, g(r)dr \tag{58}$$

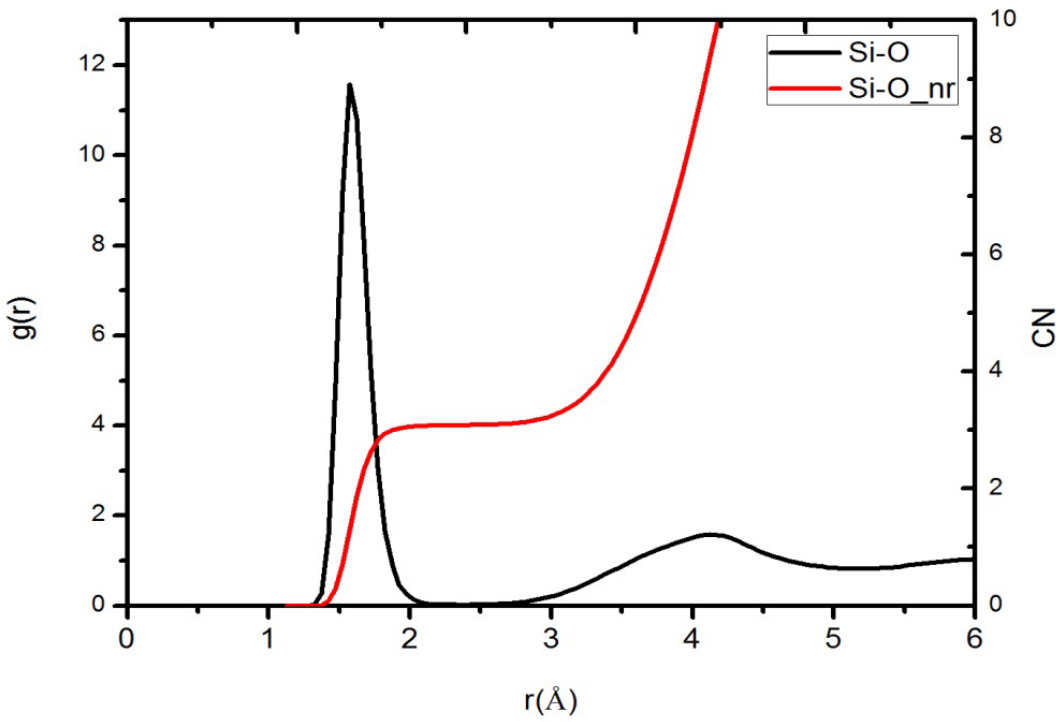

Figure 11. Si–O partial pair correlation functions (black) and average coordination numbers (red lines).

4.4. Self–diffusion coefficients

The self–diffusion coefficient D_i of a selected ion i was calculated from the average mean square displacement (MSD) using the Einstein relation (Allen and Tildesley 1989),

$$D_i = \frac{1}{6}\lim_{t\to\infty}\frac{d}{dt}\left\langle\sum_i^N[\vec{r}_i(t)-\vec{r}_i(0)]^2\right\rangle \tag{59}$$

where N is the total number of ions of type i and $\vec{r}_i(t)$ is the displacement of such an ion at time t. The angle brackets indicate an ensemble average. After an initial period of ballistic motion, the MSD increases linearly with time. In this linear regime, the slope of the curve gives the self–diffusion coefficient. The MSDs were calculated using the full 5 ns of the simulation runs under the NVT canonical ensemble (constant number of particles, N, constant volume, V and constant temperature, T), with the fitting done between 1 ns and 5 ns, the full computational details are stated in section 5.1. Fits over shorter intervals were also attempted, but this did not have a significant effect on the results. In calculating the ensemble averages, multiple time origins were used to improve statistics further. In addition, each simulation was repeated five times and the resulting diffusion coefficient reported as the average. The reported uncertainties were calculated as standard deviations for each simulated composition.

4.5. Ionic conductivities

The ionic conductivities were calculated using the following Einstein relationship,

$$\sigma^{\text{exact}} = \frac{e^2}{6kTV}\lim_{t\to\infty}\frac{d}{dt}\left\langle\sum_i^N\sum_j^N z_i z_j[\vec{r}_i(t)-\vec{r}_i(0)][\vec{r}_j(t)-\vec{r}_j(0)]\right\rangle \tag{60}$$

where k is the Boltzmann constant, T the temperature, e the elementary charge, V the simulation box volume, z_i the charge of ion i and $\vec{r}_i(t)$ the displacement vector of ion i at time t. The double summation is performed over all N ions in the simulation. Ionic conductivities were determined from the slope of the ensemble averaged quantity over 5 ns, and fitted to a 500 ps linear regime. Again, the values reported here are averages with corresponding standard deviations over at least five separate (i.e., with random starting positions) simulations. The Einstein expression involves a double summation over all ions i and j. If the cross terms are neglected, the more familiar Nernst–Einstein (NE) expression results, giving the conductivity in terms of a sum of the diffusion coefficients of each ion type (Hansen and McDonald 2006).

$$\sigma^{\text{NE}} = \frac{e^2}{kTV}\sum_j n_j z_j^2 D_j \tag{61}$$

This expression is a sum over ion types j, and n_j is the total number of ions of this type. This formulation assumes independent migration of ions and neglects correlated motion.

4.5. Analysis tools

All structural analyses and transport property and model development calculations were done using codes distributed with DL_POLY version 2.20 (Smith and Forester 1996) and supplemented with additional FORTRAN codes written in the Scientific Computing Research Unit (SCRU) at UCT (Mongalo, Lopis et al. 2016). In addition, R libraries were used for model development (R Core Team 2013).

5. RESULTS

This section presents a detailed analyses of the structural and transport property data for the ionic silicate slag systems, obtained through MD simulations. The relationship between the slag structure and its transport properties is a central issue of the present study. Electrical conductivities of slags were taken from literature as reported by Nesterenko and Khomenko as well as Hundermark (Nesterenko and Khomenko 1985, Hundermark 2003). The slags systems were simulated at the experimental temperatures of 1823 K as reported in the Slag Atlas and by Hundermark (Keene, Mills et al. 1995, Hundermark 2003). After computing the phase–space trajectory for a system of atoms, statistical analysis was carried out to extract the static and dynamic properties of the systems studied. The focus was on slag systems of varying basicity. The compositions of the slag systems by Nesterenko and Khomenko (Nesterenko and Khomenko 1985) are shown in Table 4 and were chosen because the experimental values were provided in literature.

Table 4. Composition of the slag systems in terms of weight percentages, number of atoms in the simulation boxes, and the basicity

Slag	wt% Al_2O_3	wt% CaO	wt% MgO	wt% SiO_2	N_{Si}	N_{Al}	N_{Ca}	N_{Mg}	N_O	Basicity[†]
N1	5	40	6	49	396	48	346	72	1282	1.00
N2	5	43	6	46	372	48	372	72	1259	1.20
N3	5	40	9	46	372	48	346	108	1270	1.15
N4	5	40	12	43	347	48	346	145	1257	1.32
N5	5	49	6	40	323	48	424	72	1214	1.43
N6	5	43	12	40	323	48	372	145	1235	1.49
N7	5	52	6	37	299	48	450	72	1192	1.62
N8	5	49	9	37	299	48	424	108	1202	1.65
N9	5.5	50.5	9	35	275	48	424	108	1154	1.78

[†]Basicity = (CaO +MgO)/(Al_2O_3 +SiO_2)

5.1. Computational details

Cubic simulation boxes were constructed consisting of no less than 2000 and no more than 3000 atoms, based on an approximate mass density and targeting a minimum side dimension of 32 Å. Initial atomic coordinates were randomly generated using the program PACKMOL (Martínez, Andrade et al. 2009). Given the random starting configurations, the simulation protocol was initiated with relatively long equilibration runs of at least 6 ns at 1823 K and 1 atm pressure in the isothermal–isobaric ensemble (NPT), followed by further simulation for 6 ns in the canonical (NVT) ensemble at the same temperature. In each case the 1st ns was discarded as equilibration within each ensemble. Temperature and pressure control was achieved using a Berendsen thermostat and barostat with relaxation times of 1.0 and 3.0 ps, respectively (Berendsen, Postma et al. 1984). A Nose–Hoover thermostat was used for the NVT simulations, with relaxation time of 2 ps (Hoover 1985). The atomic positions were updated using a leapfrog integrator with a time step of 1 fs (Allen and Tildesley 1989). A cut off radius of 10 Å was used for the van der Waals interactions while electrostatic interactions were calculated using the Ewald summation technique with an accuracy of 1×10^{-6} (Allen and Tildesley 1989). Atomic positions were saved at a frequency of 1000 (i.e., 1 ps) time steps. The initial structures were generated randomly with proper composition and densities, in cubic simulation boxes, with initial constraints of shortest interatomic distance to avoid atoms being too close to each other.

The system sizes used in this work were chosen to strike the balance between what is reported in literature, Pedone et. al. used 1536 atoms and Guillot and Sator used 1000 atoms for their simulations. The number of systems which were simulated in this work were more than 2000 in total, to save time, the system sizes were constrained to be between 2000- 3000 atoms. This number of atoms also falls in same range of atoms of work by Dufils et al. and Lacks et al. (Lacks, Rear et al. 2007, Dufils, Folliet et al. 2016) in which they use system sizes of 1000 to 3000 atoms for simulating the silicate melts. MD simulations of systems with 2000 - 3000 atoms took between 18 and 24 hours average, whereas those consisting of 6000 atoms took approximately 27 hours. All calculations were run on Intel Xeon processors with 24 cores.

5.2. Choice of force field used

Two force fields based on different functional forms were tested on how well they predict the properties of slags. Both these potential models have been used in the literature to describe slag-like silicate systems (Pedone, Malavasi et al. 2006, Matsui 1996). The first potential is a pairwise Morse potential,

$$U(r) = z_i z_j \frac{e^2}{r_{ij}} + D_{ij}\left[\left\{1 - e^{-a_{ij}(r-r_0)}\right\}^2 - 1\right] + \frac{C_{ij}}{r_{ij}^{12}} \quad (62)$$

developed by Pedone et al (Pedone, Malavasi et al. 2006). The potential was implemented and used by the authors to calculate structural and mechanical properties of different metal oxides, but was not tested for conductivity predictions, such as for slags of the compositions targeted here. The first term of the potential describes long-range Coulombic electrostatics, the second term is the Morse-Stretch (MS) non-bonded potential, and the third term is a repulsive contribution to the potential. The third term is only necessary to model the interactions at high temperature and pressure (Pedone, Malavasi et al. 2006). Since the simulations were performed at atmospheric pressure, this term is not required and was therefore not used. For a MS potential alone, D_{ij} is the bond dissociation energy, a_{ij} is a function of the slope of the potential energy well, and r_0 is the equilibrium bond distance. When the Coulombic and repulsive terms are included, the correspondence to the Morse potential is lost and the quantities D_{ij} and a_{ij} are just parameters with limited or no physical meaning. Table 5 shows the potential parameters used to model the slag systems. The superscripts on the metal and oxygen atoms are partial charges used within this potential. The oxygen ion charges remain fixed at -1.2 and the metal ion charges were assigned based on these to ensure self-consistency, viz., q (Si) = -2q (O) and q (Mg) = q (Ca) = -q (O), q (Al) = -3/2q (O).

Table 5. Potential parameters for the Morse–type potential

Pair	D_{ij} (eV)	a_{ij} (Å^{-2})	r_0 (Å)
$Ca^{1.2}$–$O^{-1.2}$	0.030211	2.241334	2.923245
$Si^{2.4}$–$O^{-1.2}$	0.340554	2.006700	2.100000
$O^{-1.2}$–$O^{-1.2}$	0.042395	1.379316	3.618701
$Mg^{1.2}$–$O^{-1.2}$	0.038908	2.281000	2.586153
$Al^{1.8}$–$O^{-1.2}$	0.361581	1.900442	2.164818

The subscripts on the metal and oxygen atoms are the partial charges used for this potential.

The second force field used is a Buckingham potential, described below. The parameters used for the Buckingham potential are the ones suggested by Matsui (Matsui 1996) and are listed in Table 6.

$$U(r_{ij}) = \frac{z_i z_j}{r_{ij}} + B_{ij} e^{\frac{-r_{ij}}{\rho_{ij}}} - \frac{C_{ij}}{r_{ij}^6} \quad (63)$$

Here r_{ij} is the distance between atoms *i* and *j*, z_i is the effective charge associated with the atom *i*, and B_{ij}, ρ_{ij} and C_{ij} are energy parameters for the pair *ij* describing repulsive, Coulombic and dispersive forces, respectively. This potential form has three types of fitting costants, namely B, ρ, and C_{ij}, which were used by the authors to match the predictions of the potential functions to crystallographic data and elastic properties of the materials of interest. This potential model has been used by these authors to describe slag-like silicate systems, including electrical conductivity predictions. The Buckingham potential net charges q_i were constrained such that q (Ca) = q (Mg) = 2/ 3 q (Al) = 1/2 q (Si) = -q(0), in order to preserve the requirement of transferability between phases with different compositions.

Table 6. Potential parameters for the Buckingham potential

	z (e)	B (kJ/mol)	ρ (Å)	C (Å^6 kJ/mol)
O	-0.945	870570.0	0.265	8210.17
Si	1.89	4853815.5	0.161	4467.07
Al	1.4175	2753544.3	0.172	3336.26
Mg	0.945	15019679.1	0.178	4077.45
Ca	0.945	15019679.1	0.178	4077.45

Values of B, ρ and C correspond to cation–oxygen and oxygen–oxygen interactions only, while the cation–cation interactions are described by Coulombic repulsive forces alone.

The slag properties tested include densities, and the transport properties namely diffusion coefficients and electrical conductivities. The densities of three low silica CaO-SiO_2-Al_2O_3 ternary slags at a temperature of 1733K to evaluate how well the Buckingham and the Morse potential models predict the high temperature properties of slags, before calculating the transport properties. These slag systems were chosen because they have known experimental

values, sourced from (Muhmood and Seetharaman 2010), as shown in Table 7. The full computational details are in section 5.1.

The Morse type potential predicts the experimental densities with better accuracy than the Buckingham potential. The difference in accuracy is likely due to the difference in parametrisation technique. The Buckingham potential was parametrised by fitting the force field parameters to both the observed structural properties such as coordination numbers, lattice parameters and bulk moduli of 27 crystals in the individual oxides and multicomponent CMAS liquid system (Matsui 1996). On the other hand, the Morse type potential was parametrised to reproduce a much greater number of data points, including the experimental crystal structures (lattice parameters and atomic positions for one or more configurations) and/or crystal properties that contain information concerning the shape of the energy surface, such as elastic constants, high-frequency and static dielectric constants, lattice energy, piezoelectric constants, or phonon frequencies (Pedone, Malavasi et al. 2006). The simulation procedure is explained in section 5.1.1.

Table 7. Densities of slag calculated using Buckingham and Morse type potentials by MD simulation at a temperature of 1733 K. These slag systems were sourced from Muhmood and Seetharaman (Muhmood and Seetharaman 2010).

Slag systems in %w	Experimental (g/cm^3)	Simulation (g/cm^3)	
		Morse	Buckingham
51.5 CaO – 43.5 Al_2O_3 – 5.0 SiO_2	2.88 ± 0.07	2.91 ± 0.070	3.02 ± 0.0798
51.5 CaO – 38.9 Al_2O_3 – 9.6 SiO_2	2.79 ± 0.03	2.81 ± 0.103	3.05 ± 0.0525
51.5 CaO – 34.5 Al_2O_3 – 14 SiO_2	2.76 ± 0.03	2.82 ± 0.02	2.98 ± 0.048

An accurate prediction of density is not necessarily an indicator that other properties were also accurately modelled. Slag transport properties, i.e., diffusion coefficients and electrical conductivities, were therefore also calculated for the compositions measured by Hundermark (Hundermark 2003), to determine how well the two potential models perform with respect to experimental electrical conductivity. The two slag systems chosen are denoted I0 and H0 (relating to their basicity: I for "intermediate" and H for "high") and their MD simulated diffusion coefficients are shown in Table 8. From these results it can be seen that the diffusion coefficients obtained using the Buckingham potential are higher than those obtained using the Morse type potential model. The diffusion coefficients increase from I0 to H0 for all the ions

and for both models, which can be attributed to an increase in depolymerisation owing to an increasing basicity. These differences in dynamics are expected to have an impact on calculated electrical conductivities of the slag systems as well.

Table 8. Diffusion coefficients (10^{-9} m^2/s) of ions in different oxides calculated using Buckingham and Morse type potentials at 1821 K

Buckingham potential					
Slag	D(Al)	D (Ca)	D(Mg)	D(Si)	D(O)
I0	0.59 ± 0.15	1.5 ± 0.26	1.9 ± 0.31	0.37 ± 0.061	0.51 ± 0.085
H0	1.08 ±0.028	2.3 ±0.026	2.7 ±0.027	0.67±0.014	0.91 ±0.014
Morse type potential					
Slag	D(Al)	D (Ca)	D(Mg)	D(Si)	D(O)
I0	025 ± 0.058	0.66 ± 0.02	0.85 ± 0.014	0.14 ±0.037	0.210±0.041
H0	0.429±0.014	0.995±0.022	1.17 ±0.094	0.269±0.047	0.35±0.0029

The calculated electrical conductivities of the slag systems are shown in Table 9 and are compared to the experimental values. The collective transport properties such as electrical conductivity are affected by perturbation leading to higher deviations due to dynamic correlations in the system. This effect is reflected in the higher standard deviations in calculated exact electrical conductivity for the simulated slags. The higher standard deviations indicate that exact electrical conductivities are more prone to statistical error when estimated from molecular dynamics simulation and typically require longer and more careful analysis, i.e., the choice of fitting range.

Table 9. Experimental and MD simulated electrical conductivities (S/m) of slag systems calculated using the Buckingham and Morse type potentials. These slag systems were sourced from Hundermark (Hundermark 2003)

Slag system	Exact		Nernst–Einstein	
	Morse	Buckingham	Morse	Buckingham
I0 (exp 20.8)	35.0±11.0	38.0±15.0	42.2±0.89	69.6±0.93
H0 (exp 45.5)	49.3 ±9.3	54.5±14.0	68.6±1.6	104.0±0.88

Electrical conductivities calculated using the Morse potential are lower than those obtained using the Buckingham potential and are closer to the experimental values. The overestimation using the Buckingham potential can be attributed to higher dynamics observed in diffusion coefficients. Since the electrical conductivities are related to the diffusion coefficients, it can therefore be expected that the higher diffusion coefficients will be associated with higher electrical conductivities. At this point, it is not conclusive whether the Morse potential form is inherently better for simulating the properties of slag systems or whether a different set of self-consistent Buckingham potentials could be found that would give as good or better agreement. However, based on the ability of the Morse potential of Pedone (Pedone, Malavasi et al. 2006) to better predict the experimental densities and electrical conductivities of these representative slags, it was decided to use this potential without further refinement in all the simulations in this work.

It should also be mentioned that Xiang, Du et al. (Xiang, Du et al. 2013) reported that a Buckingham potential (using a different parameterization and slightly altered functional form than what was used here) predicted densities similar to the experimental values for sodium aluminosilicate glasses, while the Pedone Morse potential gave systematically higher (around 15%) densities than the experimental values. However, the structural properties generated using the Buckingham potential contained 3% to 10% of three–coordinated Al, which is considered to be coordination defects from simulations, while the Morse potential did not show any three–coordinated Al (Xiang, Du et al. 2013). Furthermore, Du and Xiang (Du, and Xiang. 2012) studied the effects of strontium substitution on the structure, ionic diffusion and dynamic properties of 45S5 bioactive glasses using a Buckingham potential and found that this potential underestimated the densities of the glasses. Both of these potentials can thus be used to study silicate melts, however they might need improvement in order to predict properties of some slags accurately

Lastly, the Buckingham potential is considered to be transferable in the current composition ranges as reported by Guillot and Sator (Guillot and Sator, 2007). The Morse type potential was also reported to be transferable based on the fact that it reproduced structural and mechanical properties of alumino–phosphates, although they were not explicitly considered during the parameterization process (Pedone, Malavasi et al. 2006).

5.3. Testing of MD simulation parameters

5.3.1. Relaxation times

To evaluate the influence of control variable relaxation time on the melt properties, several test runs were performed with 0.5, 1.0, 2.0 and 4.0 ps relaxation times for temperature control (using both the Berendsen and Nose-Hoover thermostats to give NPT and NVT ensembles, respectively) and 0.5, 1.0, 3.0 and 6.0 ps relaxation times for pressure control (using the Berendsen barostat). The systems were simulated for a total of 1 ps and a 1 fs time step at a target temperature of 1823 K and a target pressure of 1.0 atm. For temperature relaxation times in the NPT ensemble (with the barostat relaxation set to 3.0 ps), the average temperatures and densities were calculated. The average temperature with a 1.0 ps relaxation time was closest to the expected value of 1823 K, as shown in Table 10. With the shortest relaxation time the temperature fluctuated below the target, whereas drift was observed to a higher than expected temperature when longer relaxation times were used. Although not influenced directly by the relaxation times, the densities are reported and were found to be 2.64 g/cm^3, throughout. These results therefore show that a relaxation time of 1.0 ps is appropriate.

Table 10. Average temperatures and densities for different values of the temperature relaxation time, set to a target of 1823 K, in the Berendsen isothermal–isobaric ensemble

	Time constant in ps			
	0.5	1.0	2.0	4.0
Temp (K)	1784.7± 0.36	1821.2 ± 0.28	1838.9 ± 0.025	1862 ± 0.12
Density(g/cm^3)	2.64	2.64	2.64	2.64

The pressure relaxation time constants resulted in a very small difference in densities with the exception of 0.5 ps relaxation time, which gave a density of 0.03 g/cm^3, as shown in Table 11. The 3.0 ps relaxation time is therefore appropriate for pressure control.

Table 11. Average densities for different values of the pressure relaxation time, set to a target of 1 atm, in the Berendsen isothermal–isobaric ensemble

	Time constant in ps			
Time constant	0.5	1.0	3.0	6.0
Density(g/cm^3)	0.03	2.64	2.62	2.65

The Nose-Hoover canonical (NVT) ensemble relaxation times were also tested to determine appropriate relaxation times for the production phase of the simulations. Results are shown in Table 12. An average temperature closest to the target temperature is achieved at 2.0 ps, which was the relaxation time used in all NVT studies in this study. Furthermore, it is interesting to note that the temperature for this relaxation time starts to stabilise after about 500 time steps, as shown in Figure 12. The other relaxation times had a similar behaviour but stabilised after a larger number of steps.

Table 12. Thermodynamic properties of slag system N6 at different relaxation times

	Time constant in ps			
Time constant	0.5	1	2	4
Temp (K)(NVT)	1777.5± 0.11	1801.2 ± 0.16	1832.8 ± 0.27	1846 ± 0.02

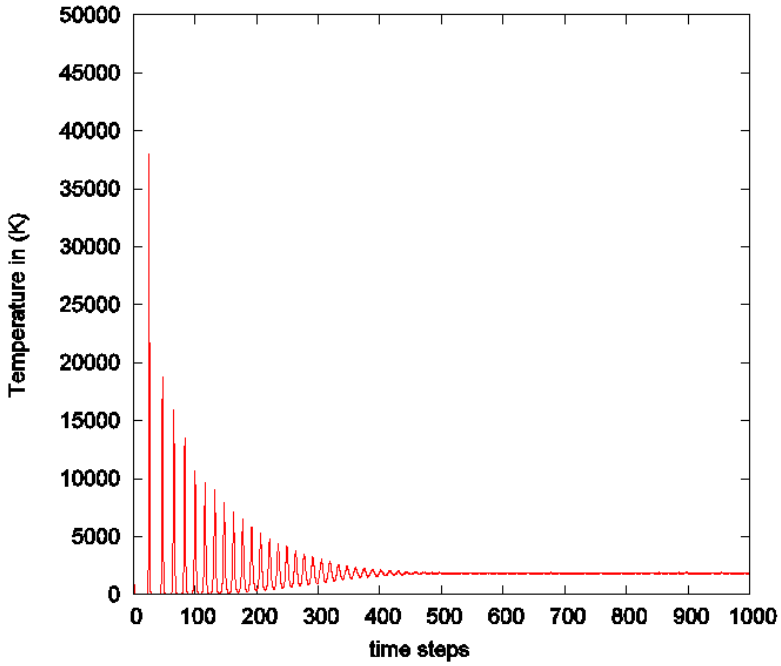

Figure 12: Times steps vs temperature for 2ps canonical (NVT) ensemble relaxation time.

5.3.2. Equilibration length

Since simulations in this work were started from a random disordered configuration at a different temperature and density, it was necessary to run the simulation for a period so that the system can come to equilibrium at the new state point. At the end of this period, all memory of the initial configuration should have been lost. To monitor thermodynamic equilibration of the system, instantaneous record values of the system energy, densities and M–O PDFs were recorded during this period. The equilibration period is carried out at least until these quantities have ceased to show a systematic drift and have started to oscillate about steady mean values. The choice of 1000 ps as equilibration time was tested by calculating the evolving density, the change in diffusion coefficients as well as the change in local structure. The latter was done by computing the M–O PDFs in 250 ps intervals Beyond 250 ps the RDF give similar (nearly exact) results as can be observed in Figures 15 - 18. The diffusion coefficients also stabilises between 250 and 500ps.

The diffusion coefficients beyond 250ps shown no significant difference as shown in Table 13. The system energy stabilised at approximately 250ps, the same applies to densities as shown in Figures 13 and 14 respectively.

Table 13. Diffusion coefficients in 10^{-9} m^2/s

Time (ps)	D_{Mg}	D_{Ca}	D_{Si}	D_{Al}	D_O
0–250	2.59	3.12	1.80	1.61	1.97
250–500	0.88	0.70	0.17	0.29	0.20
500–750	0.81	0.72	0.17	0.24	0.22
750–1000	0.98	0.70	0.17	0.21	0.22
6000–11000	ND	ND	ND	ND	ND

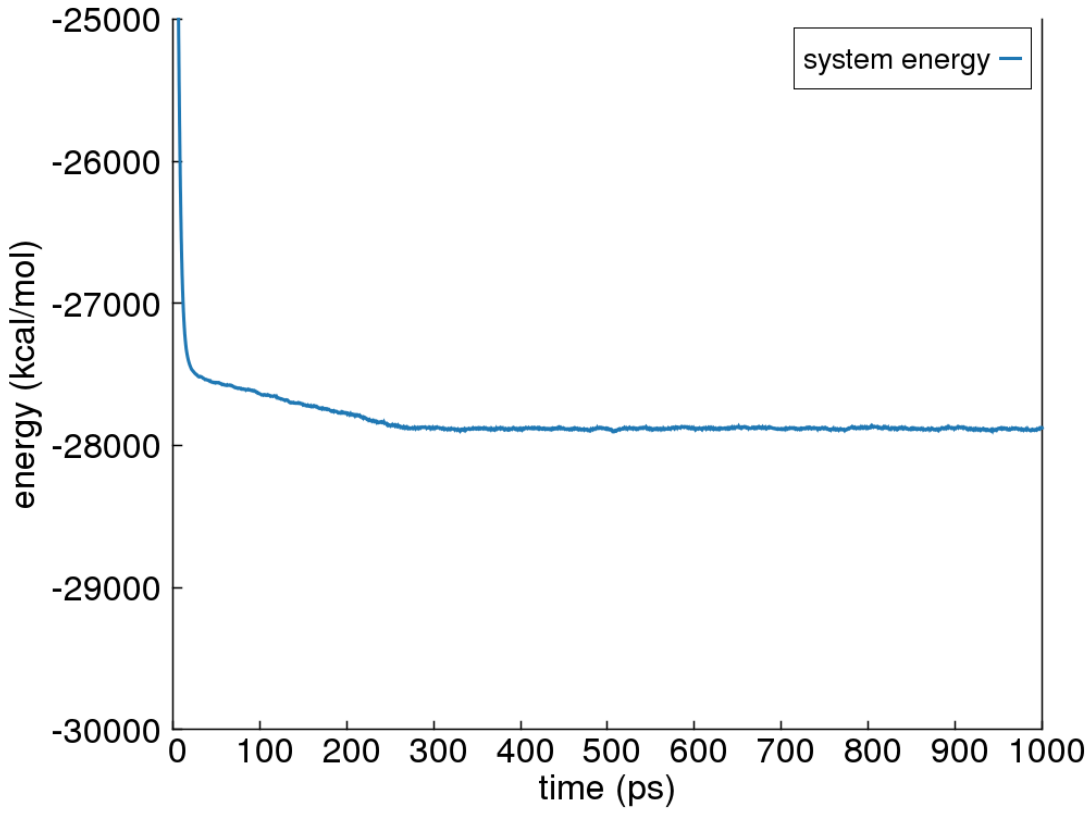

Figure 13. The change in system energy, plotted against simulation time.

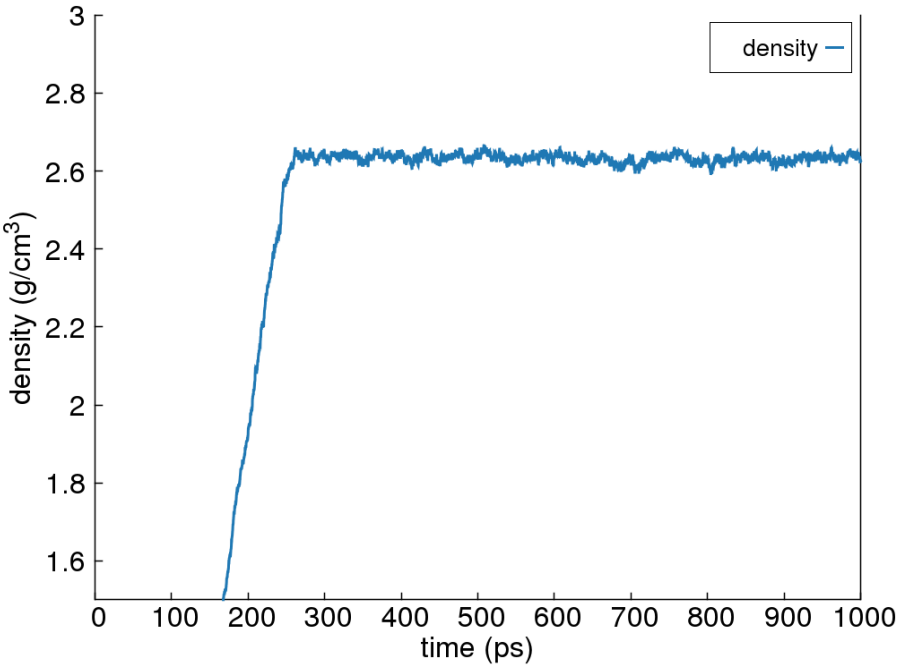

Figure 14: The change in density, plotted against simulation time.

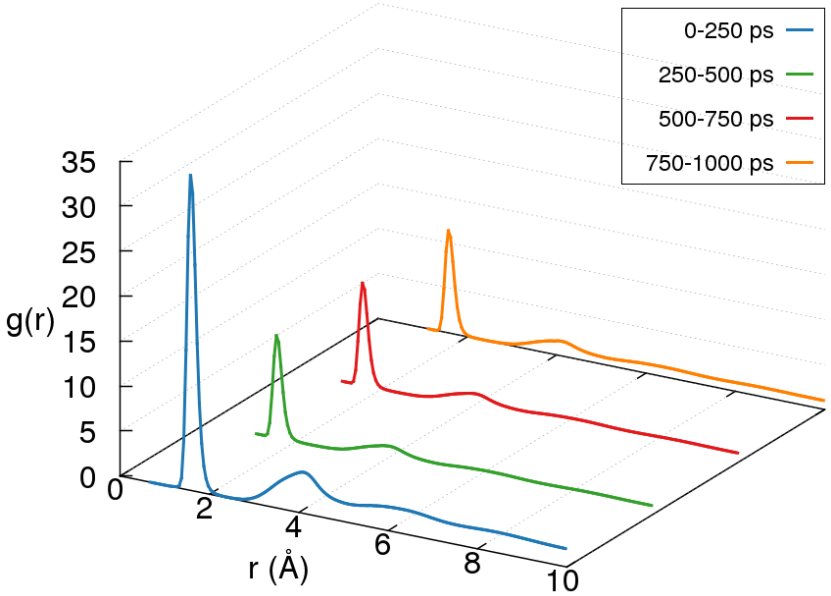

Figure 15. The change in RDF, plotted against simulation time for Si-O

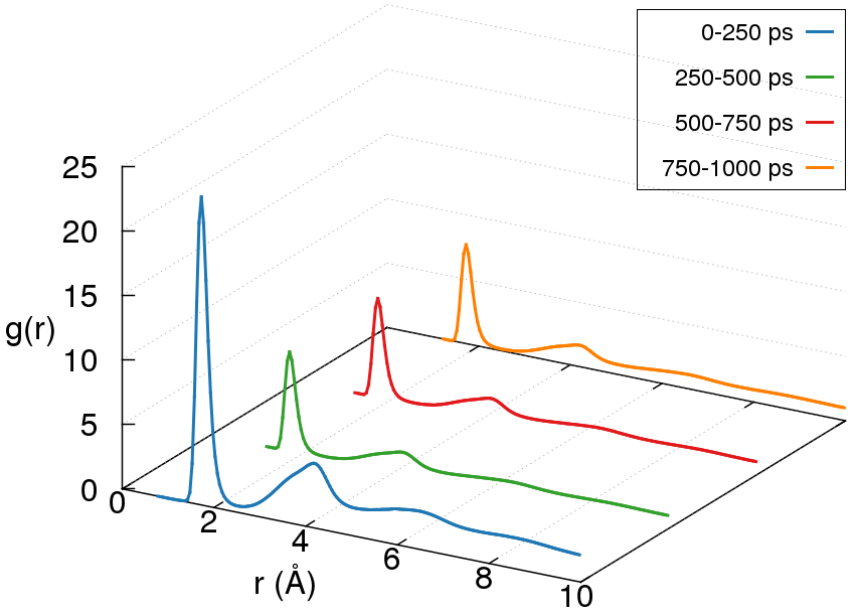

Figure 16. The change in RDF, plotted against simulation time for Al-O

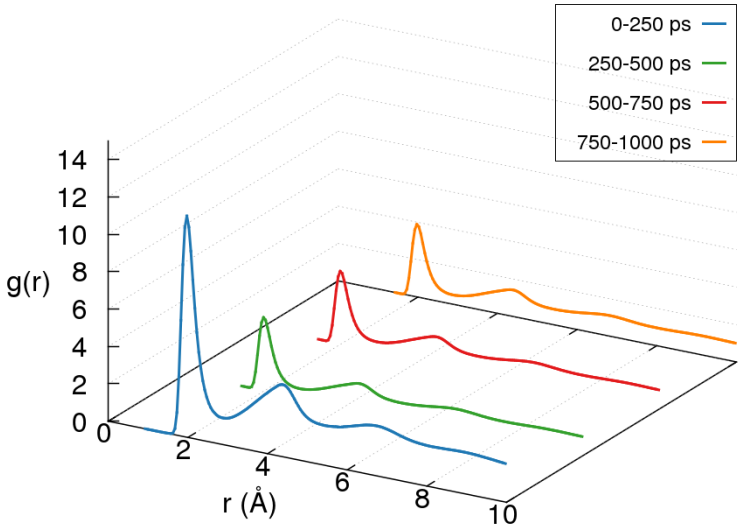

Figure 17. The change in RDF, plotted against simulation time for Mg-O

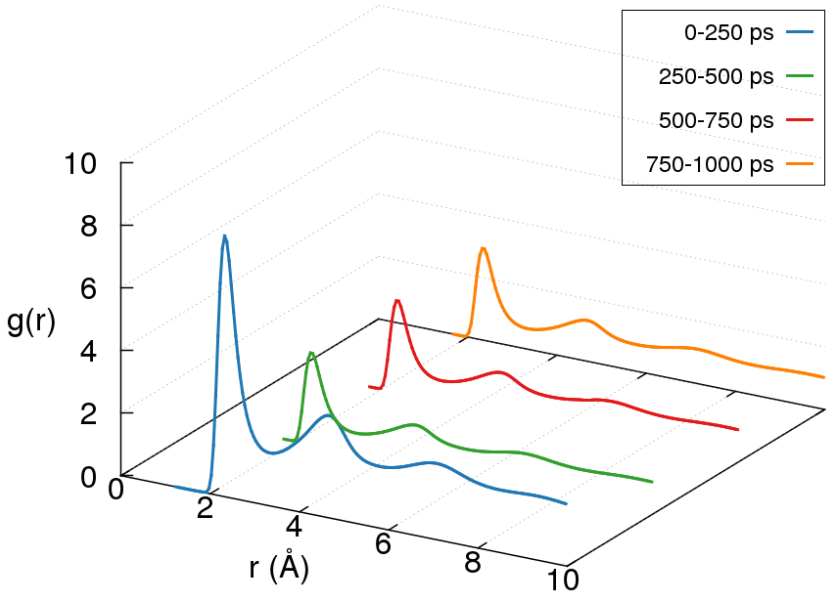

Figure 18. The change in RDF, plotted against simulation time for Ca-O

5.3.3. System size

To evaluate the influence of the system size on the melt properties, several test runs were performed with systems sizes of 1530, 2144, 3051 and 6033 atoms. The densities for 1530, 2144, 3051 system sizes were 2.65g/cm^3 and for 6033 atoms was 2.64g/cm^3 . The diffusion coefficients for the same system sizes were also compared. No significant system size effect was detected for both the densities and diffusion coefficients as can be observed in Table 14. For a good compromise between accuracy and computational cost, I choose a system size of 2000 to 3000 atoms depending on composition and density of the system. The simulation procedure is explained in section 5.1.1.

Table 14. Diffusion coefficients and densities of the N6 slag system at different box sizes

Temp (K)	D_{Mg}	D_{Ca}	D_{Si}	D_{Al}	D_{O}	Density (g/cm^3)
1531	0.85 ± 0.12	0.71 ± 0.10	0.17 ± 0.01	0.27 ± 0.06	0.22 ± 0.01	2.65 ± 0.07
2144	0.74 ± 0.20	0.86 ± 0.09	0.28 ± 0.03	0.19 ± 0.03	0.23 ± 0.01	2.65 ± 0.01
3051	0.84 ± 0.11	0.75 ± 0.06	0.17 ± 0.01	0.28 ± 0.05	0.23 ± 0.01	2.65 ± 0.07
6033	0.90 ± 0.04	0.74 ± 0.03	0.19 ± 0.01	0.25 ± 0.02	0.24 ± 0.01	2.64 ± 0.01

To further check whether the simulations were performed correctly, the densities for all the 9 systems were calculated and compared with densities calculated using a predictive model by Yuan et al. (Mills, Yuan et al. 2011). The calculated densities are shown in Table 15. The MD calculated densities ranges between 2.63 and 2.66 g/cm^3 while the theoretical calculated densities are 2.7 g/cm^3 on average. The MD calculated densities compares well with theoretical densities. These values also fall in the same ball park as the densities of CaO-MgO-Al_2O_3-SiO_2 which also range between 2.42 and 2.67 g/cm^3 at approximately similar temperature by Courtial and Dingwell (Courtial and Dingwell 1999).

Table 15. Densities of simulated slag systems

Slag system	Theoretical density (g/cm^3)	MD calculated density(g/cm^3)
N1	2.64	2.65 ± 0.0
N2	2.66	2.64 ± 0.0
N3	2.66	2.63 ± 0.0
N4	2.67	2.63 ± 0.0
N5	2.69	2.66 ± 0.0
N6	2.68	2.64 ± 0.0
N7	2.70	2.66 ± 0.0
N8	2.70	2.64 ± 0.0
N9	2.71	2.65 ± 0.0

5.4. Effect of cut off distance on structural properties

The sensitivity of structural properties as a function of varying cut off distances was investigated in this work. Three different cut off distances which correspond to the location of the first minimum in the partial pair correlation function of the X–O correlation curve were used to determine a suitable cut off distance for structural property analysis. The cut off distance is different from the bond length or bond distance which is the average distance between nuclei of two bonded atoms in a molecule and is taken as the first maxima of the pair distribution function. The cut off distances proposed as the first minimum in the PDF were 2.325, 2.525, 2.875 and 3.325 Å for Si-O, Al-O, Mg-O and Ca-O, respectively and were chosen as they appear in the PDF curves. The above cut off distances were then varied by -5% and +5%

and the results compared. The change in oxygen bridging types as a function of cut off distance was tested on two different slag systems, viz. N7 and N8. Table 16 indicates that the cut off distances do not significantly change the proportion of bridge types. A closer look at a PDF curve (Figure 19) shows that the Si-O minima are flat and range from approximately 2.1 to 2.8 Å. This might be the reason why the bridging types do not change significantly.

Table 16. Changes in numbers of oxygen bridging types as a function of cut off distance (Å)

Slag	Si-O-Si	Si-O-Al	Si-O-Si	Si-O-Al	Si-O-Si	Si-O-Al
	Original cut off (2.325)		-5% (2.209)		+5% (2.441)	
N7	59	40	59	41	61	39
N8	60	40	59	41	61	39

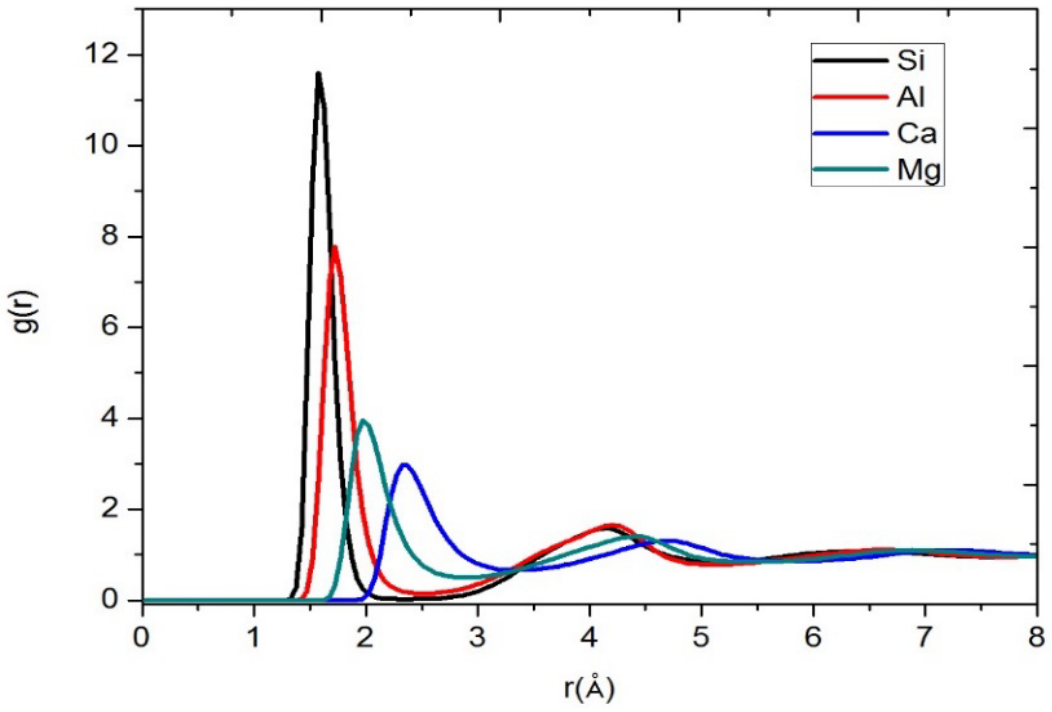

Figure 19. The ion–oxygen pair distribution function curves (PDF) showing the first peaks and the minima following the peaks, representing the bond length and cut off distances, respectively, of the cation–oxygen nearest neighbour for Si–O, Al–O, Mg–O and Ca–O in the N8 system.

It was further tested the effect of the cut off distances on the coordination numbers using same values as above (Table 17). The coordination numbers were calculated integrating the area under the PDF curve, i.e., the running integral.

Table 17. Changes in coordination number as a function of changes in cut off distances

	N7			N8		
Cut off	2.325 Å	2.209 Å (−5%)	2.441 Å (+5%)	2.325 Å	2.2089 Å (−5%)	2.441 Å (+5%)
Si	4.00	3.99	4.00	4.00	3.99	4.00
Al	4.12	4.06	4.18	4.12	4.06	4.18
Ca	6.36	5.81	6.95	6.39	5.84	6.99
Mg	4.58	4.30	4.87	4.59	4.31	4.89

The average coordination numbers for network formers remain similar, for Si the value is 4.0 and for Al the value ranges between 4.0 and 4.2, as can be seen in Table 17. These are consistent with those observed by Vuilleumier and Sator (Vuilleumier, Sator et al. 2009) in similar slag systems and are the expected coordination numbers for network formers. For network breakers, the average coordination numbers range between 5.8 and 7 for Ca, and 4.3 and 5 for Mg. These also fall within the expected band of coordination numbers for network breakers (Vuilleumier, Sator et al. 2009). The cut off distance does, however, give a greater variation in the coordination numbers for network breakers; this can be expected, since these cations are the most mobile in the melt, lacking a rigid, uniform local environment. Also, on closer inspection of the PDF curves, the network modifier PDF minima are less flat than those of the network formers. This can contribute to the observed variation in coordination numbers of network breakers. Changing the cut off distance was therefore affect these species more than the network formers, leading to significant variations in coordination numbers in the local environment. It should be noted that the cut off distance then becomes the choice of the author, as long as it gives reasonable results compared to experiment and can be argued to be suitable based on the physical form of the PDF. In this work, the cut off distances settled on for in all the calculations were the first minima in the respective PDFs at 2.325, 2.525, 2.875 and 3.325 Å

for Si-O, Al-O, Mg-O and Ca-O, respectively. For Si-O and Al-O, a minor change had a negligible effect and for Mg-O and Ca-O, the changes were within the band of values reported by others.

This then concludes the section wherein the choice of potential and cut offs were tested. In the remainder of the chapter, the results for a systematic study of the nine slag systems given in Table 4 are reported. Results are discussed in detail and relationships between simulated properties and empirically predicted quantities, are elaborated on.

5.5. Structural properties of simulated slags

This section presents the results of the structural and transport properties of nine (9) successfully simulated slag systems, i.e., N1 – N9. These properties of the slag melts are discussed in detail, while the relationship between transport properties of the melt, and structural properties are also investigated. The simulation procedure was explained in section

5.5.1. Bond lengths

The PDF gives insight into the local structure of an atomic system; that is, it shows the radially averaged manner in which atoms organise themselves around one another. These functions can be evaluated and compared with those observed from X-ray and neutron diffraction experiments. The description of the short–range ordering of the silicate melt structure of slags proceeds from the analysis of PDFs. Figure 19 shows the PDF of Si–O, Al–O, Mg–O and Ca–O for slag system N1. The first peak and the minimum following this peak represent the bond length and cut off values respectively of the cation-oxygen nearest neighbour pairs. The bond length is defined as the mode of the first peak in the PDF (de Koker, Stixrude et al. 2008). Two atoms (e.g., Si and O) are considered bonded if their separation is less than the distance representing the first minimum in the corresponding PDF. The PDFs are output at particular intervals (bin sizes), which was 0.05 Å. Therefore although there might be variations of maybe 0.05 Å between values, they all appear the same. The first peak of the PDF is located at 1.60 Å for Si-O, 1.80 Å for Al-O, 2.00 Å for Mg-O and 2.40 Å for Ca-O. The sharpness of the peaks indicates highly ordered slag structures. The Si–O and Al-O peaks are significantly narrower than the other peaks, with the former narrower than the latter, denoting a more rigid Si–O than Al–O coordination shell. The Si-O, Al-O, Mg-O and Ca-O peak positions are the same in all the slag systems. There was no significant change observed with varying chemical compositions, except for a decrease in peak intensity with a decreasing basicity, thus implying

a constant bond length between cations and oxygens. The cation–oxygen bond lengths are directly comparable to the experimental data available in the literature for analogous systems, as shown in Table 18. I note that the nearest-neighbour distances are consistent with experimental values observed by Waseda and Toguri, Waseda and Suito, Anderson and Guignard and Cormier (Waseda and Toguri 1990; Waseda and Suito 1977; Waseda and Toguri 1977; Waseda and Toguri 1978; Don L. Anderson 1989, Guignard and Cormier 2008) in binary silicate melts and glasses.

Table 18. The bond lengths (Å) of the metal oxides (PDF peak, "Max") and the minimum after the first peak (PDF peak "Min") used to calculate the coordination numbers of oxygen atoms around the metal cations

	Si-O		Al-O		Mg-O		Ca-O	
	Max	Min	Max	Min	Max	Min	Max	Min
N1	1.60	2.10	1.80	2.50	2.00	2.90	2.40	3.40
N2	1.60	2.20	1.80	2.50	2.00	3.00	2.40	3.50
N3	1.60	2.20	1.80	2.50	2.00	3.00	2.40	3.50
N4	1.60	2.20	1.80	2.50	2.00	3.00	2.40	3.50
N5	1.60	2.20	1.80	2.50	2.00	3.00	2.40	3.50
N6	1.60	2.20	1.80	2.50	2.00	3.00	2.40	3.50
N7	1.60	2.20	1.80	2.50	2.00	3.00	2.40	3.50
N8	1.60	2.20	1.80	2.50	2.00	3.00	2.40	3.50
N9	1.60	2.20	1.80	2.50	2.00	3.00	2.40	3.50

5.5.2. Oxygen bridging types

The melt framework can be investigated by quantifying the extent to which $[SiO_4]^{4-}$ and $[AlO_4]^{5-}$ tetrahedral species are connected. This provides information of the polymerisation in the melt, which relates to the mass and charge transport, influencing macroscopic properties

such as viscosity and conductivity. Greater polymerisation decrease conductivity and increase viscosity (and *vice versa*). The distribution of oxygen atoms into bridging oxygen (BO), nonbridging oxygen (NBO) and three–bonded oxygen atoms (TBO) or triclusters, was therefore calculated. The remaining oxygen atoms are considered unclassified or "free". An oxygen atom is assumed to be a BO when it is connected to two network formers (either Si or Al, provided that the metal atom is bonded to the four nearest neighbouring oxygen atoms,(Cormack and Cao 1996) (denoted as $^{[4]}$Al or $^{[4]}$Si), whereas it is an NBO when it is connected to only one network forming Si or Al atom. TBOs are oxygens that are bonded to three network formers, the latter being defined as above. In addition, disorder in the framework can be further characterised through the degree of mixing of interconnected $[SiO_4]^{4-}$ and $[AlO_4]^{5-}$ anions. The BOs were therefore identified as being either $^{[4]}$Si–O–$^{[4]}$Si, $^{[4]}$Si–O–$^{[4]}$Al or $^{[4]}$Al–O–$^{[4]}$Al bridges.

The distribution of BOs and NBOs is presented in Figure 20. NBOs should dominate, since all the compositions are in peralkaline region. In the simulations, NBOs are observed to outweigh the BOs by up to a factor of four. As the basicity increases, the values range from 60% (N1) to 73% (N9) for NBOs, and from 37% to 18% for BOs. In addition, there are high numbers of "free oxygens", with as many as 9% for N9. Since I did not perform an explicit check, but assumed free oxygens to be those not identified as BO, NBO or TBO, this classification could be (or is clearly) the result of one of two possibilities. These possibilities are either that an oxygen atom is unbound with no Si^{4+} or Al^{3+} coordinating partners within the PDF cut off (due to coordination to Mg^{2+} and Ca^{2+} cations only) or, most likely, due to coordination with Si^{4+} and Al^{3+} cations that are not in a tetrahedral configuration.

The fraction of NBOs can also be calculated directly from the composition expressed in mole fractions, (Mysen, Virgo et al. 1984, Mills 1993)

$$f(\mathrm{NBO}) = \frac{2\left(x_{\mathrm{MgO}} + x_{\mathrm{CaO}} - x_{\mathrm{Al_2O_3}}\right)}{x_{\mathrm{MgO}} + x_{\mathrm{CaO}} + 2x_{\mathrm{SiO_2}} + 3x_{\mathrm{Al_2O_3}}} \tag{64}$$

Equation 64 assumes that all Si^{4+} and Al^{3+} cations are network forming, with the $[AlO_4]^{5-}$ always charge balanced by either Ca^{2+} or Mg^{2+} cations. It is worth noting some factors that could lead to the MD calculated values differing from predictions obtained using this equation. Firstly, the formation of $[AlO_n]^{3-2n}$ species with higher/lower coordination than four (see section 5.3.4) means that not all Al^{3+} can be strictly classified as network forming. Also, the association of a single charge balancing cation with two $[AlO_4]^{5-}$ is not necessarily true in the

dynamic environment, especially at low Al_2O_3 concentration. As a result, it was found that MD simulation consistently gives a lower number of NBOs than does the composition–based estimate.

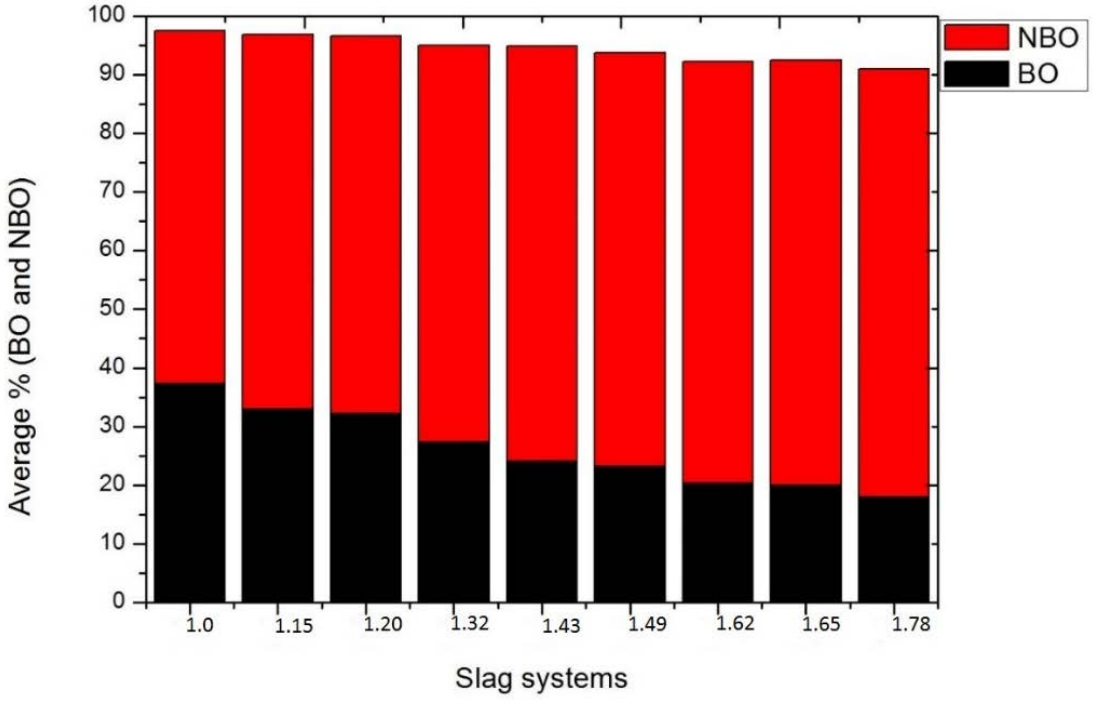

Figure 20. Bridging (BO) and nonbridging oxygen atoms (NBO) as a percentage of total oxygen atoms, averaged over each simulation. Slags systems are given using basicity.

The comparison of MD and the theoretically calculated NBOs are shown in Figure 21. The results are comparable at low basicity, but deviate increasingly as the basicity increases. Despite this, the two determinations still show a fairly good correlation with a correlation coefficient of 0.96.

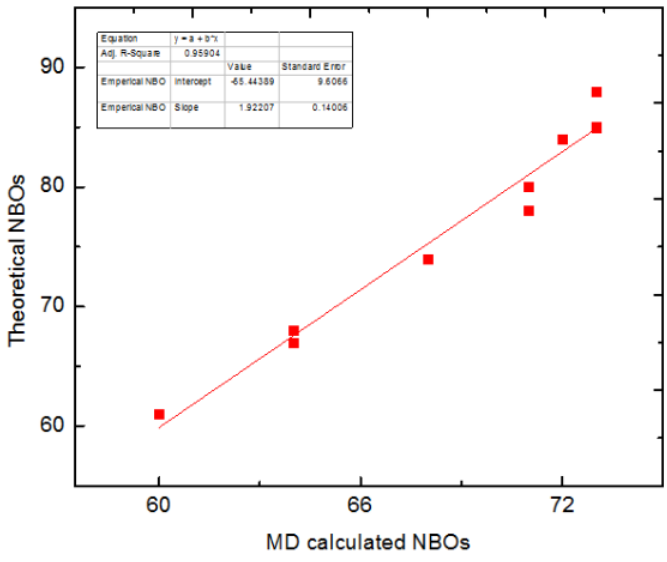

Figure 21. The relationship between the MD calculated and theoretically calculated NBOs.

Furthermore, the ratio of NBO/BO was compared to slag basicity (Figure 22). A linear fit gives a correlation coefficient of 0.99. This strong correlation indicates that as the basicity increases, so does the depolymerisation of the slag systems. It also shows that it might be possible to estimate the NBO/BO ratio directly from the value of the basicity.

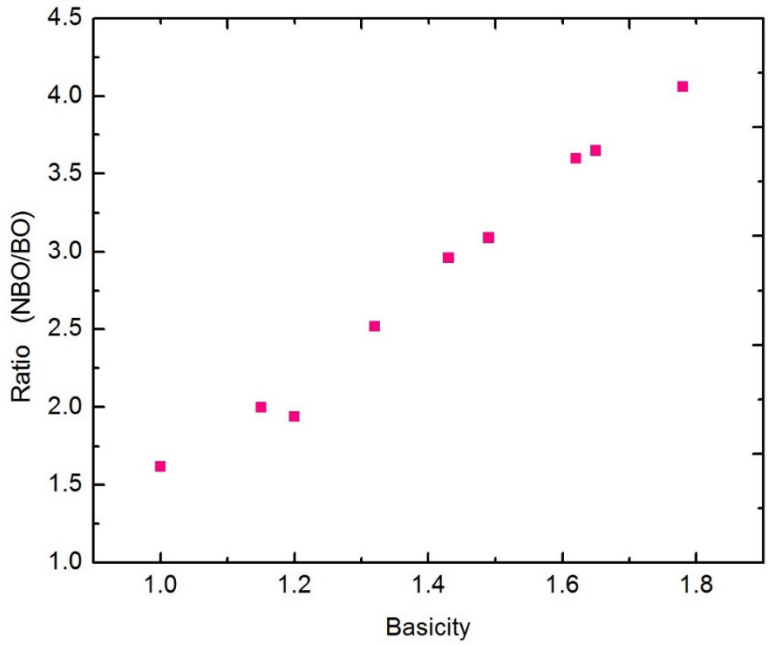

Figure 22. Ratio of bridging (BO) and nonbridging oxygen atoms (NBO) as a function of basicity.

5.5.3. Aluminium avoidance principle

Figure 23 shows the distribution of $^{[4]}$Si–O–$^{[4]}$Si and $^{[4]}$Si–O–$^{[4]}$Al bridges, while the distribution of $^{[4]}$Al–O–$^{[4]}$Al bridges was less than 1% and are not shown. In these silica rich compositions, $^{[4]}$Si–O–$^{[4]}$Si bridges are dominant and account for 56% (N9) to 74% (N1) of the total bridges. In general, a higher ratio of SiO_2/Al_2O_3 results in a greater number of $^{[4]}$Si–O–$^{[4]}$Si bridges.

The Al avoidance principle is an empirical rule stating that Al tetrahedra are not regularly found linked by common oxygen ions, especially at low Al content (Lowenstein 1954). Deviations from this rule are, however, known to occur, in particular when cations of high field strength, such as Ca^{2+} and Mg^{2+} are present, as is the case here (Stebbins, Lee et al. 1999, Stebbins, Kroeker et al. 2000). These ions would be more efficient in stabilising the higher negative charge associated with formation of an $^{[4]}$Al–O–$^{[4]}$Al linkage. In addition, a lack of these

bridges also relates to the preference for Al and Si bridging partners in a $^{[4]}$Si–O–$^{[4]}$X bridge, indicated by the following equilibrium shifting to the heterogeneous bonding partners on the right on adherence of Al avoidance,

$$Al–O–Al + Si–O–Si \rightleftharpoons 2\ Si–O–Al \quad (65)$$

With respect to the preference for Al/Si bridging partners in a Si–O–X bridge, early calorimetric data indicates no strong preference, while conclusions from *ab initio* calculations depend heavily on the environment and the presence of charge balancing cations (Navrotsky, Peraudeau et al. 1982, Navrotsky, Geisinger et al. 1985). At first glance, simulation results show no preference for either type of partner and that the Si–O–Si/Si–O–Al ratio increases steadily as the Si/Al ratio increases, as shown in Figure 24, with a correlation coefficient of 0.98. However, to further assess the degree to which this principle is either adhered to or not, the simulated results were compared with those obtained assuming a random distribution. A complete description of the applied random distribution model can be found in Pedone et al (Pedone, Gambuzzi et al. 2012). The results are shown in Table 19.

Due to the low concentration of Al, a random distribution shows the occurrence of $^{[4]}$Al–O–$^{[4]}$Al to be 2% or less. Importantly though, MD simulation predicts even lower amounts, the first indication of Al avoidance. In addition, as the SiO_2/Al_2O_3 ratio drops, which also corresponds to an increasing basicity in the compositions studied, the random distribution gives an increasing number of $^{[4]}$Al–O–$^{[4]}$Al bridges, whereas simulation results remain relatively constant throughout, suggesting a greater degree of Al avoidance at high basicity from the simulations. Another indication of this principle as observed from simulation is the lower number of predicted $^{[4]}$Si–O–$^{[4]}$Si bridges and the greater number of predicted $^{[4]}$Si–O–$^{[4]}$Al bridges, compared with a random distribution. This illustrates that equation 65 is predicted to be shifted to the right. Again, the difference becomes more pronounced as the basicity increases. One thus find consistent evidence indicating a preference for $^{[4]}$Si–O–$^{[4]}$Al bridges, and can therefore conclude that the compositions studied simulations do indicate a degree of Al avoidance, especially at higher basicity.

Finally, the percentage of TBOs is less than 0.08%, equating to 1.6 atoms in a simulation box of 2000 atoms. One of the reasons suggested for the formation of TBOs is to promote charge balancing of Al^{3+} cations, (Lacy 1963). However, with the small amount of Al_2O_3 present here and the excess availability of charge balancing cations, this mechanism is not expected to be significant.

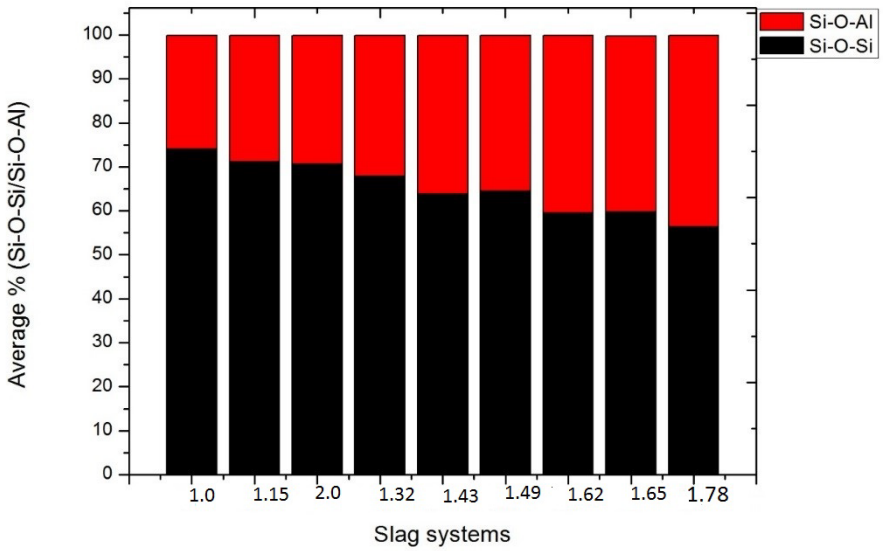

Figure 23. The percentage of $^{[4]}$Si–O–$^{[4]}$Si and $^{[4]}$Si–O–$^{[4]}$Al bridges in each composition. The slags systems are given in terms of basicity.

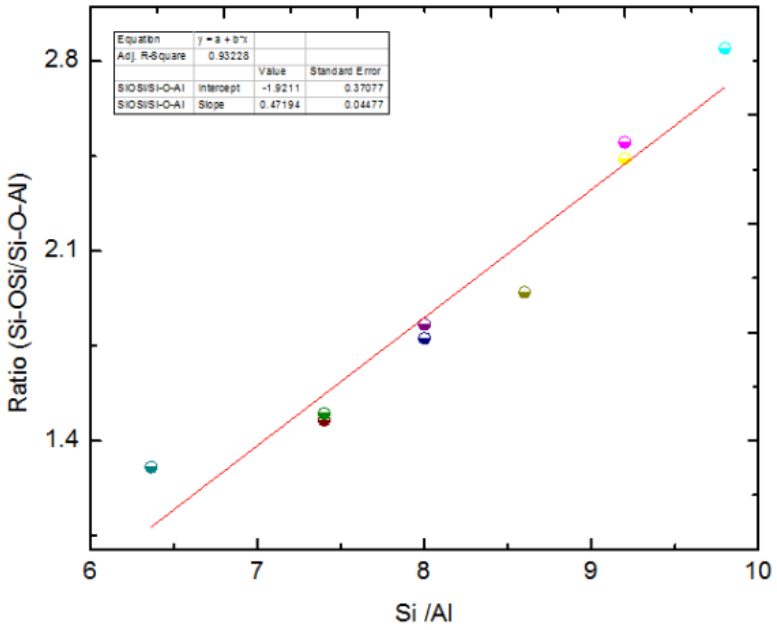

Figure 24. The ratio of Si-O-Si/Al-O-Si bridges as a function of Si/Al mol % of silicate slags N1 to N9.

Table 19. BO populations predicted by MD and assuming a random distribution†

	$^{[4]}$Si–O–$^{[4]}$Si		$^{[4]}$Si–O–$^{[4]}$Al		$^{[4]}$Al–O–$^{[4]}$Al	
Slag System	MD	Random	MD	Random	MD	Random
N1	74	80	26	19	< 0.5	1
N2	71	78	29	20	< 0.5	1
N3	71	78	29	20	< 0.5	1
N4	60	77	39	21	1	1
N5	64	76	36	23	< 0.5	2
N6	64	76	35	23	1	2
N7	59	74	40	24	1	2
N8	60	74	40	24	< 0.5	2
N9	56	72	43	24	1	2

† Calculated using $a_{M–O–M'} \times \chi_M \times \chi_{M'}$, where M or M′ refers to the metal, $a_{M–O–M}$ is the binomial coefficient and χ_M the mole fraction of metal M (Pedone, Gambuzzi et al. 2012).

5.5.4. Coordination number distributions

Oxygen coordination number (CN) distributions for each type of metal ion, as well as the corresponding standard deviations, were explicitly calculated (average coordination numbers can also be calculated by integrating under the first peak in the corresponding PDF, e.g., see Table 8 for comparison) and are shown in Figure 25 and the average CNs are shown in Table 20. The analysis was done for each composition, but varied very little and for brevity, only averages are discussed. The CNs are 4.0 for Si^{4+}, 4.0 for Al^{3+}, and range between 4.5–4.8 for Mg^{2+} and 6.3–7.1 for Ca^{2+}. The lowest standard deviation occurs for the Si^{4+} cation and the greatest for the Ca^{2+} cation. These are expected consequences of the persistence of the structure making tetrahedral $^{[4]}$Si units, and the mobility and greater size of the Ca^{2+} cation. The average of 4.1 for Al^{3+} is indicative of the presence of ≈10% $^{[5]}$Al, an observation that was discussed later.

Considering the distributions, the dominant CNs for the Mg^{2+} cation are 4 and 5, around 39% and 42%, respectively, in line with experimental estimates from X–ray and neutron diffraction data (Guignard and Cormier 2008) of MAS systems. There is also a significant amount (10–13%) of $^{[6]}$Mg, and somewhat less $^{[3]}$Mg (4.7–6.2%). The coordination of Ca^{2+} ions in the melts is characterised by a broad distribution, with values ranging from 4 to 9. The most abundant CNs for the Ca^{2+} cation are 6 and 7, contributing 34% and 32%, respectively. Again, this agrees well with experimental determinations in CAS systems (Neuville, Cormier et al. 2004). There

is also a significant amount of $^{[5]}$Ca (15%) and $^{[8]}$Ca (13%), with coordination by 4 (3%) and 9 (5%) oxygen atoms contributing the least. This wide distribution is consistent with Ca^{2+} having a larger effective ionic radius accommodating a greater variety of coordinations, compared with other cations present in the slag systems. Further, these coordination numbers are in good agreement with the classical molecular dynamics simulation studies of CMAS systems reported by Shimoda (Shimoda and Saito 2007) and Matsui (Matsui 1996) , both of which use intermolecular potentials that differ from the one used here.

With Al^{3+} as a structure forming ion inserted into the tetrahedral framework with Si^{4+}, a dominant CN of four is expected, which is indeed the case here, where 84.5-87% of this cation is present as $^{[4]}$Al. A large percentage (11–13%) of five coordinated $[AlO_5]^{5-}$species is, however, also present. Whereas in the peraluminous region these species are expected, a stoichiometric argument would suggest that in the presence of an excess of charge balancing Ca^{2+} and Mg^{2+} cations deep in the peralkali region, most Al^{3+} cations should be fully incorporated into the framework as $^{[4]}$Al, leaving little or no Al in six- and five-fold coordination. This is, however, not the case and it has been known for some time, as determined from NMR measurements, that $^{[5]}$Al species exist in aluminosilicates containing Ca and/or Mg at tectosilicate (i.e., $[x(CaO) + x(MgO)]/x(Al_2O_3) = 1$) or, surprisingly, even peralkaline compositions (Stebbins, Kroeker et al. 2000, Toplis, Kohn et al. 2000, Neuville, Cormier et al. 2004, Neuville, Cormier et al. 2006, Neuville, Cormier et al. 2007). Finally, the simulation results also show the presence of Al^{3+} coordinated to three and six oxygen atoms, although these are well below 2% of the total number of Al^{3+} cations.

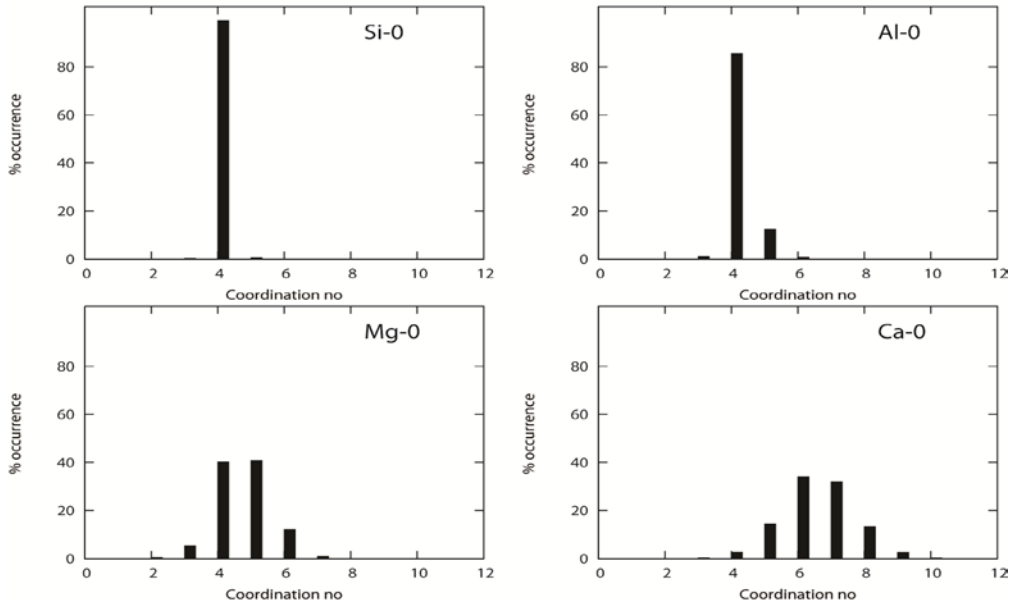

Figure 25. Coordination numbers for the simulated silicate slags (N1 to N9). The histograms were calculated as averages over all nine compositions.

The great stability of the tetrahedral $[SiO_4]^{4-}$ species leads to a dominant coordination number of 4 for Si (>99%) in all compositions, although a very small amount of $^{[5]}$Si (< 1%) is present as well. This is not unexpected, as $^{[5]}$Si is known to occur at low atmospheric pressure (Stebbins 1991), albeit at very low concentrations.

Table 20. Average coordination numbers for each atom in the silicate slags N1 to N9

	N1	N2	N3	N4	N5	N6	N7	N8	N9
Si	4.0	4.0	4.0	4.0	4.0	4.0	4.0	4.0	4.0
Al	4.1	4.1	4.1	4.1	4.1	4.1	4.1	4.1	4.1
Mg	4.7	4.7	4.7	4.6	4.6	4.6	4.6	4.6	4.5
Ca	6.6	6.5	6.5	6.4	6.4	6.4	6.4	6.4	6.3

5.5.5. Bond angle distribution (BAD)

The bond angle distribution is another important structural property that helps one's understanding of the coordination pattern that is observed in silicate melts, especially for the coordination of Si^{4+} and Al^{3+} network-former cations. Evaluation of the angle distributions was again based on the distance cut offs determined from the first minimum of the PDF curves. The bond angle distributions were calculated for O-Si-O, O-Al-O, Si-O-Si, Al-O-Al and Si-O-Al bridges and are shown in Figures 26 to 30, for the N1 system**.**

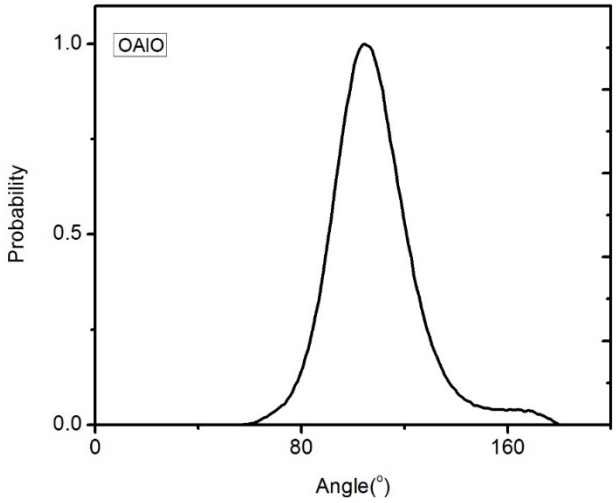

Figure 26. O-Al-O bond angle distribution (BAD) for the simulated N1 system.

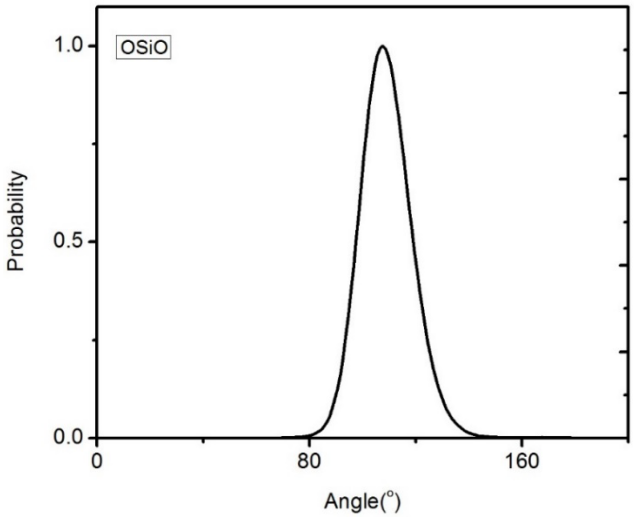

Figure 27. O-Si-O bond angle distribution (BAD) for the simulated N1 system.

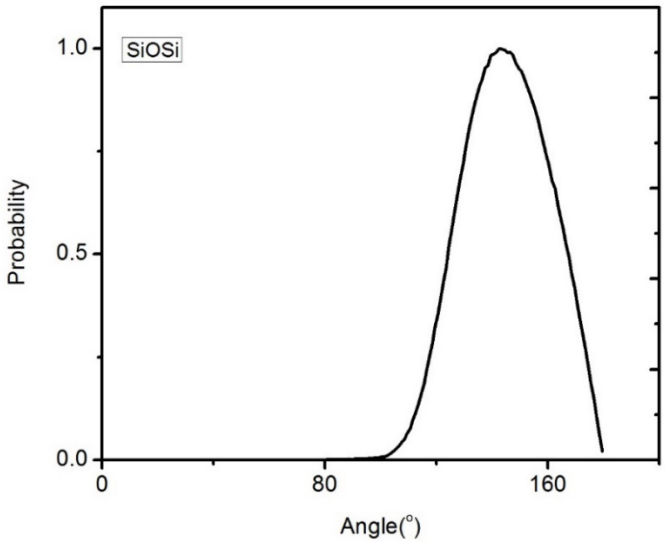

Figure 28. Si-O-Si bond angle distribution (BAD) for the simulated N1 system.

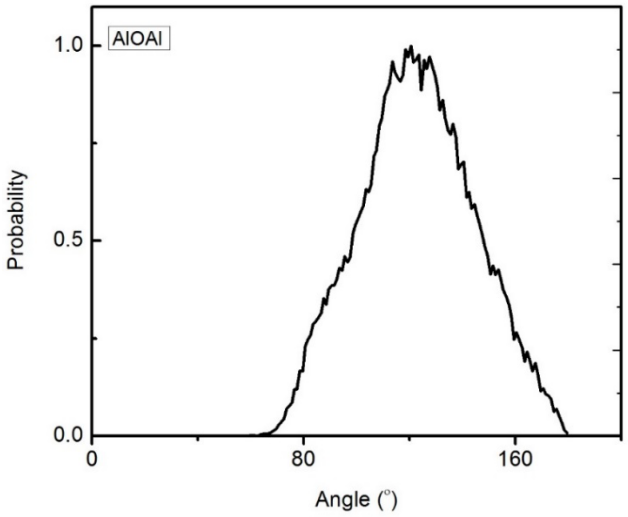

Figure 29. Al-O-Al bond angle distribution (BAD) for the simulated N1 system.

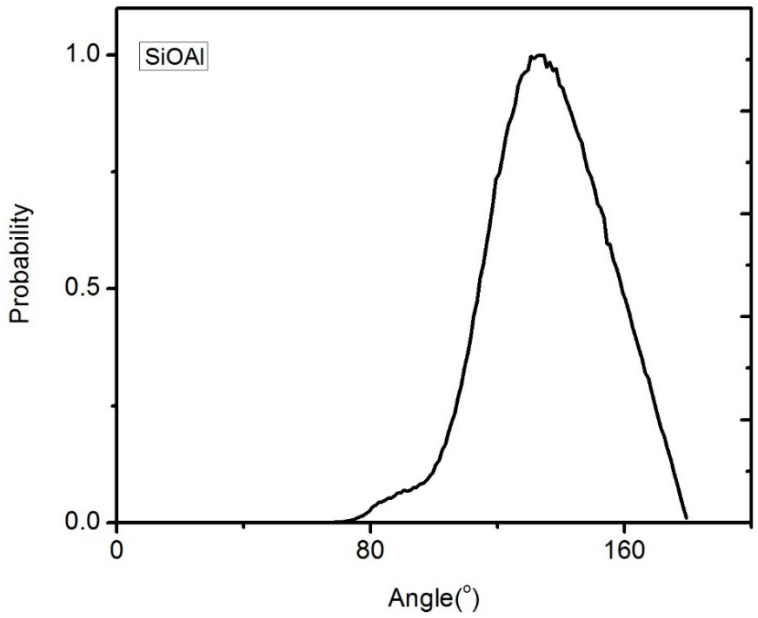

Figure 30. Si-O-Al bond angle distribution (BAD) for the simulated N1 system.

The maxima in the BADs for these bridges are summarised in Table 21. The O–Si–O BAD peaks at 107.5°, showing that the intra-tetrahedral angle is slightly distorted and deviates from the ideal value of 109.4°. The O–Al–O BAD peak is centered at 104.7° with a broad shoulder extending from 150°–180°. The O–Al–O BADs are broader than the corresponding O–Si–O distributions in all the slag systems, indicating a greater distortion of $[AlO_4]^{5-}$ tetrahedra. The BAD for the Si^{4+} cations supports the tetrahedral coordination observed in Figure 25 and the slight deviation from the ideal tetrahedral angle might be due to coordination in transitional states as oxygen atoms migrate through the melt. The relative broadness of the O-Al-O angle distribution compared to that of O-Si-O likely signifies the multiple coordination for Al^{3+} cations that consists of the fraction of fourfold $Al^{[3]}$, threefold $Al^{[4]}$, fivefold $Al^{[5]}$ and six fold $Al^{[6]}$, which are more pronounced as shown in Figure 25. Generally, these angles deviate from the ideal value of 109.4°, indicating that MO_4 tetrahedra do deform with a changing composition and the distortion is significant in the $[AlO_4]^{5-}$ intra-tetrahedral angle.

The Si–O–Si BADs are broad, asymmetric and their peaks generally decrease from 143.8° to 140.9° with an increasing basicity. A similar observation was reported by Xiang and Du (Xiang and Du 2011), where the introduction of network modifiers decreases the Si–O–Si angles in the silicate networks. The consensus regarding angle distribution for pure silica is reported to

be in the range of 146-151° (Vuilleumier, Sator et al. 2009). In the case of CMAS systems, the shift in angle may thus be attributed to the presence of alkali ions that causes the distortion of Si–O–Si angles. The Al–O–Al BADs for the slag systems are centered around 121°. These Al–O–Al angular distributions are uneven showing numerical noise and does not present a clear maximum, as in the case of the Si–O–Si BAD. This might be due to low numbers of these linkages, which is consistent with the fact that the aluminium avoidance principle is not necessarily adhered to in these aluminium silicate melts.

Finally, the Si–O–Al BAD distributions were analysed and the average BAD peak for these bridges was localised at 134°. The Si–O–Al angle distribution shows a more pronounced shoulder around 80°–100° than that of the Si–O–Si and Al–O–Al bridges.

Table 21. Bond angle distribution for network-former oxides (°)

	Si–O–Si	Al–O–Al	O–Si–O	O–Al–O	Si–O–Al
N1	143.8	120.7	107.5	104.7	134.0
N2	142.9	120.7	107.5	104.7	134.0
N3	143.8	120.7	107.5	104.7	134.0
N4	142.5	120.7	107.5	104.7	134.0
N5	142.0	120.7	107.5	104.7	134.0
N6	141.7	120.7	107.5	104.7	134.0
N7	140.6	120.7	107.5	104.7	134.0
N8	140.7	120.7	107.5	104.7	134.0
N9	140.9	120.7	107.5	104.7	134.0

5.5.6. Q^n distributions for Si and Al

The degree of polymerisation can be quantified by the number of NBOs per tetrahedrally coordinated framework cation, NBO/T. Alternatively, the index $Q^n = 4 - \text{NBO/T}$ can also be used. Q^n(Si) is defined as the number (n) of BOs associated with a $^{[4]}$Si atom. This notation is conveniently associated with the degree of polymerisation, in that higher values of n indicate greater polymerisation. In addition, since Al is also able to play the role of structure former, Q^n(Al) is similarly defined for the Al atoms. It should be noted that this quantification is restricted to tetrahedrally coordinated cations and there is no unambiguous treatment of $[AlO_5]^{5-}$. The Q^n(Si) speciation was determined for each slag system, and is shown in Figure 31.

Figure 32 shows the same information, but plotted against mol % SiO_2, since at constant Al_2O_3 composition the extent of polymerisation is better expressed in terms of the SiO_2 content alone. I see Q^2, Q^3 and Q^4 species increase with an increasing amount of SiO_2 (and thus decreasing MgO and/or CaO content), whereas Q^0 and Q^1 decrease. At higher silica content, polymerisation is indeed favoured, as evidenced by the rapid rising of the more polymerised Q^3 and Q^4 species. This is similar to recent simulation results of $CaO–SiO_2$ and $CaO–Al_2O_3$ slags by Wu (Wu, He et al. 2015).

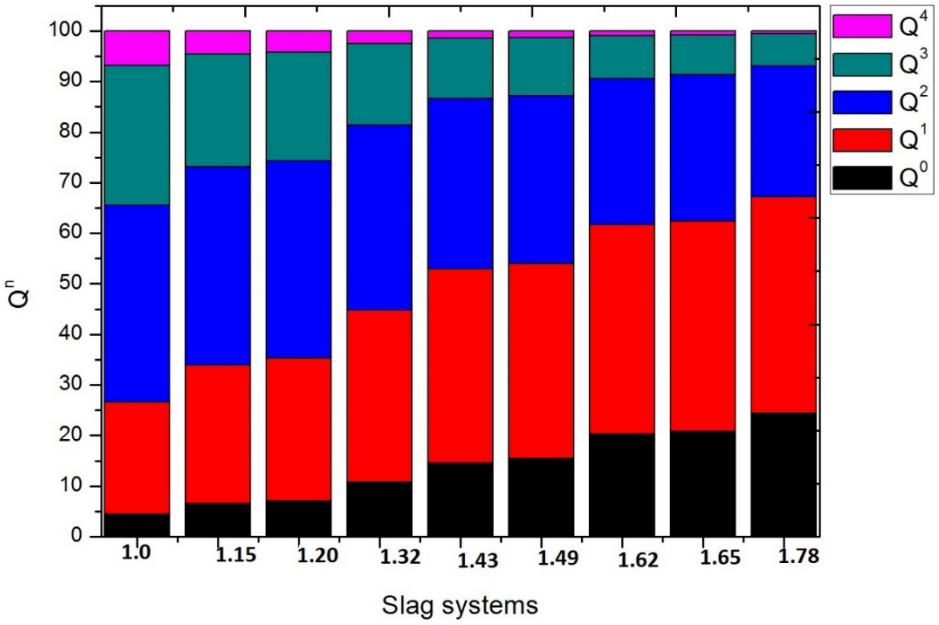

Figure 31. Distribution of Q^n(Si) species, where Q^n(Si) is a tetrahedral $[SiO_4]^{4-}$ species with n bridging oxygens associated with it. The slags systems are given in terms of basicity.

It is interesting to compare the average Q^n value from MD simulation with that estimated from composition expressed in mole fractions (Mills 1993),

$$Q^n = 4 - \frac{NBO}{T} = 4 - \frac{2\left(x_{MgO} + x_{CaO} - x_{Al_2O_3}\right)}{x_{SiO_2} + 2x_{Al_2O_3}} \tag{66}$$

The correlation is shown in Figure 33 and is good at low basicity. As was previously observed, however, the NBO/T ratio, estimated from composition, deviates from simulation at high basicity, which consequently leads to a greater deviation in calculated Q^n.

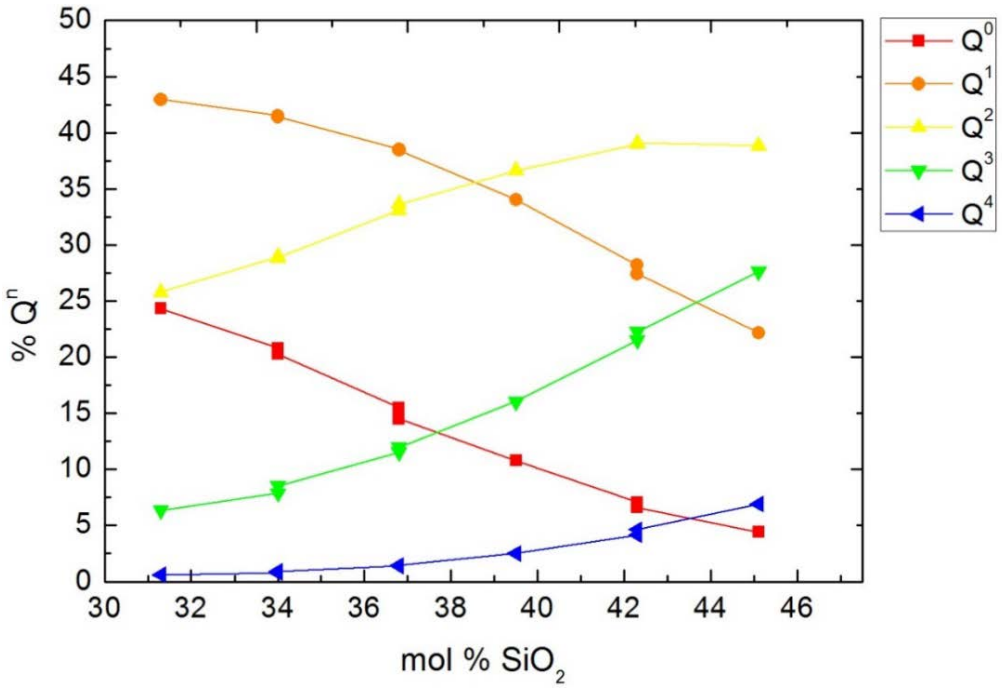

Figure 32. The Q^n(Si) speciation in each of the simulated silicate slags as it varies with SiO_2 content. As the SiO_2 increases the basicity decreases.

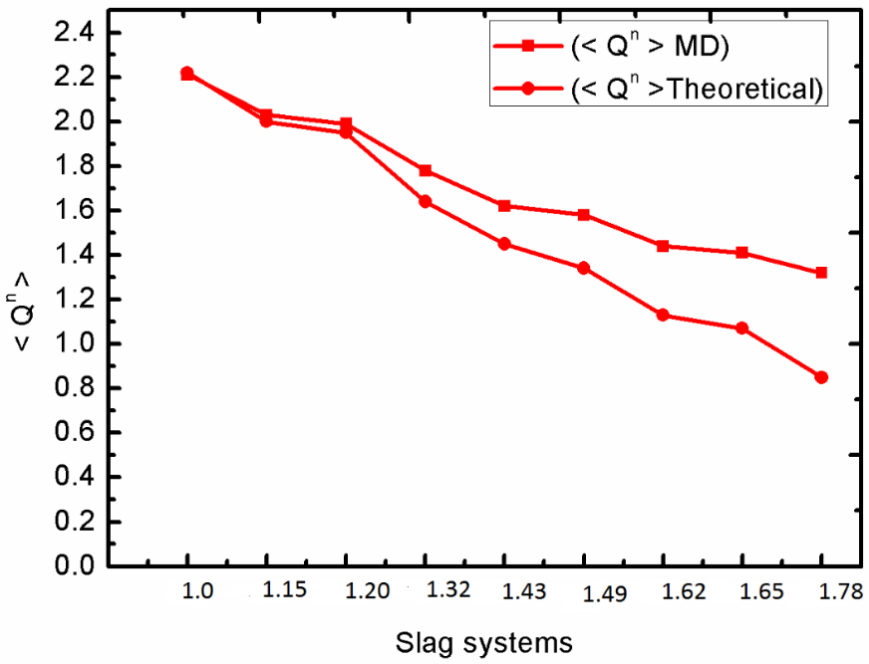

Figure 33. Average Q^n(Si) from MD simulation compared with that calculated from an empirical equation 66. The slags systems are given terms of basicity.

The Q^n speciation of Al was also examined. The results are shown in Figures 34 and 35. The dominant environments are Q^2, Q^3 and Q^4. Globally, the less polymerised species all decrease with an increasing amount of SiO_2 and a consequent decrease in basicity, while the more polymerised Q^3 species increases gradually until about 38 mol % after which it stabilises, and the Q^4 species increases throughout (see Figure 35). This again provides support to the idea that at higher alkalinity, depolymerisation is enhanced. The relatively consistent proportion of the Q^3 species indicates that Al prefers to be localised in these structural units over the range of these compositions. Molecular dynamics simulations of CAS systems by Zheng et al.(Zheng, Yang et al. 2014) indicated that Al exhibits a strong preference for Q^4 species over the less polymerised Q^3 and Q^2 species. These simulations were, however, at lower CaO concentration, and so a more structured network with higher Q^n is to be expected.

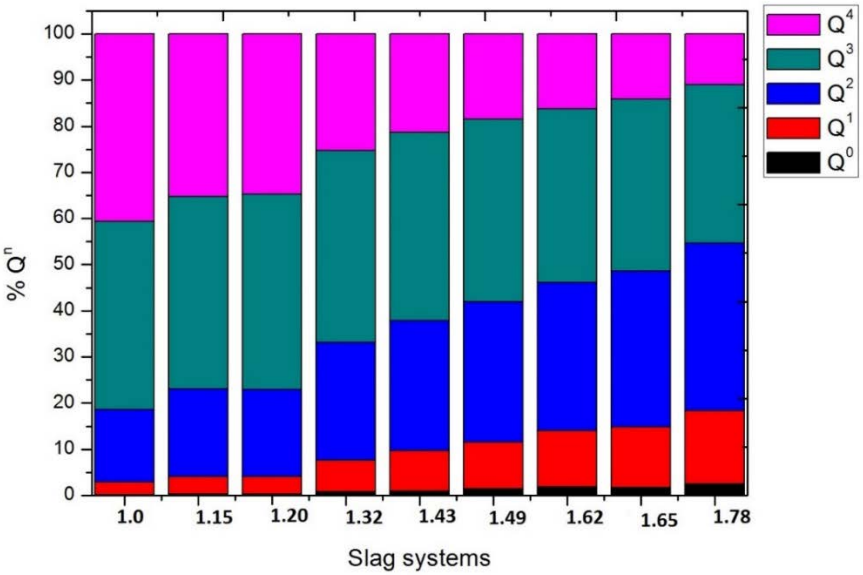

Figure 34. Distribution of Q^n(Al) species, where Q^n(Al) is a tetrahedral $[AlO_4]^{5-}$ species with n bridging oxygens associated with it. The slags systems are given in terms of basicity.

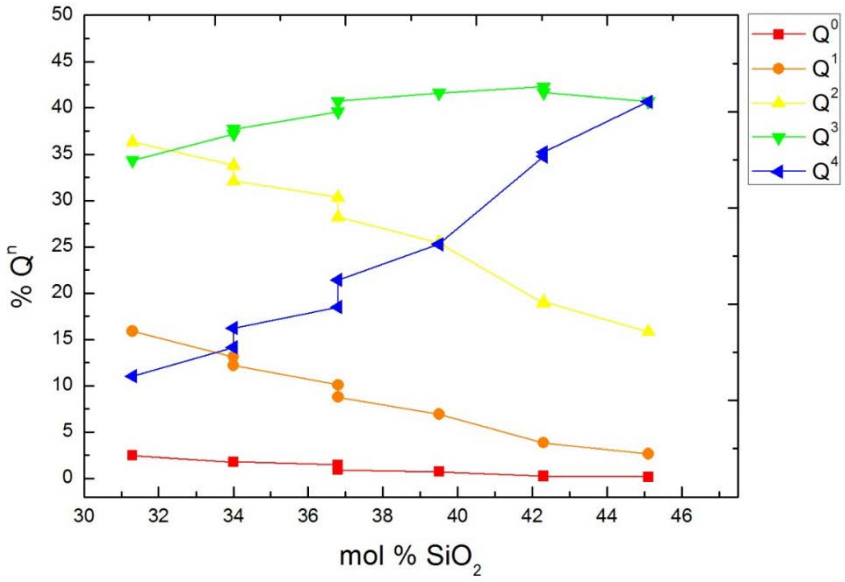

Figure 35. The Q^n(Al) speciation in each of the simulated silicate slags as it varies with SiO_2 content. As the SiO_2 increases the basicity decreases.

5.6. Transport properties

5.6.1. Self–diffusion coefficients

Figure 36 shows a typical plot of the time dependence of the mean square displacement. The resulting diffusion coefficients for systems N1 to N9 are shown in Table 22. Here the reported uncertainties have been calculated as standard deviations for each simulated composition.

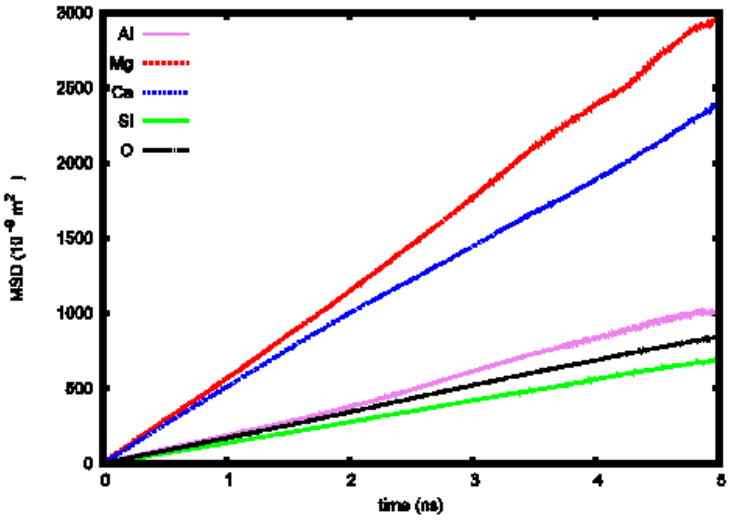

Figure 36. MSD curve for each ion type in the N2 slag system. The MSDs were calculated using the full 5 ns of NVT production simulation.

The decreasing diffusion rate of the cations follows the increase in ionic charge (or ionic field strength where the charges are equivalent) in the order $Mg^{2+} > Ca^{2+} >> A1^{3+} > Si^{4+}$, with the same trend maintained across all compositions. The diffusion coefficient values of O^{2-} are comparable with those of Si^{4+} and Al^{3+}. This trend is similar to that measured by Liang et al. (Liang, Richter et al. 1996) using the isotope tracer method in $CaO–SiO_2–Al_2O_3$ slags at 1500°C and high pressure, and calculated by Tandia et al. (Tandia, Timofeev et al. 2011) and Zheng et al. (Zheng, Yang et al. 2014) using molecular dynamics simulations of calcium aluminosilicates. The relatively high mobility of the Mg^{2+} cation is due to its comparatively smaller ionic radius and, together with the Ca^{2+} cation, are expected to have the highest diffusion coefficients since they are the nonframework cations. These cations sit in the interstitial sites between polymeric chains, allowing them more freedom of movement, and resulting in their diffusion rate being between three to four times quicker than any of the other species. On the other hand, the framework cations and oxygen atoms are expected to be the least mobile, since they are contained within the polymeric structure, in part due to their strong ionic interactions. The general trend for diffusion coefficients is that they increase with increasing basicity as shown in Figure 37.

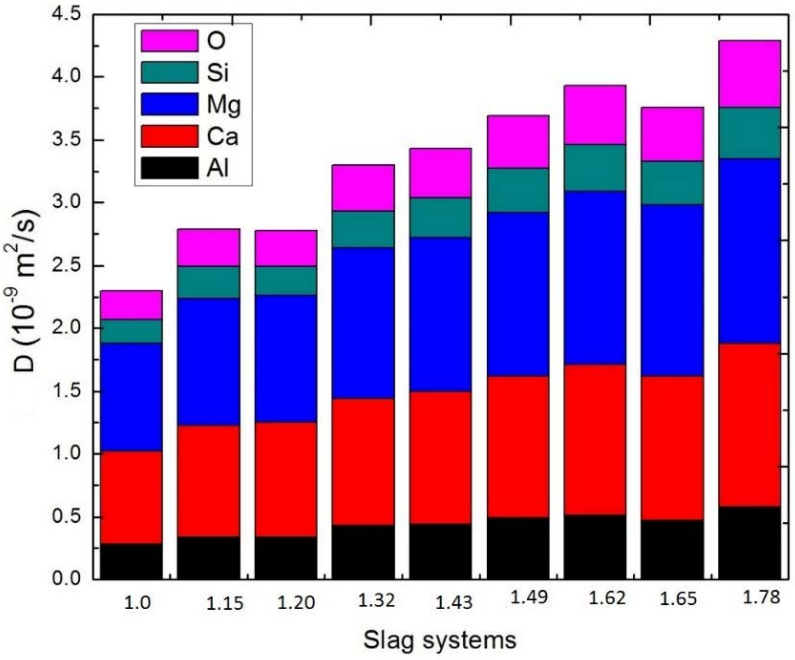

Figure 37. The effect of changing basicity on diffusion coefficients (D). The slags systems are given in terms of basicity.

Table 22. Diffusion coefficients, in units of 10^{-9} m^2/s, of metal cations and the oxygen anion in the simulated slag systems

Slag	Basicity	D(Ca)	D(Mg)	D(Al)	D(Si)	D(O)
N1	1.00	0.74 ± 0.20	0.86 ± 0.09	0.28 ± 0.03	0.19 ± 0.03	0.23 ± 0.01
N2	1.20	0.89 ± 0.09	1.01 ± 0.04	0.34 ± 0.05	0.25 ± 0.05	0.30 ± 0.06
N3	1.15	0.91 ± 0.04	1.01 ± 0.07	0.34 ± 0.03	0.23 ± 0.01	0.29 ± 0.01
N4	1.32	1.01 ± 0.01	1.20 ± 0.08	0.43 ± 0.03	0.29 ± 0.02	0.37 ± 0.01
N5	1.43	1.06 ± 0.05	1.22 ± 0.05	0.44 ± 0.05	0.32 ± 0.02	0.39 ± 0.01
N6	1.49	1.13 ± 0.04	1.30 ± 0.09	0.49 ± 0.06	0.35 ± 0.02	0.42 ± 0.02
N7	1.62	1.20 ± 0.03	1.38 ± 0.10	0.51 ± 0.08	0.37 ± 0.01	0.47 ± 0.02
N8	1.65	1.15 ± 0.10	1.36 ± 0.20	0.47 ± 0.08	0.35 ± 0.03	0.43 ± 0.03
N9	1.78	1.30 ± 0.04	1.47 ± 0.04	0.58 ± 0.03	0.41 ± 0.05	0.53 ± 0.01

Figure 38 shows the trend in diffusion coefficients together with the corresponding $<Q^n>$ speciation. As discussed before, a lower $<Q^n>$ value is an indicator of greater depolymerisation, and hence it is expected that the diffusion coefficients to increase as $<Q^n>$ decreases. This trend is observed in Figure 38. In addition, the figure clearly illustrates the difference in mobility between the framework (Al, Si and O) and nonframework (Mg, Ca) species, since their diffusion coefficients separate into two groups. This was also noted by Zheng et al. (Zheng, Yang et al. 2014), who suggested using an expression based on the diffusion coefficients of Al and Si and their relative concentration, to model the O diffusion:

$$D(O) = \left[\frac{x_{SiO_2}}{x_{SiO_2} + x_{Al_2O_2}}\right] D(Si) + \left[\frac{x_{Al_2O_3}}{x_{SiO_2} + x_{Al_2O_3}}\right] D(Al) \qquad (67)$$

Although this expression underestimates the diffusion of the oxygen atoms, there is agreement (Figure 38), which substantiates that the rate of diffusion of the O atoms depend on that of the Al and Si atoms.

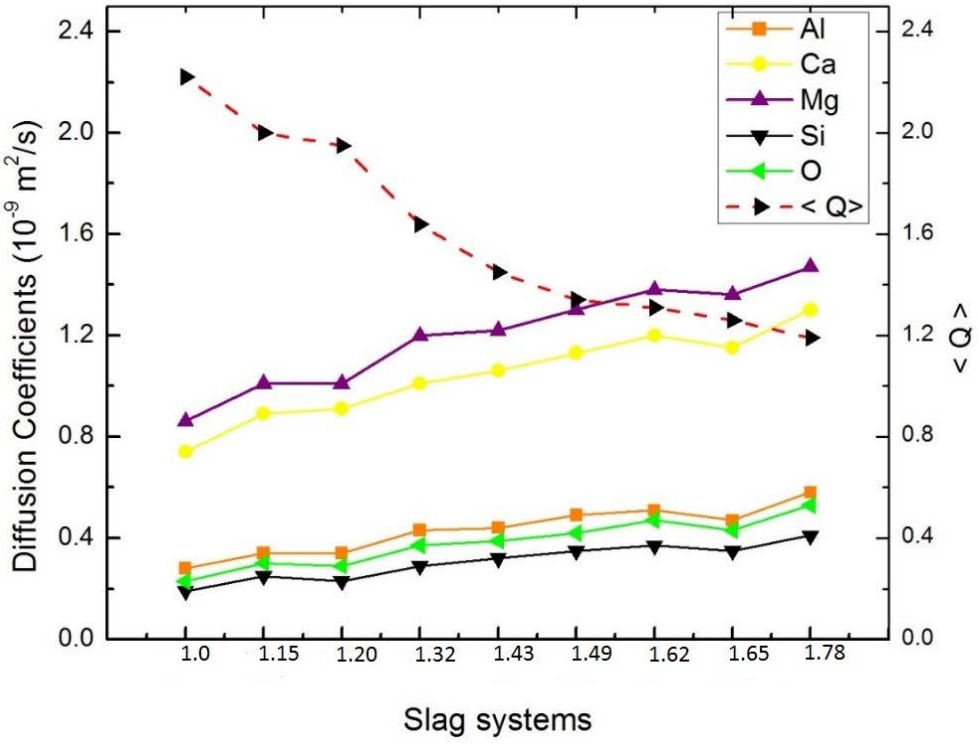

Figure 38. Diffusion coefficients of all ions and, for comparison, $<Q^n>$. The slags systems are given in terms of basicity.

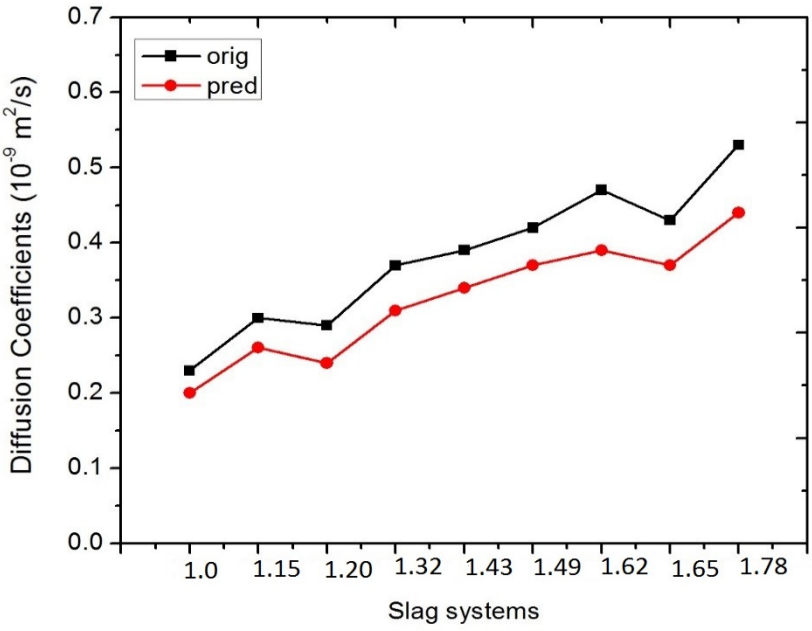

Figure 39. Diffusion coefficients (10^{-9} m^2/s) of oxygen ions in the silicate slags compared to the model shown in equation 67. The slags systems are given in terms of basicity.

5.6.2. Ionic conductivities

The ionic conductivities, calculated using Equations 60 and 61, are shown, together with experimental values, in Table 23. It is important to mention that, as a collective property, convergence is significantly more difficult to establish than the calculation of diffusion coefficients; consistent results could only be obtained over much shorter time intervals and multiple simulations. This is also reflected in the standard deviations, which are up to 20% in the most extreme cases. As seen with diffusion, the electrical conductivities increase with increasing basicity, decreasing SiO_2 content as well as decreasing $<Q^n>$. Values calculated using the exact approach (Equation 60) are in very good agreement with experiment for compositions N1 to N6. The deviations seen for N7 to N9 could be due to erroneous reporting of these conductivity values in literature (Mills 1995). Firstly, it is expected that conductivity of molten slags at constant temperature should increase with increasing basicity (See Table 26 in Section 6) and the experimental results do not reflect this trend for N7 to N9. In addition, our calculations support the expected trend in that both the NE and exact conductivities yield an increase in conductivity (and diffusion coefficients show greater mobility of the charge carriers), which is in line with the expected behaviour.

Table 23. Ionic conductivities, in units of S/m, calculated using Equation 60 (σ^{exact}) and Equation 61 (σ^{NE}). Experimental values are from Mills (Mills 1995). H_R is the Haven ratio, defined as $\sigma^{NE}/\sigma^{exact}$ (Equation 17).

Slag	Basicity	σ^{exp}	σ^{exact}	σ^{NE}	H_R
N1	1.00	24	23 ± 2.8	46 ± 0.9	2.0
N2	1.20	41	38 ± 7.7	55 ± 1.0	1.4
N3	1.15	44	40 ± 3.6	57 ± 1.2	1.4
N4	1.32	51	51 ± 2.9	69 ± 1.1	1.4
N5	1.43	41	44 ± 2.5	71 ± 2.5	1.6
N6	1.49	45	46 ± 5.1	78 ± 2.0	1.7
N7	1.62	11	56 ± 10.0	82 ± 1.7	1.5
N8	1.65	16	58 ± 0.9	84 ± 0.9	1.4
N9	1.78	11	64 ± 2.6	113 ± 1.9	1.8

It is clear that the NE approximation results in higher values than the experimental and exact conductivities by between 40% and 100%, which can be ascribed to the neglected of cross terms and correlations between different ions which might be of the same type or different types. The NE estimated conductivities from MD simulation probably constitutes an upper limit since correlation effects were not taken into account and all particles are treated as having integer charges. If it is assumed that Al^{3+} and Si^{4+} ions remain in tetrahedral $[AlO_4]^{5-}$ and $[SiO_4]^{4-}$ coordination environments, this would lead to reduced transport of ionic charge as the aggregated species carry the effective charge of the tetrahedral unit, which is a lower charge than would occur if the ions were assumed to migrate independently, each carrying their own valence charge. This correlation can be quantified by using the Haven ratio (H_R), defined in Equation 17 (Le Claire 1970), which falls between 1.4 and 2.0 for the current systems. Further work on the relationship between H_R and the exact conductivity, and a better understanding of the factors that control this ratio, should allow more accurate estimation of this important transport property from ionic diffusion.

As mentioned earlier, transport properties are a function of composition and structure. Hence, the potential relationship between variables of interest (NE and exact conductivities), which are referred to as the response variables or dependent variables, to the independent variables such as BOs, NBOs and basicity was investigated. The fitting was done using linear regression by employing the R statistical software (Team 2013). A response variable y (electrical conductivities in this case) was regressed on a single explanatory variable x (BO, NBO and basicity). The data points were fitted in a straight line model of $y = a + bx$. The correlation coefficients and R^2 values were calculated. Results are shown in Table 24. The correlation between both conductivities (NE and exact) and BO is negative, while the correlation between the NBO and basicity is positive. In terms of magnitude, there is a stronger correlation between the NE conductivity, basicity and BO than NBO. The correlation between exact conductivity and basicity as well as NBO, is almost equal in magnitude. Also, since NE increases with increasing basicity resulting in an increase in NBO, a strong correlation between these variables would be expected. Almost certainly, the effect has arisen because at higher basicities, more bond breakages take place. The next section builds on these results be further investigating the relationship between structural properties and conductivity.

Table 24. Relationship between conductivity (exact and NE), composition and structural properties

		R^2	Correlation coefficient
exact	Basicity	0.59	0.77
	BO	0.57	-0.75
	NBO	0.56	0.75
NE	Basicity	0.91	0.95
	BO	0.81	-0.90
	NBO	0.76	0.87

6. ELECTRICAL CONDUCTIVITY MODEL DEVELOPMENT

As mentioned earlier, electrical conductivity is a key factor determining the design of the power supply in an electrical furnace. For metals such as aluminium, magnesium and titanium, which are produced by an electrolytic process involving a slag or molten salt, electrical conductivity data is essential to successfully optimise the process.

Several general empirical and composition dependent electrical conductivity models for multicomponent slag systems have been developed (Jiao and Themelis 1988, Zhang and Chou 2010, Mills, Yuan et al. 2011, Martin and Derge 1943, Goto, Sasabe et al. 1977, Barati and Coley 2006, Fluegel, Earl et al. 2007). However, these models are unable to predict electrical conductivities of slags over a very wide range of compositions and conditions. The effect of slag chemistry and physical and structural properties are not clearly defined within these models. In addition, effort has been made, as evidenced in the literature (Masson, Smith et al. 1970), to develop models that correlate electrical conductivities of slags with other slag properties or with the structure of slags. A model that correlates structure and electrical conductivity of slags, assuming polymeric structures, was developed by Smith et al. (Masson, Smith et al. 1970). Notably however, this model failed to arrive at acceptable estimations of electrical conductivities.

Since viscosities and electrical conductivities respond to similar factors, i.e., slag chemistry, this led (Martin and Derge 1943) to try and correlate these properties. Tracer diffusivity of ionic species, if known, has been used to approximate the electrical conductivity of each species from the Nernst-Einstein (NE) approximation (Goto, Sasabe et al. 1977). However, in some case large deviations were seen between conductivity values determined experimentally and approximated from the NE equation, leading to the failure of this model. The measured tracer diffusivities did not agree with the diffusivities estimated from the conductivities obtained from the NE equation. This is probably due to the fact that the NE approximation omits cross correlation or interionic forces between the different ionic species. This suggests that the mechanism influencing the diffusivity and electrical conductivity is too complex to be explained by the NE formalism.

A model expressing electrical conductivity as an exponential function (fitted linearly) of molar concentration of Ca^{2+}, Mg^{2+}, Fe^{2+}, Mn^{2+} and Si^{4+} cations was developed by Jiao and Themelis (Jiao and Themelis 1988) for CaO-MgO-FeO-MnO-SiO_2 systems. The model is applicable within a limited composition range as it is based mainly on slags with lower basicities. Also, because the coefficients used in this model were obtained through regression of a few data points at specific temperatures, it is difficult to extrapolate outside its intended range. Hence, extending its application to other temperatures and compositions might introduce considerable errors.

A diffusion-assisted charge transfer (DACT) model was developed by Barati and Coley (Barati and Coley 2006) for CaO-FeO_x-SiO_2 systems. The development of this model involved the measurement of electronic conductivities; it attempted to correlate the dependence of the electronic conductivity on the oxidation state of iron and the mechanism of electron conductance in CaO-SiO_2-FeO_x slags. The applicability of this model to industrial slags is limited by the complexity of the parameters involved, such as measurement of the electronic contribution. In 2003, Hundermark (Hundermark 2003) developed an electrical conductivity model for metallurgical slags, both including and excluding iron oxide and chromium oxide. A linear regression model was employed to relate electrical conductivity and slag composition for MgO-CaO-Al_2O_3-SiO_2 slags. This model is also not universally applicable since it is based on a limited composition range and thus unable to predict electrical conductivities across all slag compositions.

A model of the relationship between electrical conductivity and viscosity was developed by Yan et al. and Chou et al. (Zhang, Yan et al. 2011, Zhang, Chou et al. 2012). This relationship is based on Walden's rule (Mendolia and Farrington 1993, Thibodeau and Jung 2016). This rule assumes that the product of the viscosity and the equivalent ionic conductivity in extremely dilute electrolytic solutions is a constant. Walden's rule is mostly applicable in aqueous electrolytic solutions and in oxide melts. Predicting electrical conductivities from viscosities is not clear cut and although a strong correlation between the two properties is observed in some melts, it is not the case for all systems, as illustrated in work by Zhang and Chou (Zhang and Chou 2012). Both viscosity and electrical conductivity are influenced by the diffusivity of cations, i.e., both properties are dependent on ionic migration (Thibodeau and Jung 2016).

An electrical conductivity model for glasses, which is based on multi-linear regressions, was developed by Earl et al. (Fluegel, Earl et al. 2007). Experimental data obtained from the

SciGlass database was used for the development of this model (Fluegel, Earl et al. 2005). However, the applicability of this model is restricted to composition ranges of 50 to 85 mole percentage SiO_2 and is primarily applicable to alkali bearing melts.

6.1. Artificial neural networks

One of the limitations of the development of a good universal electrical conductivity model is the lack of reliable experimental data to validate multi-component models, before they can be deployed in practical applications. In the current study, it is desired to produce artificial neural network (ANN) conductivity models over a broad range of CaO-MgO- Al_2O_3-SiO_2 molten slag compositions. To the author's knowledge, there is no electrical conductivity model for slags or silicate melts based on ANN models, although this has been done for viscosities (Duchesne, Macchi et al. 2010). Transport properties of molten slags are a function of slag structure, therefore an attempt was made to develop a predictive model for electrical conductivity based on structural properties, rather than mobility properties.

An ANN is a computational approach inspired by the performance of the brain and nervous systems in biological organisms (Jain, Mao et al. 1996, Zhang, Patuwo et al. 1998, Basheer and Hajmeer 2000, De Castro and Timmis 2002). It mimics the structure of a brain by distributing the computations to small and simple processing units called artificial neurons, which are interconnected to form a network (Ahadian, Mizuseki et al. 2010). ANNs are applied to modelling in various, diverse fields such as engineering, commerce and science (Khashei and Bijari 2010, Uysal and Tanyildizi 2012). These models have an advantage over linear regression models as a model function with explicit theoretical basis is not needed. The models are data-driven, self-adaptive methods in that there are few prior assumptions necessary for the problems under study (Zhang, Patuwo et al. 1998, Khashei and Bijari 2010). Further, ANNs are able to generalise the data and are capable of multifactorial analyses for modelling complex patterns. The ability of an ANN model to learn allows the inclusion and interaction of more complex variables since these models are able to detect nonlinearities which are not obvious to the user (Uysal and Tanyildizi 2012, Duchesne, Bronsch et al. 2013). Lastly, these models can be generalized, which enables application of the model to unlearned data. Hence an ANN can often correctly predict the output of the unseen test data set even if it is noisy.

The most widely used ANN model is the feed-forward neural network, also known as multilayer perceptron (MLP). In a (MLP) neural network, each node of a given layer is

connected to all the nodes of the next layer and put in adjacent to each other by parallel connections. Generally, a feed-forward ANN model has three processing units, i.e., an input layer, hidden layer(s), and output layer. Figure 40 shows a typical ANN illustrating the basic structure and terminology. The neighbouring layers of an ANN are fully interconnected by the weight values that are associated with each vector and node in the network. The input parameters are propagated to the neurons of the hidden layer(s) without subjecting them to an activation function. Finally, the network predictions from the output layer neurons are produced.

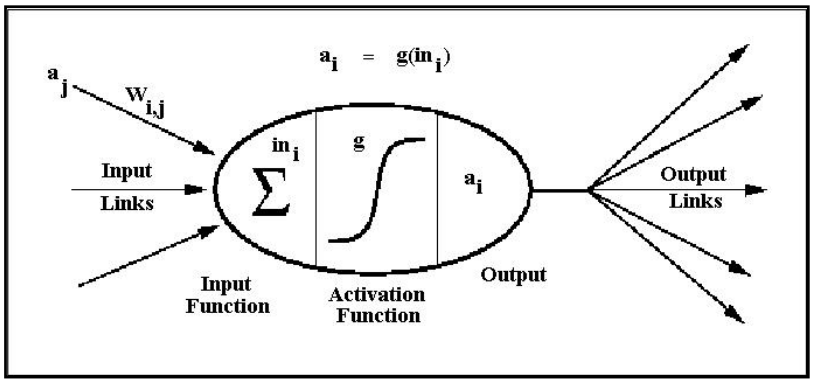

Figure 40. Illustration of artificial neural network (ANN) topology (Elsafi 2014).

Typically, each neuron receives inputs for other neurons and then produces outputs for other neurons.

- Input Layer: The numbers of input nodes comprising this layer are typically equal to the number of state variables in your data. Some ANN configurations add one additional node for a bias term.

- Output Layer: If the ANN is a regression model, as in this case, the output layer can have a single or multiple nodes. In this case, a regression artificial neural network model returns a single value (e.g., an electrical conductivity).

Each input is multiplied by its corresponding weighting factor; these quantities are combined, and then passed through an activation function to produce the output.

$$y_z = f(Z_z) = f(w^T x + b) \tag{68}$$

where y_s is the output of the node, *f(Zs)* is the transfer function, w^T is the connection weight and x is an input signal of the neuron, which corresponds to the weighted sum of the inputs. To train a neural network, data is fitted by training algorithms. Training algorithms can be categorized into two main groups, namely supervised and unsupervised learning. The supervised learning algorithms are characterized by the use of known target values or desired outputs, so that the ANN can adjust its weighting factors to try and match its outputs to the target values. The target values are compared to the predicted output and the differences are used to modify the weights appropriately. In unsupervised learning, the network is provided with inputs and the learning involves using a function to describe the hidden structure from data with no known target outputs. An application of this is clustering, i.e., identifying a set of objects into groups according to their similarity.

During the training process of a neural network, a learning algorithm is used. Two of the most widely used learning algorithms are the resilient backpropagation and the backpropagation algorithms. In backpropagation, the gradient is calculated with respect to all the weights in the network. The backpropagation algorithm comprises two steps: the first step involves a forward activation to produce a solution, and a second step is backward propagation of the computed loss function which is used to update the weights in an attempt to minimise the loss function. The network error, which is the difference between the predicted and target values, is usually reduced by adjusting the weights of the model in order to minimise an appropriate function such as the squares of the errors, using a gradient optimization method (Ahmed 2005). The resilient back propagation updates the weights based on how large the partial derivative of the error function is, the weights are updated based on whether the partial derivative is positive or negative.

The neuron output is determined using a mathematical operation, which controls the relationship between an input and output signal. This operation occurs through an activation function that transforms the input in a linear or nonlinear manner. Activation functions used can be linear, piece wise, Gaussian or sigmoid. Amongst these, the sigmoid function, where β is the slope parameter, is the most widely used, (Zhang, Patuwo et al. 1998):

$$g(x) = \frac{1}{\left(1 + \exp^{(-\beta)}\right)} \tag{69}$$

Performance measurements such as the mean square error (MSE), root mean square error (RMS) and correlation coefficients are used to judge the success of the model. The smaller

MSE indicate that the desired output and the model output for the training set are closer to each other.

$$MSE = \frac{1}{n}\sum_{j=1}^{n}\left(t_j - O_j\right)^2 \tag{70}$$

where *t* and *O* are target and output values respectively, while *n* is the number of the network outputs.

6.2. Model development strategies

The aim of this section is to develop a feed forward neural network for the prediction of electrical conductivities of silicate slags (CMAS) trained by resilient back-propagation, testing different variables and network topologies. Different features, variables and strategies of the model development are outlined in detail below. The models developed in this work uses structural properties as input variables. This is different from previous models, which are often empirical and use compositions as input variables, such as the one by Mills et al. (Mills, Yuan et al. 2011) . To our knowledge, there is no such model, available in the literature that is based on an ANN and structural properties as input variables, for predicting electrical conductivities of silicate slags. The other unique feature of this model is that it uses MD calculated structural properties and electrical conductivities as input and output variables, respectively, for the training, testing and validation phases. This choice has associated with it the advantage of being easily extendable and not confined to use of scarcely available experimental data. However, its disadvantage is the potential variability in the accuracy of MD predicted properties. Although the previous chapter was in part devoted to exploring this latter question, in this section this question again was briefly addressed. The electrical conductivities predicted using the ANN are compared to both MD calculated and experimentally measured conductivities (where available) to see how well the model performs.

The ANN performance is analysed in terms of its mean squared error (MSE) and the coefficient of determination, R^2. The MSE is the average of the squared difference between the actual output and the desired output, while R^2 is a measure of the degree to which changes to the value of one variable result in changes to the value of another variable. Before the model is developed it is a good idea to assess how well the force field predicts the structural properties and experimental conductivities of slags, since these parameters are used for validation. The

structural and transport properties of these slags are therefore briefly discussed in the following section.

6.3. Structural properties

This section briefly analyse the quality of the input parameters for the validation data that was used in model development. It should also be mentioned that not all the analysis done in Section 5 was repeated (only that relevant to model development) and hence to present results on these compositions in Section 5 would appear incomplete/inconsistent. This is important as it might help us to interpret the ANN model. The input parameters were structural properties, which are: BOs, NBO, TBO, free oxygens, and Q^n numbers. The slag compositions and electrical conductivities are shown in Tables 25 and 26, respectively and are arranged in order of increasing basicity as this has proven to be instrumental in predicting the trend of structural properties observed in slags. These compositions were chosen to be the validation data because they have available experimentally measured electrical conductivities. This is important when comparing how well an ANN model predicts MD-calculated and experimental conductivities. As before, cubic simulation boxes were constructed consisting of no less than 1500 and no more than 3000 atoms, based on an approximate mass density and targeting a minimum side dimension of 32 Å. Initial atomic coordinates were randomly generated using the program PACKMOL (Martínez, Andrade et al. 2009) . Given the random starting configurations, the simulation protocol was initiated with relatively long equilibration runs of at least 6 ns at 1823 K and 1 atm pressure in the isothermal–isobaric ensemble (NPT), followed by further simulation for 6 ns in the canonical (NVT) ensemble at the same temperature. In each case the 1st ns was discarded as equilibration within each ensemble. The average density was determined from the final 5 ns of the NPT runs and all structural and transport properties were calculated from the final 5 ns of the NVT simulations. Temperature and pressure control was achieved using a Berendsen thermostat and barostat with relaxation times of 1.0 and 3.0 ps, respectively (Berendsen, Postma et al. 1984). A Nose–Hoover thermostat was used for the NVT simulations, with relaxation time of 2 ps (Berendsen, Postma et al. 1984). The atomic positions were updated using a leapfrog integrator with a time step of 1 fs (Allen and Tildesley 1989) . A cut off radius of 10 Å was used for the van der Waals interactions while electrostatic interactions were calculated using the Ewald summation technique with an accuracy of 1×10^{-6} (Allen and Tildesley 1989). Atomic positions were saved at a frequency of 1000 (i.e., 1 ps) time steps. The DL_POLY 2.20 code was used for all MD simulations (Smith and Forester

1996). All structural analyses and transport property calculations were done using codes distributed with DL_POLY and supplemented with additional codes written by our group. The slag systems used as validation set were taken from Winterhager, Greiner et al. (Winterhager, Greiner et al. 1966) and are denoted as W in Table 25. The electrical conductivities for these systems are shown in Table 26.

Table 25. The slags compositions (wt. %) used as the validation data for the ANN model

Slag systems	Al_2O_3	CaO	MgO	SiO_2	Total	Basicity
W6	3.5	25.0	7.4	64.1	100	0.48
W5	4.0	28.3	8.1	59.6	100	0.57
W15	20.0	29.5	8.4	42.1	100	0.61
W14	15.0	31.3	8.9	44.8	100	0.67
W4	4.5	31.7	9.0	54.8	100	0.69
W1	18.9	35.8	5.7	39.6	100	0.71
W13	10.4	33.0	9.5	47.1	100	0.74
W2	17.9	33.9	10.7	37.5	100	0.81
W3	5.0	35.0	10.0	50	100	0.82
W10	4.8	33.7	13.4	48.1	100	0.89
W7	4.7	38.4	9.5	47.4	100	0.92
W11	4.6	32.3	16.9	46.2	100	0.97
W8	4.5	41.6	9.0	44.9	100	1.02
W12	4.4	30.7	21.1	43.8	100	1.07

Table 26. The electrical conductivities (S/m) of slags used as the validation data for the ANN model. The slag systems have been rearranged to be in order of basicity. Slags were taken from Winterhager, Greiner et al. (Winterhager, Greiner et al. 1966).

System	Basicity	σ^{EXP}	σ^{EXACT}
W6	0.48	9	11 ± 1.6
W5	0.57	14	18 ± 1.6
W15	0.61	28	28 ± 3.1
W14	0.67	10	25 ± 2.6
W4	0.69	21	20 ± 0.5
W1	0.70	21	29 ± 1.4
W13	0.74	23	29 ± 5.9
W2	0.81	27	38 ± 2.9
W3	0.82	29	31 ± 3.3
W10	0.89	34	35 ± 6.5
W7	0.92	34	30 ± 4.0
W11	0.97	39	42 ± 7.3
W8	1.02	39	40 ± 6.3
W12	1.07	46	48 ± 11.6

The exact electrical conductivities were calculated using the Einstein relation, taking cross–correlations into account. The degree of polymerisation of the melt can be investigated by quantifying the extent to which $[SiO_4]^{4-}$ and $[AlO_4]^{5-}$ tetrahedral units are connected. The extent or degree of polymerisation provides information which relates to the mass and charge transport, which influences macroscopic properties such as conductivity. A higher degree of depolymerisation increases the conductivity and vice versa. The degree of polymerisation of silicate melts can be quantified in terms of structural properties such as bridging oxygen (BOs), nonbridging oxygen (NBOs) and three–bonded oxygen atoms (TBOs) or triclusters, which are shown in Figure 41. These properties were determined in the same manner as before.

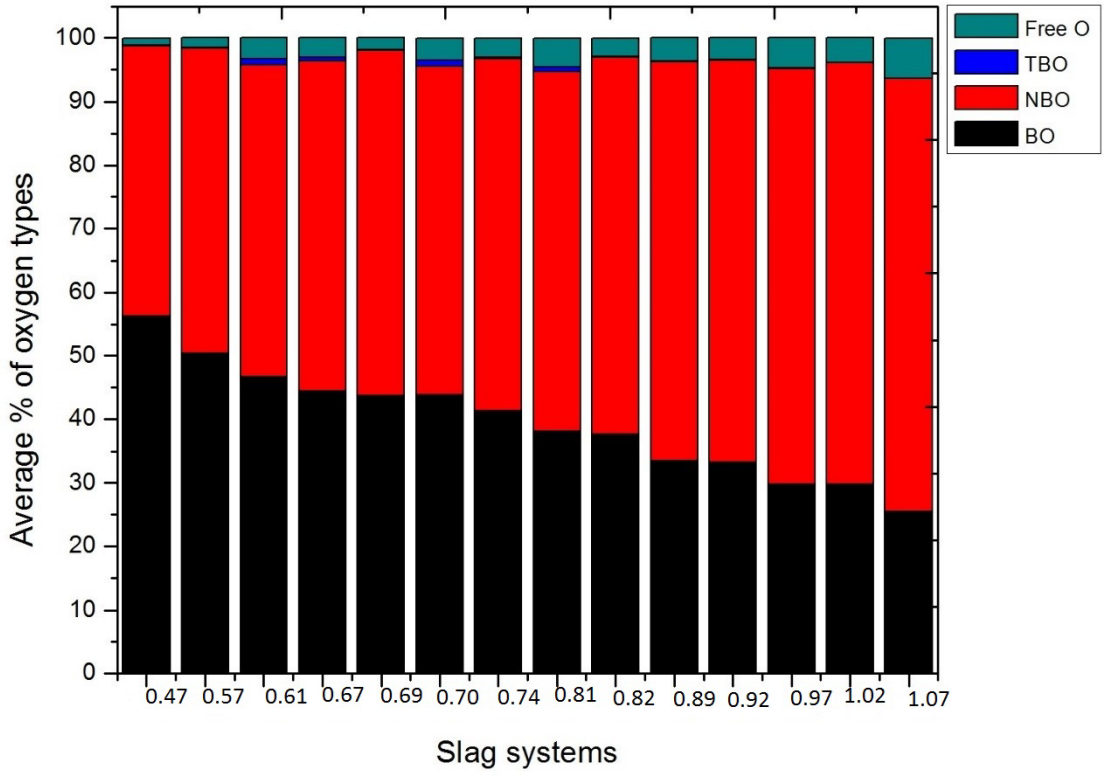

Figure 41. Different oxygen types in slag systems. Slags systems are shown in terms of basicity.

The percentage of NBOs increases with increasing basicity, since the relative amount of network modifying Ca^{2+} and Mg^{2+} ions increase. In addition, there are also high numbers of free oxygens, which increase with increasing basicity. There is also the presence of TBO for slags with a greater amount of Al_2O_3 oxides, i.e., the manifestation of TBO takes place for slags with between 15 and 20 %w of Al_2O_3. Using equation 56, the number of NBOs were calculated theoretically in order to see how they compare to the MD calculated values. Results are shown in Table 27 and Figure 42. On average, these two values compare well. The theoretical NBOs increase with an increasing basicitiy with the exception of W3, W6 and W8. An increase of NBOs with basicity is expected as it promotes depolymerisation of slag systems. The coefficient of determination, R^2, between the theoretical and MD calculated NBOs stands at 92%.

Table 27. MD calculated and theoretically calculated NBOs

Slag systems	MD Calculated NBO	Theoretical NBO
W6	43	42
W5	48	48
W15	49	40
W14	52	47
W4	54	54
W1	52	45
W13	55	54
W2	57	53
W3	59	61
W10	63	66
W7	63	66
W11	65	71
W8	66	71
W12	68	77

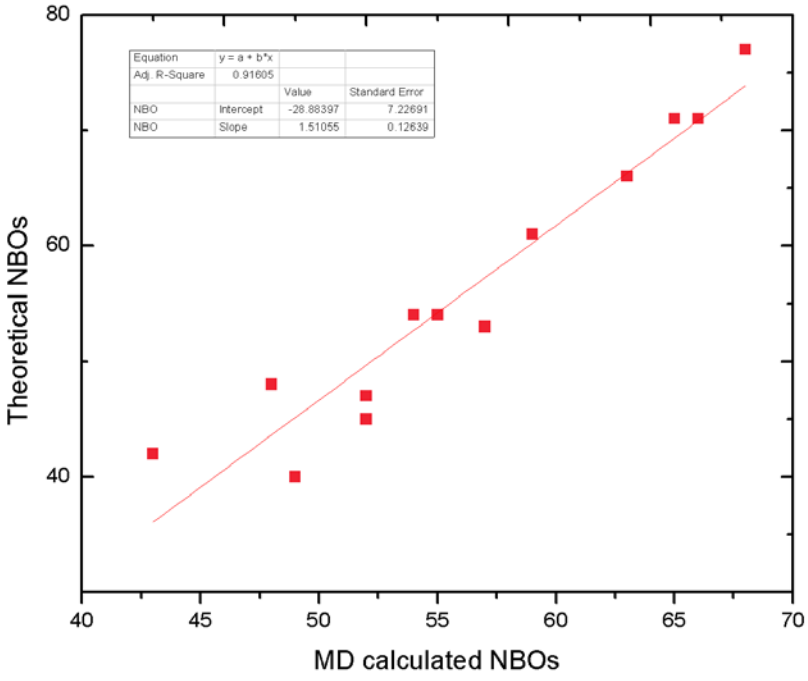

Figure 42. The relationship between MD and empirically calculated NBOs.

The degree of polymerisation is next quantified by the number of NBOs per tetrahedrally coordinated framework cation, NBO/T or Q^n(Si, Al) numbers. Higher values of *n* indicate greater polymerisation, as stated earlier. It must be noted that this quantification is restricted to tetrahedrally coordinated cations and there is no unambiguous treatment of $[AlO_5]^{5-}$. The Q^n(Si) and Q^n(Al) speciation were determined for each slag system and are shown in Figures 42 and 44. The observed general trend for Q^n(Si) species is that depolymerisation increases with increasing basicity, i.e., the more depolymerised species (Q^0,Q^1) increases, Q^2 increases initially but then stabilizes, whereas Q^3 and Q^4 decreases . The Q^n(Si) numbers prefer to be localised in Q^2 and Q^3 in these slag systems. This trend is similar to one observed in Nesterenko slags reported in an earlier chapter (Nesterenko and Khomenko 1985).

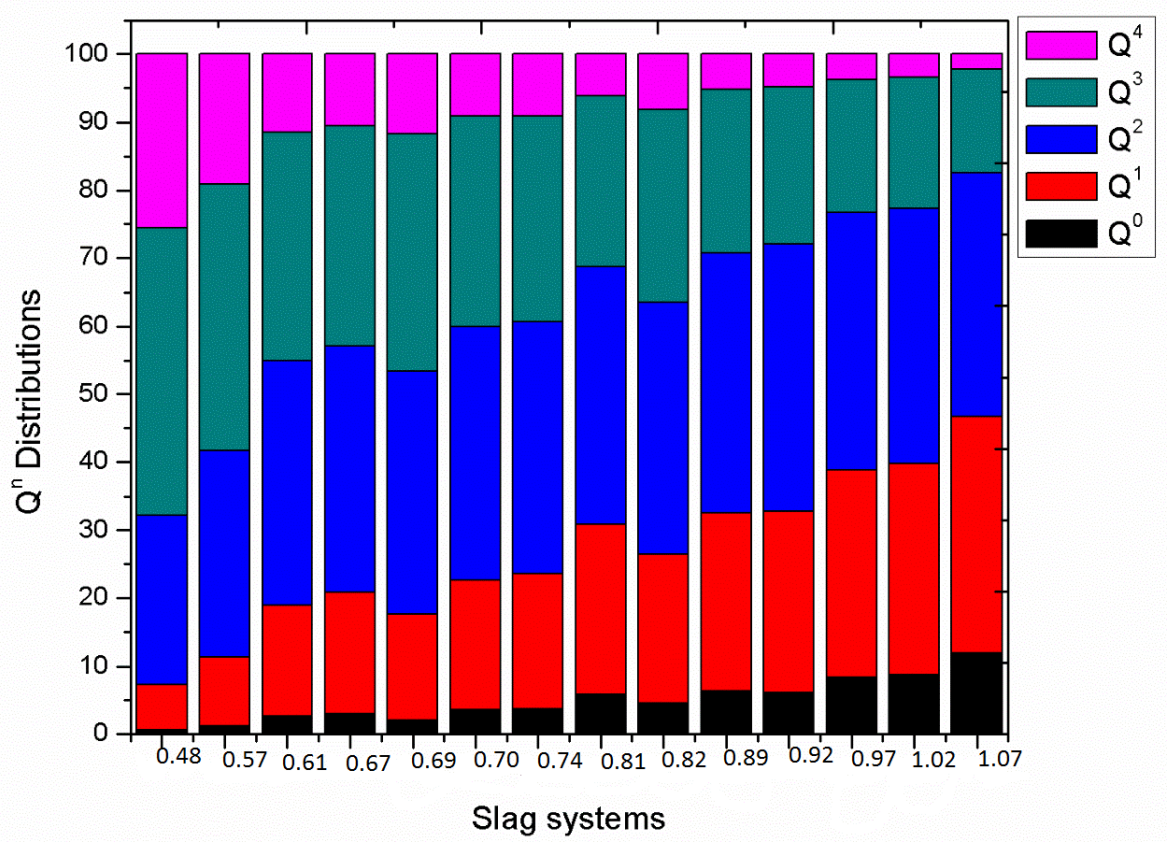

Figure 43. Si (Q^n) distributions in the slag systems. Slags systems are shown in terms of basicity.

For Al, the dominant environments are Q^1, Q^2 and Q^3. Overall, the less polymerised species Q^0 is essentially negligible, Q^1 increases with an increasing basicity and Q^2 is stabilised in all the slags, while the more polymerised Q^3 and Q^4 species decreases with increasing basicity throughout. This again provides support that at higher alkalinity, depolymerisation is enhanced. The relatively consistent proportion of the Q^2 species indicates that Al prefers to be localised

in these structural units over the range of these compositions. Molecular dynamics simulations of CAS systems by Zheng et al. (Zheng, Yang et al. 2014) reported that Al exhibits a strong preference for Q^4 species over the less polymerised Q^3 and Q^2 species. These simulations were, however, at lower CaO concentration and so a more structured network with higher Q^n is to be expected in this case.

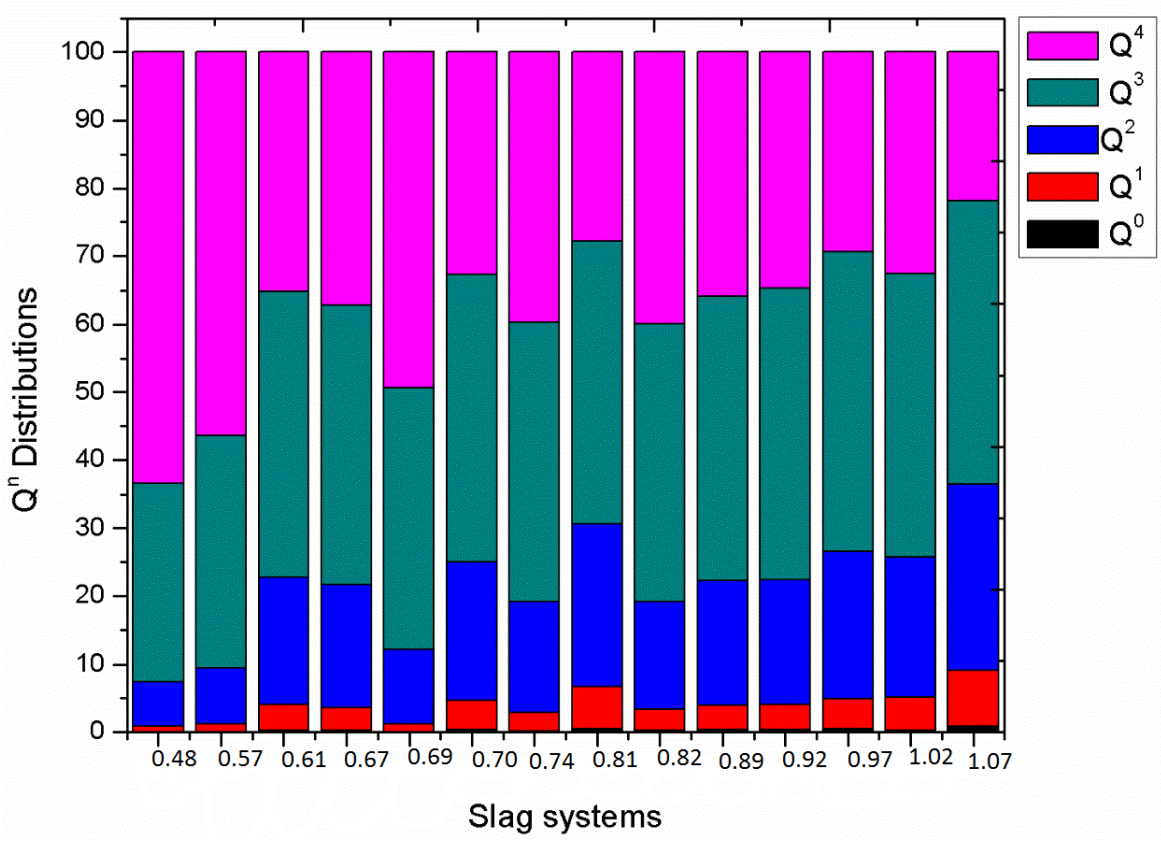

Figure 44. Al (Q^n) distributions in the slag systems. Slags systems are shown in terms of basicity.

6.4. Model development

One of the disadvantages of working on electrical conductivities of slags is the lack of published experimental data that span the full compositional range of these systems for a wide range of temperatures. To develop a model for predicting electrical conductivities of slags I therefore resorted to deriving artificial slag systems that cover a wide range of composition for the training phase. The electrical conductivities were calculated using MD simulations. The force field used in this work was able to predict electrical conductivities with good accuracy (see previous chapter). The composition ranges for these slags systems are shown in Table 28. It is possible that the slags might not remain liquid over the whole composition range at these

temperature, which is likely to affect electrical conductivity as the presence of second phase is likely to hinder the movement of cations and lowers the conductivity. Above the liquidus temperature where there is no presence of a second, solid phase and the conductivity of slags is expected to be higher as there is less or no hindrance to the movement of cations due to an increase in a degree of depolymerisation.

Table 28. Slag composition ranges for training, testing and validation data when using holdout validation (see section 6.8 for an explanation of the validation procedures). The full list of compositions used for training can be found in Appendix B.

Training and validation data composition range (wt %)	
CaO	5 —85
MgO	5 —85
Al_2O_3	5 — 85
SiO_2	5 —85
Testing data composition range (wt %)	
CaO	25 —45
MgO	5.7 — 21
Al_2O_3	3.5 —20
SiO_2	38 —64

After data collection, the next step was to examine the data in detail. Because the structure of silicate melts depends on composition, it was important to explore data features in order to observe the multivariate relationships between different slag components, since these affect the training data. It is good practice to begin by examining relevant scatterplot matrices as this may draw attention to gross errors in the data. This also gave insight into the patterns presented by multiple variables and insight into the spread of our data. Although there are numerous silicate melts in nature and described in the literature, I unfortunately cannot cover all of them and limit the compositions included to the slags with available experimental conductivity values. If successful, this method can be extended to cover a wider composition range. The compositions are graphically represented in Figure 45. In these figures, it is clear that the data covers a broad composition range of the network formers, i.e., SiO_2 and Al_2O_3, with mostly low CaO and MgO, although some compositions with increased amounts of MgO and CaO were included as

well This was assumed to be sufficient, since the structural descriptors (e.g., NBO/BO and Q^n(Si or Al)) depend directly on both the network formers and network breakers.

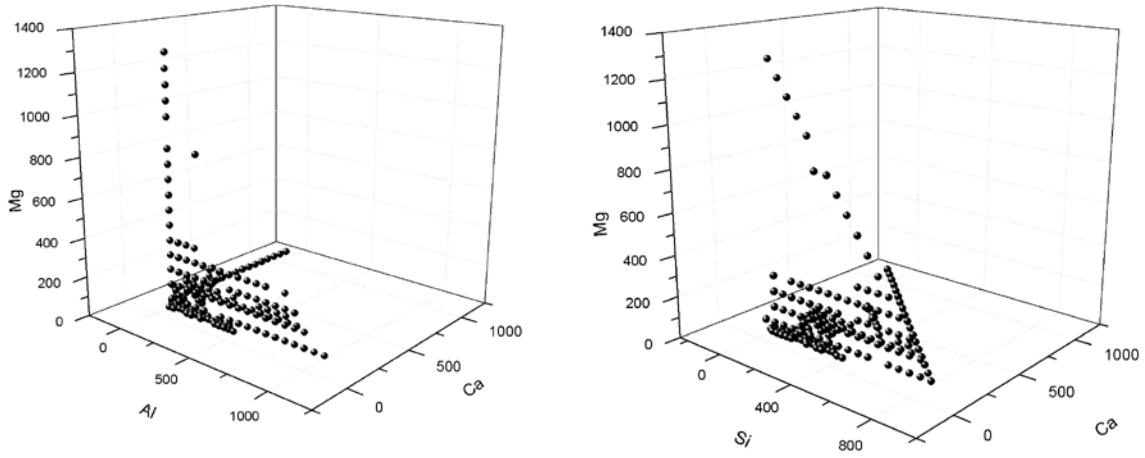

Figure 45. Scatter plots showing the distribution between the network formers (Al atoms in Al_2O_3, left and Si atoms in SiO_2, right) and network breakers (Ca and Mg atoms in CaO and MgO, respectively).

6.5. Relationship between the input and electrical conductivity

In order to establish which input variables might be best suited to further model development, I first checked for linear correlation amongst the input variables as well as between the variables and the electrical conductivity. The relationships between these different parameters are shown in in Figure 46 - 48. In this matrix, the diagonal entries depict the distribution of values for each feature as a histogram. Above the diagonal are correlation matrix values, the intersection of each row and column holds the correlation coefficients for the respective variable pairs, whereas a scatterplot of these pairs are shown below the diagonal. A correlation matrix is a variable that describe the relationship between two or more variable; this usually refers to a matrix of Pearson- type correlations (Benesty et al. 2009).

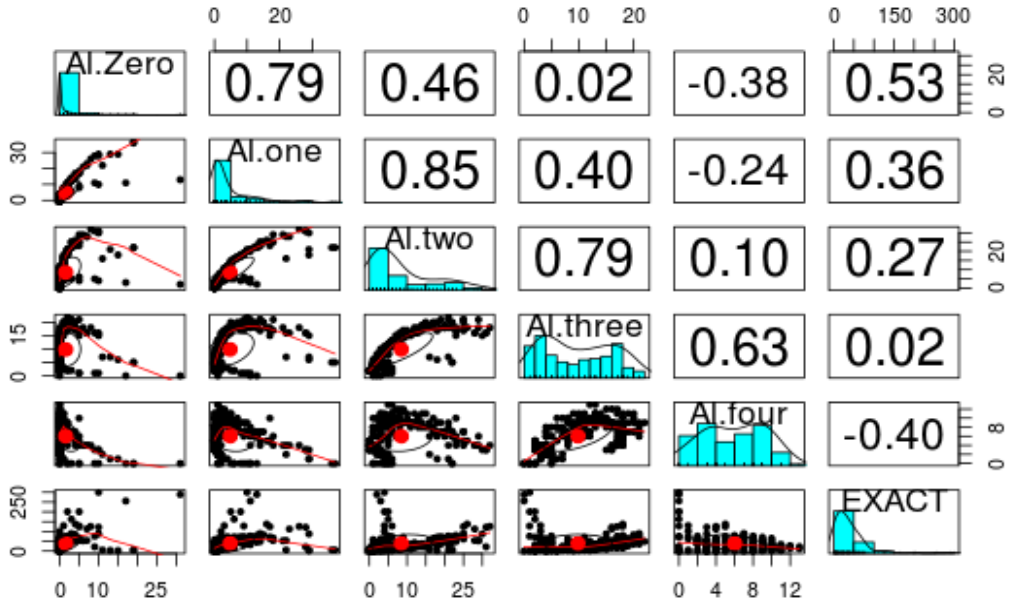

Figure 46. Correlation between the input and output variables which was used for model development. Al.Zero to Al.four denotes Al (Q^0 to Q^4) and EXACT is the electrical conductivity.

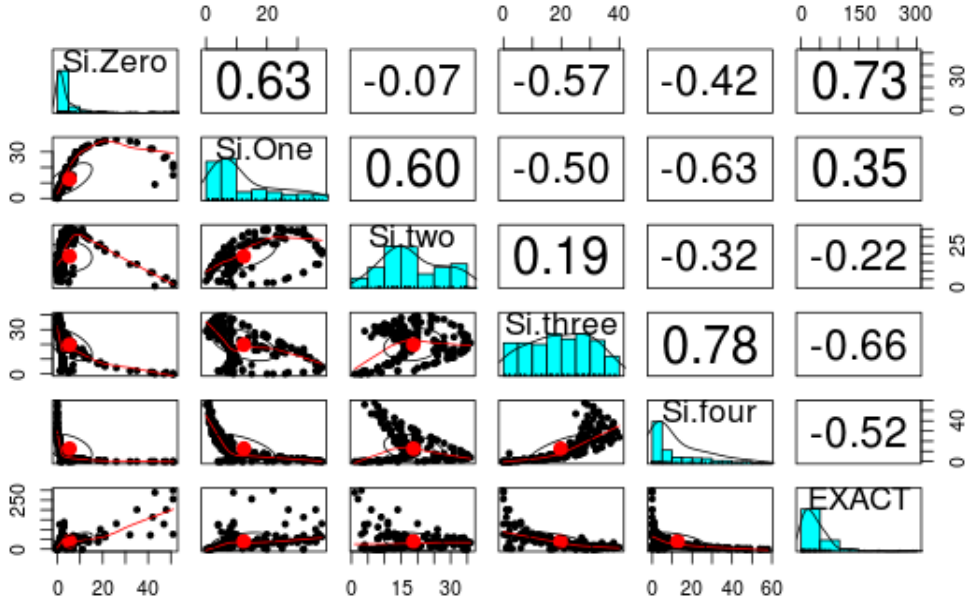

Figure 47. Correlation between the input and output variables which was used for model development. Si.Zero to Si.four denotes Si (Q^0 to Q^4) and EXACT is the electrical conductivity.

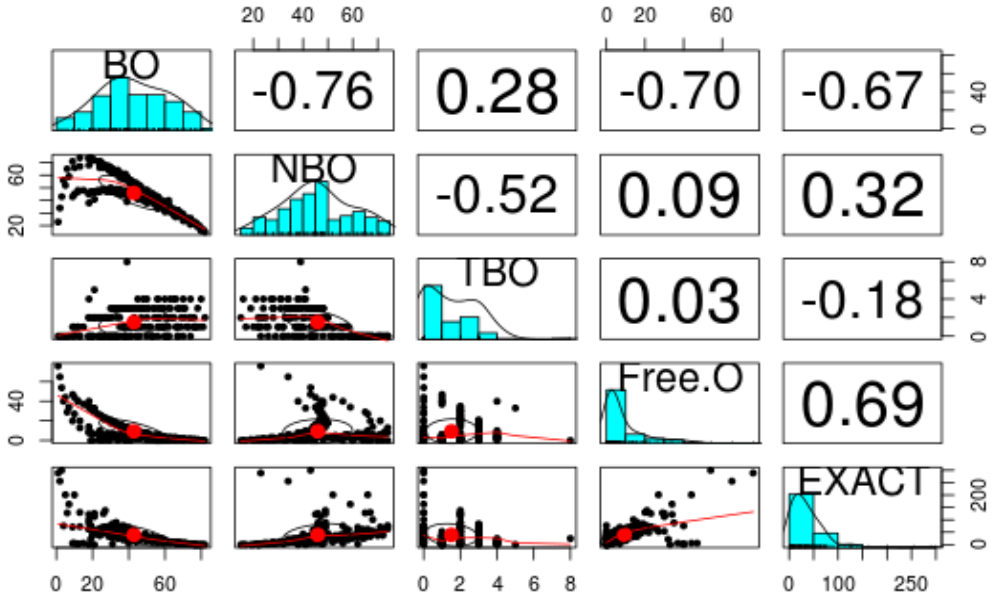

Figure 48. Correlation between the input and output variables which was used for model development. The BO, NBO, TBO, Free.O are bridging, non-bridging, three bridged and free oxygens and EXACT is the electrical conductivity.

The red curve drawn on the scatterplots indicates a best fit relationship between the data points and the red dot is the average. For the Al distributions (Figure 46), there is a weak ($R^2 = 0.53$) positive correlation between Al(Q^0) and conductivity, however, the distribution shows that very little of these species occur in the melt, and so this correlation is perhaps not meaningful. Although other correlations remain insignificant ($R^2 < |0.40|$), it is pleasing to note that the less polymerised species correlate positively with the conductivity (Q^0 to Q^3) and the more polymerised (Q^4), negatively.

For the Si distributions (Figure 47), the correlation between Si(Q^0) and conductivity is stronger than that between Si(Q^1) and conductivity even though the distribution shows that very little of Q^0 than Q^1 species occur in the melt. The correlations between the conductivity and Si(Q^2 to Q^4) species is weakly negative. Again, it is expected that this should be negative, since electrical conductivity is inhibited by greater polymerisation.

For the distribution of oxygen types, there is a negative correlation between the BOs as well as the TBOs and the conductivity, whereas the correlation between NBOs and free oxygens is positive as shown in Figure 48. The opposing correlation of BOs (negative) and NBOs (positive) with conductivity is expected, since these have previously shown to decrease or increase,

receptively, as basicity increases. The correlation between the free oxygens and conductivity is also notable and expected since there were more of these species in the melt during bond forming and breaking associated with decreased polymerisation. As a formally charged, doubly valent anion species, O^{2-}, also makes a greater contribution to the ionic conductivity than when it is associated with the tetrahedral structural units.

6.6. Training procedure

In this section, the procedure and results used in electrical conductivity model development are presented. For the training stage with holdout validation (see section 6.8 for an explanation of the validation procedures), 171 data points were used leaving 18 data points used for validation, while 13 were used for testing. This ratio of approximately 85:9:6 was chosen as a compromise between a sufficiently dense spacing of data points in the training set, validation set and testing set. Whereas the training compositions were generated *ad hoc*, for the testing and validation phases, compositions were chosen for which experimental conductivities were available. It should be reiterated that MD calculated conductivities were used throughout the model development and the choice of experimentally available conductivities were done so that the model could also be evaluated for its ability to predict experimental conductivities without ever having been trained on such data. The system sizes ranged from 1500 to 3000 atoms in total. The smaller system sizes were used to speed up generation of results. It was further confirmed that the system sizes did not significantly affect the properties of the slags by comparing the number of bridging oxygen types from systems with different sizes; this is shown in Table 29.

Table 29. Showing oxygen atom types from the same systems (e.g., M19 and M20), but with a different number of total atoms

Slag	System size	BO	NBO	TBO	Free oxygens
M19	2961	78	20	1.1	0.5
M19	1479	76	23	0.83	0.5
M20	2958	77	21	1.66	1
M20	1479	77	21	1.78	1

The training procedure involves determining the correct model architecture (i.e., number of hidden nodes/layers) and the number of input (i.e., structural descriptors) parameters. The appropriate number of neurons in the hidden layer may depend on three factors:

- The complexity of the correlation between input and output data,
- The number of available training and validation data points, and
- The severity of the noise imposed by the data sets.

A too small number of neurons may render a network unable to reach the desired error limit, while a large number of neurons may result in over-fitting. Various model structures with different number of hidden neurons were investigated. The difference between the predicted electrical conductivity and the MD calculated electrical conductivity was calculated to show the model performance in terms of mean square error (MSE) and coefficient of determination (R^2). The `neuralnet` library in the R software was used for model training, testing and validation. Each of the datasets consists of two parts: input (BO, NBO, TBO, free oxygens, Q^n numbers) and output, which was the MD calculated electrical conductivity (exact electrical conductivity). The input and output data were normalised to fall in the range between 0 and 1 so that the data dimensions are approximately the same scale. In general, the following steps are followed in an artificial neural network development: (1) generation of the training data for the network, (2) evaluation of the different network architectures for selecting the optimal structure using validating data and (3) testing the neural network using the unused data set. Figure 49 shows an example of topology of a trained neural network. The plot includes the trained synaptic weights and all intercepts.

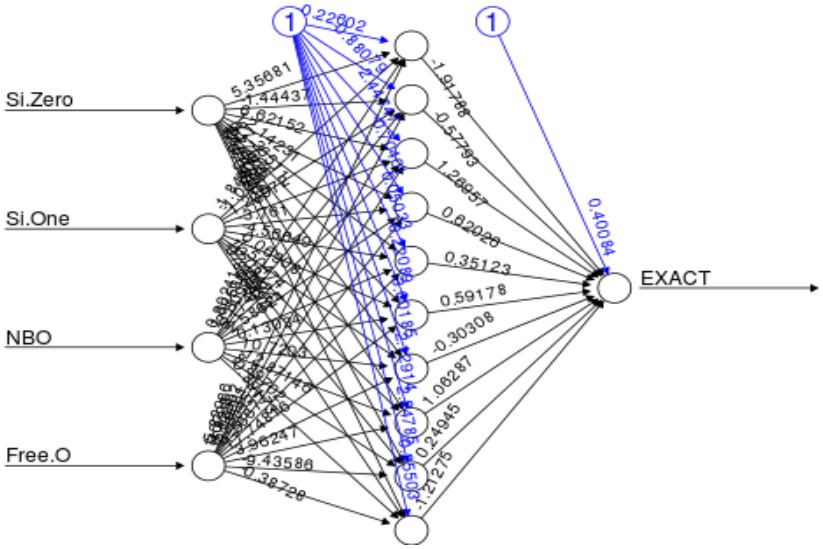

Figure 49. Example of a neural network with four input parameters and one output parameter (exact conductivity) with one hidden layer consisting of ten hidden neurons and the blue lines are biases. Si.Zero and Si.One denote Si (Q^0) and (Q^1), whereas NBO, Free.O and EXACT are the amount of non-bridging, free oxygens as well as the MD calculated electrical conductivity.

The data points are fed to the input layer, which then send signals to the hidden layer automatically. During the training step, the multilayer perceptron (MLP) is repeatedly presented with the training data and the weights in the network are adjusted until the desired input—output mapping occur. Each pair of input and target output was applied to adjust the weights and biases of ANNs with logistic sigmoidal transfer functions.

6.7. Details of the training algorithm

In this study, a feed-forward resilient back-propagation (Rprop) algorithm was used. Implementation details can be found in the book by Bishop (Bishop 2006).

The Rprop algorithm is summarised below:

- The network weights are initialised
- The input parameters from training data are presented to the network
- The input parameters are propagated through the network to obtain an output

- An error signal is calculated by comparing the actual output vector to the desired target vector
- The error signal is propagated back through the network
- The weight vectors are adjusted to minimise overall error
- The above steps are repeated with the same input parameters, until overall error is satisfactorily small

An example command in the R `neuralnet` package used to train a model using the resilient backpropagaion algoritm is (parameters not shown were kept at their default values):

```
neuralnet (formula=f, data= train_, hidden=(7, 4), rep=200, linear.out= T)
```

where `f` is a formula for the model that prescribes which variables are to be used for input and which for output, `_train` is the training data, hidden is the vector specifying the number of hidden neurons in each hidden layer, which are 7 and 4, respectively, `rep` is the number of repetitions for which the model was run (i.e., 200 in total, from which the average MSE and best ANN can be extracted) and `linear.`out specifies whether the activation function should be applied to the neurons in the output layer. This was set to the default value of `TRUE`, which means that the activation function is not applied and a linear output is observed. This is appropriate for regression problems because applying a sigmoid activation function would bound the output in the interval [0, 1] (Forte 2015). The starting weights (`startweights`), a vector containing pre-specified starting values, was also set to the default, which is generated as random numbers drawn from the standard normal distribution. The activation function (`act.fct`) by default is set to the logistic function. In addition, the maximum steps (`stepmax`) were kept at the default value of 100 000 and the upper and lower limit for the multiplication factors (`learningrate.factor`) in the learning rate were 0.5 (negative change) and 1.2 (positive change).

The optimal configuration of the MLP ANN network is determined by an optimization procedure through changing the number of neurons in each hidden layer, as well as using different input parameters. It is possible to also adjust the number of layers, but in this work two layers were used for all models. The difference between the network results from the testing phase and the desired outputs are calculated and used as a criterion for updating the network's parameters. Several approaches were applied to determine the optional number of

hidden neurons and input parameters. Both holdout and 10-fold cross-validation were used to determine optimal number of input and hidden neurons. In addition, some further models were also developed on intuitive basis and were validated using holdout validation.

6.8. Cross validation

Two validation techniques were used in this work, i.e., *k*-fold cross validation and holdout validation. These two techniques are discussed below.

6.8.1. Holdout validation

In holdout validation, the data is separated into three mutually disjoint subsets consisting of the training, validation, and testing set. The training set had 171 data points, validation set 17 data points and test set had 13 data points. The number of neurons in the hidden layer is determined through an optimization procedure that minimizes MSE. The hold out cross validation is summarised as follow:

- Training set: a set of examples used for learning: to fit the parameters of the model. In the `neuralnet` case, I would use the training set to find the "optimal" weights with the back-prop rule.

- Validation set: a set of examples used to tune the parameters of a model. In the `neuralnet` case, I would use the validation set to find the "optimal" number of hidden units.

- Test set: a set of examples used only to assess the performance of a fully-trained model. In the `neuralnet` case, I would use the test to estimate the error rate after I have chosen the final model (neuralnet size and actual weights). After assessing the final model with the test set, the model must not further be tuned.

6.8.2. 10-fold cross-validation

In *k*-fold cross validation (with $k = 10$ in this work), all the training data is divided at random into k distinct subsets, the network is trained using *k*-fold subsets and then validated on the remaining subsets. The training and validation process is repeated for each of the *k* possible choices of the subset omitted from the training. To assess the performance of the model, the average performance across the k subsets is computed and used to estimate the generalised performance. Figure 50 illustrates the sub-setting of data when using 10-fold cross validation.

The full procedure can be summarised as follows:

- The training data is split into *k* equally sized and non-overlapping partitions. The model is then trained using *k*−1 of these partitions and the remaining partition is used as a validation set.

- A suitable number of dimensionalities for the hidden neurons(s) were chosen by validating the performance of the model. For example I might select 7 hidden layers, and 3 neurons or nodes.

- For each of these candidate dimensionalities, I compute a global estimate of the accuracy of our method on unseen data (test data) by aggregating all estimates that I obtained across the *k* different test sets

- I selected the number of hidden neurons whose average testing error over the k trials of point (3) is lowest.

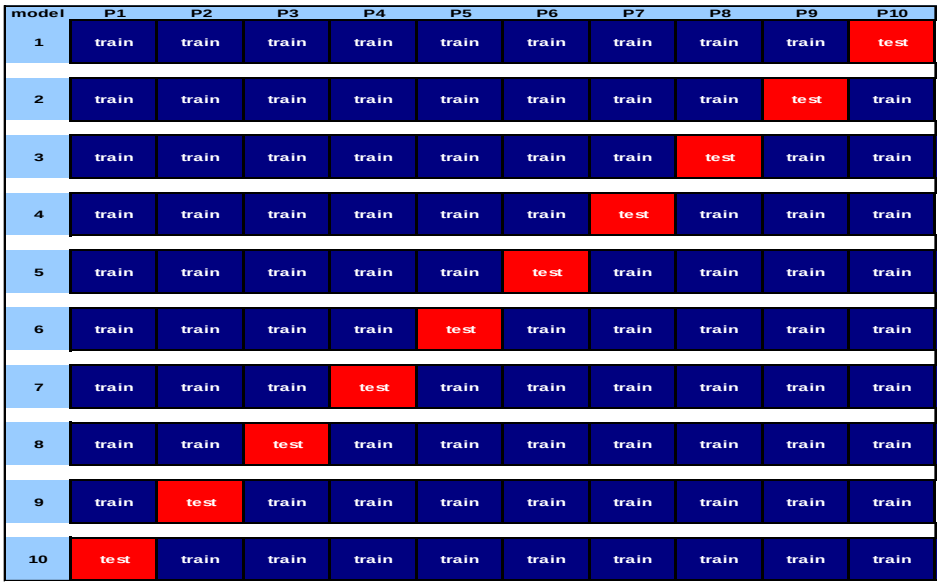

Figure 50. Illustration of a 10–fold cross-validation (Guszcza 2004).

6.9. Model results

Several models using individual input parameters were first developed and are shown in Table 30. Models were first developed using all the individual parameters, however only those with higher correlation and lower MSE are reported in this work. The number of hidden layers were also varied to search for the best models and it turned out that the models with better performance on the test and validation set were those with 3,2 hidden layers. Some of the

models showed higher correlation coefficients and higher MSE values and vice versa when fitted on both the test and validation set. These models predicted the electrical conductivity poorly. Therefore a combination of parameters was used and is discussed later in the chapter.

Table 30. ANN models with different architectures using Si (Q^0–Q^4) as input parameters

	Correlation, R^2	MSE $(S/m)^2$	Hidden neurons
Q^0 Test set	0.74	192.97	3,2(***Si***Q^0)
Q^0 Validation set	0.88	36.15	3,2(***Si***Q^0)
Q^1 Test set	0.97	173.19	3,2(***Si***Q^1)
Q^1 Validation set	0.97	152.25	3,2(***Si***Q^1)
Q^{11} Test set	0.86	950.10	3,2(***Si***Q^1)
Q^{11} Validation set	0.92	1457.65	3,2(***Si***Q^1)
Q^2 Test set	-0.49	336.61	2(***Si***Q^2)
Q^2 Validation set	-0.73	144.60	2(***Si***Q^2)

The models with fewer number of hidden layers and using all the input parameters were developed and the results from the test and validation set are shown in Table 31. At a later stage, the performance of these models were compared to those with many hidden layers.

Table 31. ANN models with different architectures Si (Q^0–Q^4), Al (Q^0–Q^4), BO, NBO, TBO, and free oxygen as input parameters

	Correlation, R^2	MSE $(S/m)^2$	Hidden layers
CT1 Test set	0.79	0.79	1
CV1 Validation set	0.52	111.11	1
CT2 Test set	0.59	592.64	2
CT2 Validation set	0.70	67.57	2
CT3 Test set	0.50	1990.49	3
CT3 Validation set	0.90	34.22	3
CT4 Test set	0.33	868.64	4
CV4 Validation set	0.85	53.31	4

Models using compositions and temperature as input parameters were also developed in this work. Different strategies were tried out during the model development including changing the size of the training set and hidden layers. The best model was found when the size of the training data was set at 94. The test set showed a low correlation coefficient and a high MSE as shown in Table 32. On one hand the validation set showed a high correlation and low MSE. This model is promising even though it uses a smaller size of the training set. The model predicted well the conductivity of the slags as shown in Figure 52.

Table 32. ANN models using composition as input parameters

	Correlations (R^2)	MSE $(S/m)^2$	Hidden layers
COMP Test set	0.59	568.6	5,4
COMP Validation set	0.96	40.86	5,4

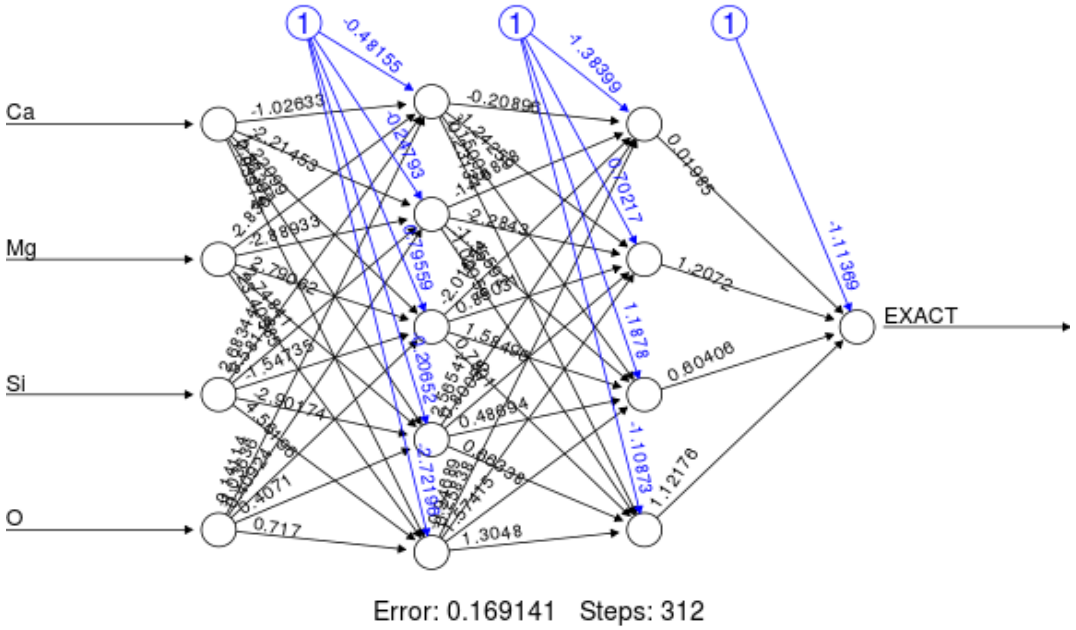

Figure 51. Weights of a neural network with nine input parameters Si (Q^0 - Q^4), BO, NBO, TBOs and free oxygens) and one output parameter (exact conductivity) which has two hidden layers.

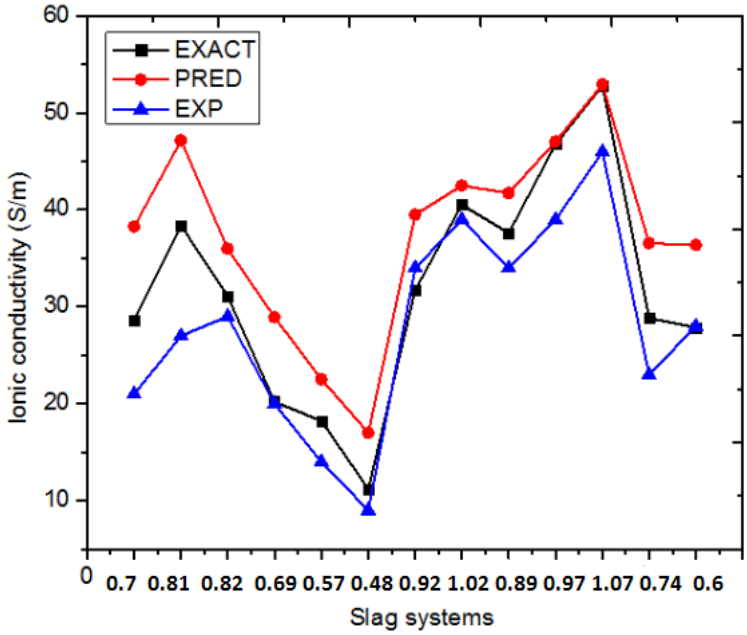

Figure 52. Electrical conductivity of slags predicted using ANN model COMP Validation set compared with MD calculated and experimentally measured electrical conductivity. The x-axis are presented in terms of basicity.

The next set of model used a combination of input parameters and a varying number of hidden layers. Four different set of input parameters were used to develop the ANN models using a pre-determined number of hidden neurons. For the first set of models (M*x*, *x* = 1–9, using holdout validation), the input parameters were Si (Q^0 to Q^4), BO, NBO, TBO and free oxygens. The vector pairs for hidden neurons, input parameters and results for this set of models are shown in Table 33. An example of the topology of the first model is shown in Figure 54.

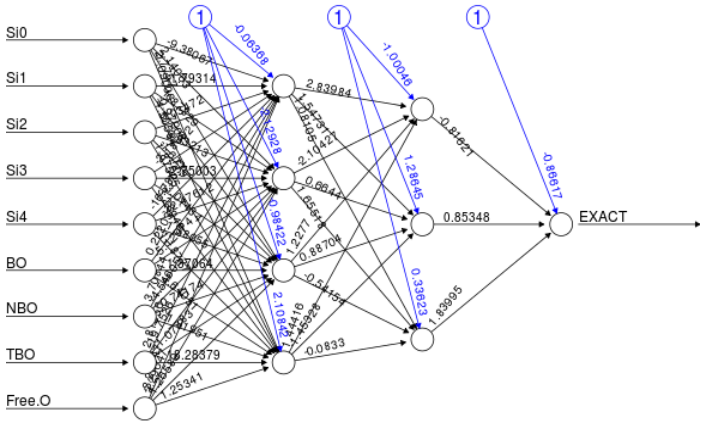

Figure 53. Weights of a neural network with nine input parameters Si (Q^0 - Q^4), BO, NBO, TBOs and free oxygens) and one output parameter (exact conductivity) which has two hidden layers.

The best performing model was identified based on the lowest value of the MSE when applied to the validation set, which is M7 with 7 and 4 hidden neurons. The MSE and correlation coefficient are 69.7 $(S/m)^2$ and 0.88, respectively, for the validation set. Model M7 was applied to the test set to evaluate how well it predicts the electrical conductivity of an unseen data set. The results for the test set are shown in Table 33 and Figure 55. The corresponding MSE and correlation coefficient when applied to the validation data, are 66.0 S/m^2 and 0.67, respectively. Performance is generally good, but the model has large errors (>20%) for W1, W4, W6, W11 and W15, as shown in Table 33. It should also be noted that a few compositions, specifically W13, have large errors between the MD calculated and experimental conductivities.

Table 33. Results for models optimised using Si (Q^0 – Q^4), BO, NBO, TBO, and free oxygen atoms as input parameters

Slag system	σ^{PRED}	σ^{EXACT}	% error
W6	15	11	36
W5	20	18	11
W15	34	28	21
W4	25	20	25
W1	37	29	28
W13	32	29	10
W2	43	38	13
W3	28	31	10
W10	29	35	17
W7	30	30	0
W11	33	42	21
W8	32	40	20
W12	44	48	8

Table 34. Results for model M7 electrical conductivity in (S/m)

Model	Hidden neurons	Correlation factor	MSE $(S/m)^2$
M1	1,2	0.86	84.4
M2	3,2	0.84	153.8
M3	4,3	0.84	110.2
M4	5,4	0.84	102.6
M5	6,5	0.85	119.3
M6	7,6	0.84	304.5
M7	7,4	0.88	69.6
M8	8,9	0.68	332.0
M9	9,3	0.54	849.2

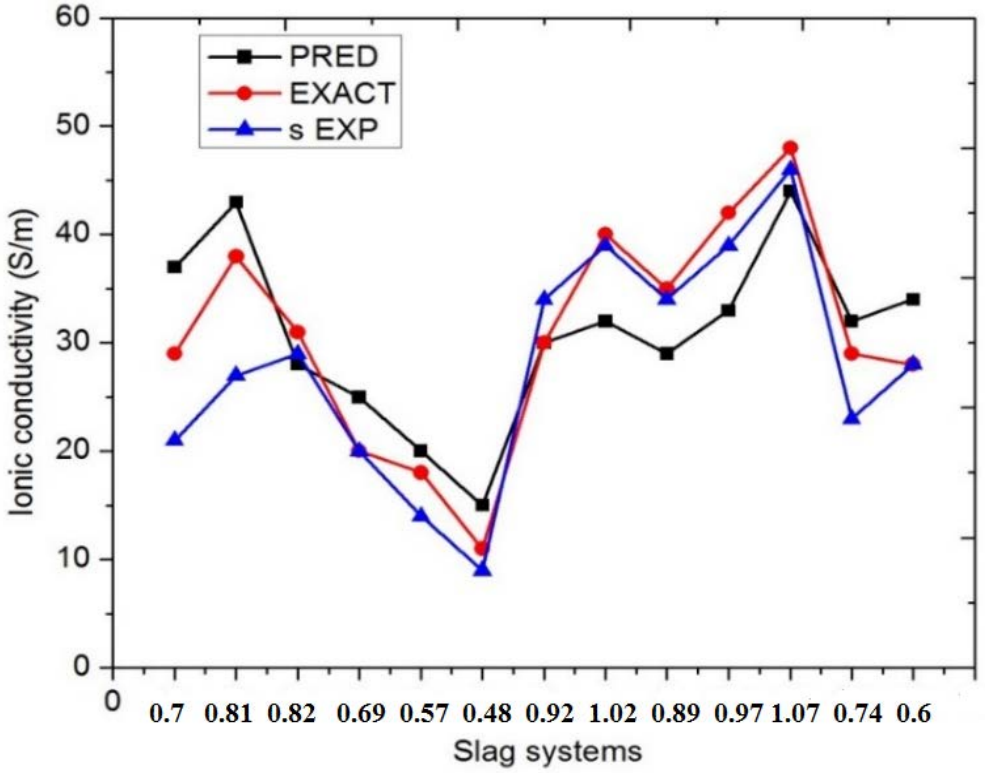

Figure 54. Electrical conductivity of slags predicted using ANN model M7 compared with MD calculated and experimentally measured electrical conductivity. Slags systems are shown in terms of basicity.

The second set of models (N*x*, *x* = 1–9, using holdout validation) developed used Al ($Q^0 - Q^4$), BO, NBO, TBO and free oxygens as input parameters. A similar construction of tested hidden neurons, as for the above discussed models, were used and are shown in Table 35. The model with the lowest MSE is N2 with an architecture of 3 and 2 hidden neurons. The MSE and correlation coefficient are 77.5 $(S/m)^2$ and 0.87, respectively, for the validation set. Applied to the validation set, as shown in Table 36 and Figure 56, the MSE and correlation coefficient are 35.2 $(S/m)^2$ and 0.88, respectively. This model has a much lower error when applied to the test set, than the M7 model, with the predicted values much closer to the MD calculated values. However, the slag systems W1, W2 and W4 still have large errors (>10%, which is less than the case for model M7, whereas the error for W6 is still in excess of 30%), whereas W7 now also deviates by more than 10%.

Table 35. Results for models optimised using Al (Q^0–Q^4), BO, NBO, TBO and free oxygen atoms as input parameters

Model	Hidden neurons	Correlation factor	MSE $(S/m)^2$
N1	1,2	0.83	173.04
N2	3,2	0.87	77.46
N3	4,3	0.87	109.12
N4	5,4	0.81	198.03
N5	6,5	0.87	102.12
N6	7,6	0.75	226.78
N7	7,4	0.85	124.86
N8	8,9	0.50	777.54
N9	9,3	0.77	191.80

Table 36. Results for models N2 electrical conductivity in (S/m)

Slag system	σ PRED	σ EXACT	% error
W6	15	11	37
W5	18	18	0
W15	28	28	0
W4	23	20	15
W1	32	29	11
W13	28	29	4
W2	43	38	13
W3	29	31	7
W10	38	35	9
W7	34	30	13
W11	38	42	10
W8	37	40	8
W12	49	48	2

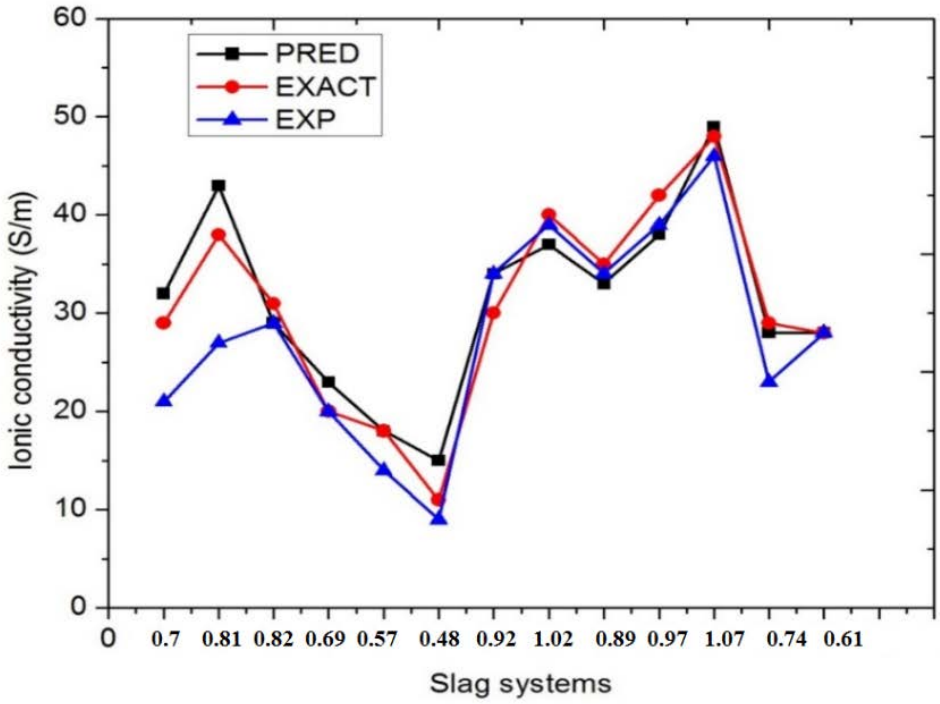

Figure 55. Electrical conductivity of slags predicted using ANN N2 compared with MD calculated and experimental measured electrical conductivity. The x-axis are presented in terms of basicity.

The third set of models (O*x*, *x* = 1–9, using holdout validation) developed had the full set of 14 input parameters, i.e., Si ($Q^0 - Q^4$), Al ($Q^0 - Q^4$), BO, NBO, TBO and free oxygens. The results for test are shown in Table 37. The MSE and the correlation coefficient are 141.4 $(S/m)^2$ and 0.80, respectively. The best model is O6 with an architecture of 7 and 6 hidden neurons. This model was also applied to the validation data. The MSE and correlation coefficient are 61 $(S/m)^2$ and 0.80, respectively, which is better than when applied to the validation set, but worse than N2 and only slightly better than M7, on average. The results are shown in Table 38 and Figure 57, respectively. For this model, the errors for W4 (>20%) and W6 (>100%) remain large, with W5 now also predicted poorly (>20%).

Table 37. Results for models optimised using Si (Q^0 – Q^4), Al (Q^0– Q^4), BO, NBO, TBO and free oxygen atoms as input parameters

Model	Hidden neurons	Correlation factor	MSE $(S/m)^2$
O1	1,2	0.75	321.0
O2	3,2	0.81	158.2
O3	4,3	0.81	151.9
O4	5,4	0.81	209.5
O5	6,5	0.77	188.8
O6	7,6	0.80	141.4
O7	7,4	0.83	147.5
O8	8,9	0.71	261.5
O9	9,3	0.78	158.5

Table 38. Results for model O6 electrical conductivity in (S/m)

Slag system	σ^{PRED}	σ^{EXACT}	% error
W6	26	11	136
W5	23	18	28
W15	28	28	0
W4	25	20	20
W1	32	29	10
W13	33	29	14
W2	40	38	5
W3	28	31	10
W10	32	35	9
W7	34	30	13
W11	38	42	10
W8	37	40	8
W12	48	48	0

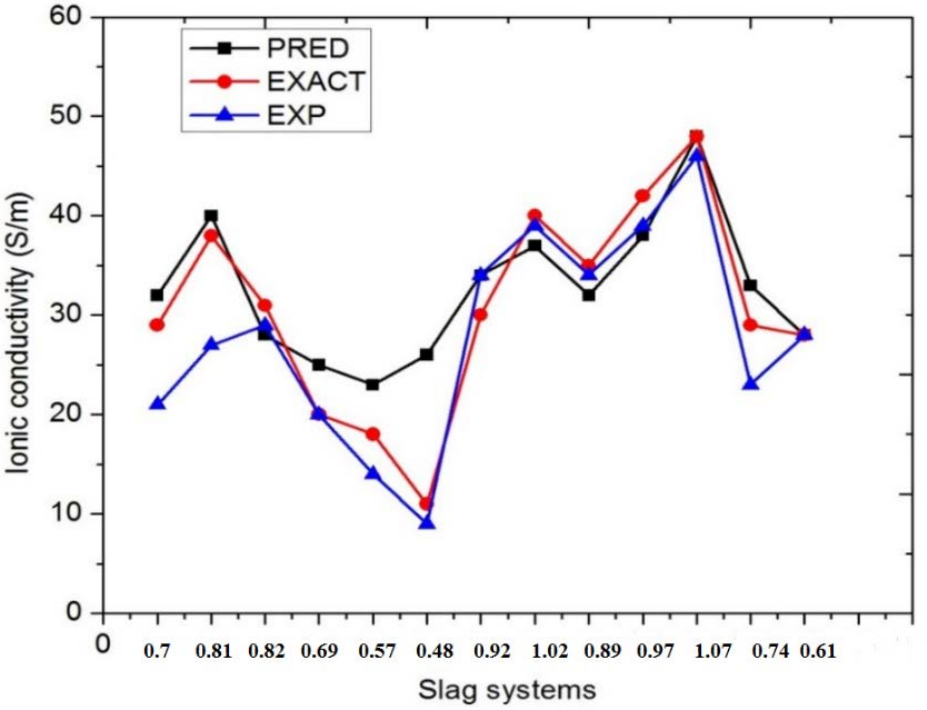

Figure 56. Electrical conductivity of slags predicted using ANN model O6, compared with MD calculated and experimental measured electrical conductivity. The x-axis are presented in terms of basicity.

In the next phase, 10-fold cross validation was used to develop a fourth model. In the ideal case (i.e., with sufficiently large and well representative training sets) the choice of validation method becomes less significant, but it was decided to test this here, where the training and holdout validation sets are of limited size.

10-fold cross-validated models with the full 14 input parameters, the same as models O1 to O9, were developed. Here, only the best model based on the lowest MSE, is reported. A (7,4) ANN gave the lowest average MSE, 328 $(S/m)^2$ with the results shown in Figure 58. Note that the error is given as an average value across all training sets in the 10-fold validation procedure. Figure 58 therefore shows a whisker plot of the statistics of this quantity. The vertical lines forming the box in the middle represent Q1 (first quartile), Q2 (median) and Q3 (third quartile) when reading the plot from left to right. The minimum and maximum values are illustrated by whiskers, which extend from the left and the right of the box.

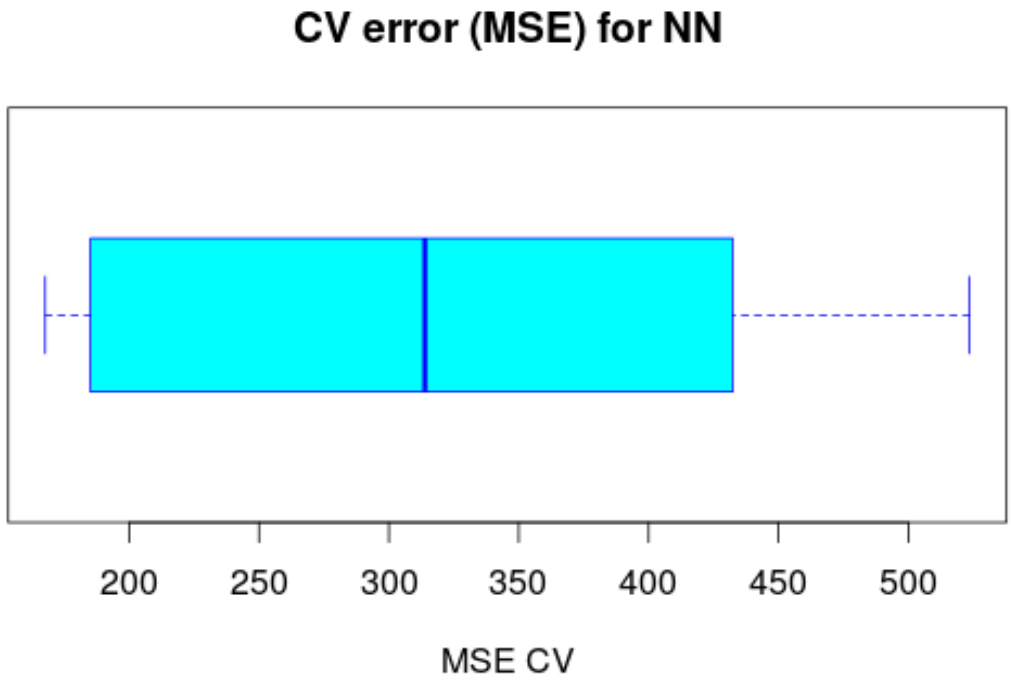

Figure 57. The number of hidden neurons which minimises the validation error $(S/m)^2$.

This model was then applied to the validation set, with the MSE again reported as an average resulting from the application of all 10 models developed in the CV phase. The results are shown in Table 39 and Figure 59. The test set MSE is 32 $(S/m)^2$ with a correlation coefficient of 0.90, which is similar to the accuracy achieved using model N2. As can be expected, this MSE is much lower than that of the 10-fold validation set, 328 $(S/m)^2$. From these results, it is clear that the model can predict the exact electrical conductivity well and that the switch to 10-fold cross validation has improved the results significantly from that achieved with holdout validation (model O6). Again, however, compositions W4 and W6 are predicted poorly, which has been the case consistently for all models developed. It should also be mentioned that the error expressed as a percentage is large, but this stems from the fact that these two compositions have the lowest (W6) and third-lowest (W4) calculated conductivity. As an absolute value, however, the error is similar to many of the other compositions.

Table 39. Results for the model optimised using Si, Al (Q^0–Q^4), BO, NBO, TBO, and free oxygen atoms as input parameters, using 10-fold cross-validation.

Slag system	σ^{PRED} (S/m)	σ^{EXACT} (S/m)	% error
W6	15	11	35
W5	19	18	7
W15	29	28	2
W4	24	20	22
W1	32	29	10
W13	29	29	0
W2	40	38	5
W3	29	31	6
W10	33	35	6
W7	33	30	10
W11	39	42	6
W8	38	40	5
W12	52	48	8

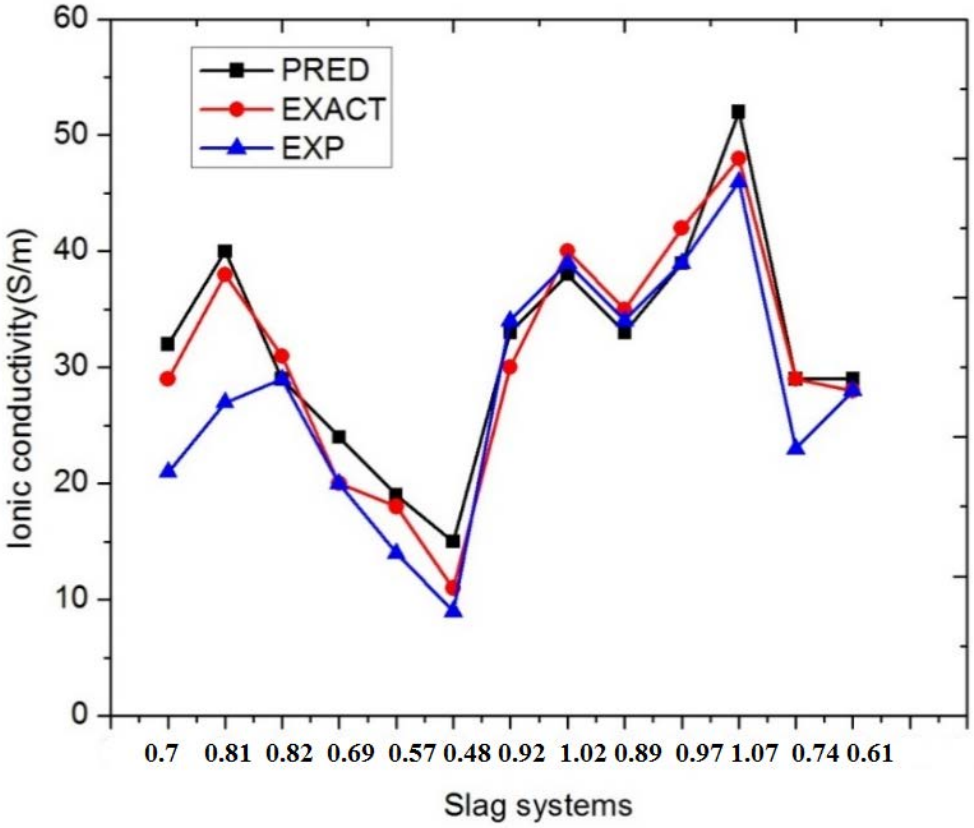

Figure 58. Electrical conductivity of slags predicted using ANN validated using a 10-fold cross validation with Si (Q^0–Q^4), Al (Q^0–Q^4), BO, NBO, TBO, and free oxygen as input parameters, with an architecture of 7 and 4 hidden neurons. The x-axis are presented in terms of basicity.

The list of the best models developed in this work are summarised in Table 40. The MSEs indicate that the model developed using all 14 parameters and 10-fold cross validation is the best, followed by model N2, M7 and O6, respectively. Using the maximum number of parameters and optimising with *k*-fold cross validation thus appears to yield the best results. It is also interesting to note that in the case of model N2, a much simpler topology of two layers with three and two hidden neurons is able to outperform the more complicated (7,6) network, O6. The results suggest that large topologies, optimized with holdout validation (M7 and O6) are less accurate, but with a switch to cross-validation for optimization (Model 4), a larger topology performs quite well.

Table 40. Summary of results for ANN models developed and discussed above. The models 1 to 4 are the best models from the first set to the fourth set, respectively. The results are for test data set.

Model	Correlation coefficient	MSE for validation set $(S/m)^2$	Hidden layers
Model 1 (M7)	0.67	66.0	7,4
Model 2 (N2)	0.88	35.2	3,2
Model 3 (O6)	0.80	61.0	7,6
Model 4	0.90	32.0	7,4

Finally, encouraged by these results, different input parameters and different topologies were explored further. Here, models fitted from the training phase were validated using the holdout procedure against 10 data points and tested against 11 data points, respectively. The latter were from the same set as before. The NN1 model was trained with 171 training data points and all other models were trained using 166 data points. Predictive capabilities and learning ability of four model constructs (i.e., with different sets of input parameters) were explored. The models developed in this work are shown in Table 41. NN1 to NN4 are four selected ANN models.

The models NN1 and NN4 have the largest correlation coefficients of 0.97, but very different MSEs, 33.7 and 6.4 $(S/m)^2$, respectively. At first glance it might therefore appear as if NN4 is thus the best model, however when it was applied on test data it performed poorly, compared to NN1, as can be seen in Table 42. The test set correlation coefficients for NN1 and NN4 are 0.98 and 0.63 with a MSE of 6.80 and 123.4 $(S/m)^2$, respectively. The NN2 and NN3 models also had high correlation coefficients of 0.91 and 0.94, respectively, and MSEs of 23.6 and

8.52 $(S/m)^2$, however both of these models performed poorly in predicting the electrical conductivities when applied to the test set. In summary then, the NN1 neural network model yielded the most encouraging results, e.g., excellent goodness-of-fit to the MD simulated conductivity, compared to the other models. The summary of predicted electrical conductivities from testing and validation phase using this model are shown in Table 43 and Figure 60 and, respectively. The architecture and weights for the NN1 model is shown in figure 61.

Table 41. Input parameters and optimized ANN models architectures developed in this work. The input parameters are Si (Q^0–Q^4), Al (Q^0–Q^4), BO, NBO, TBO, and free oxygens

Model	Hidden layers	Correlation factor	MSE $(S/m)^2$
NN1	7,4	0.97	33.7
NN2	6,4	0.91	23.6
NN3	6,4	0.94	8.52
NN4	6,4	0.97	6.4

Table 42. Input parameters, ANN model architectures and results for models shown in

Model	Hidden layers	Correlation factor	MSE$(S/m)^2$
NN1	7,4	0.98	6.8
NN2	6,4	0.87	28.4
NN3	6,4	0.84	54
NN4	6,4	0.63	123.4

Table 43. ANN predicted, MD calculated and experimental electrical conductivities (S/m)[†]

Slag system	σ^{EXP}	σ^{PRED}	σ^{EXACT}
W5	19	18	18
W15	29	26	28
W4	24	23	20
W13	29	29	29
W3	29	33	31
W10	33	35	35
W7	33	34	30
W11	39	40	42
W8	38	38	40
W12	52	48	48
N4[†]	51	48	51

[†] (Nesterenko and Khomenko 1985)

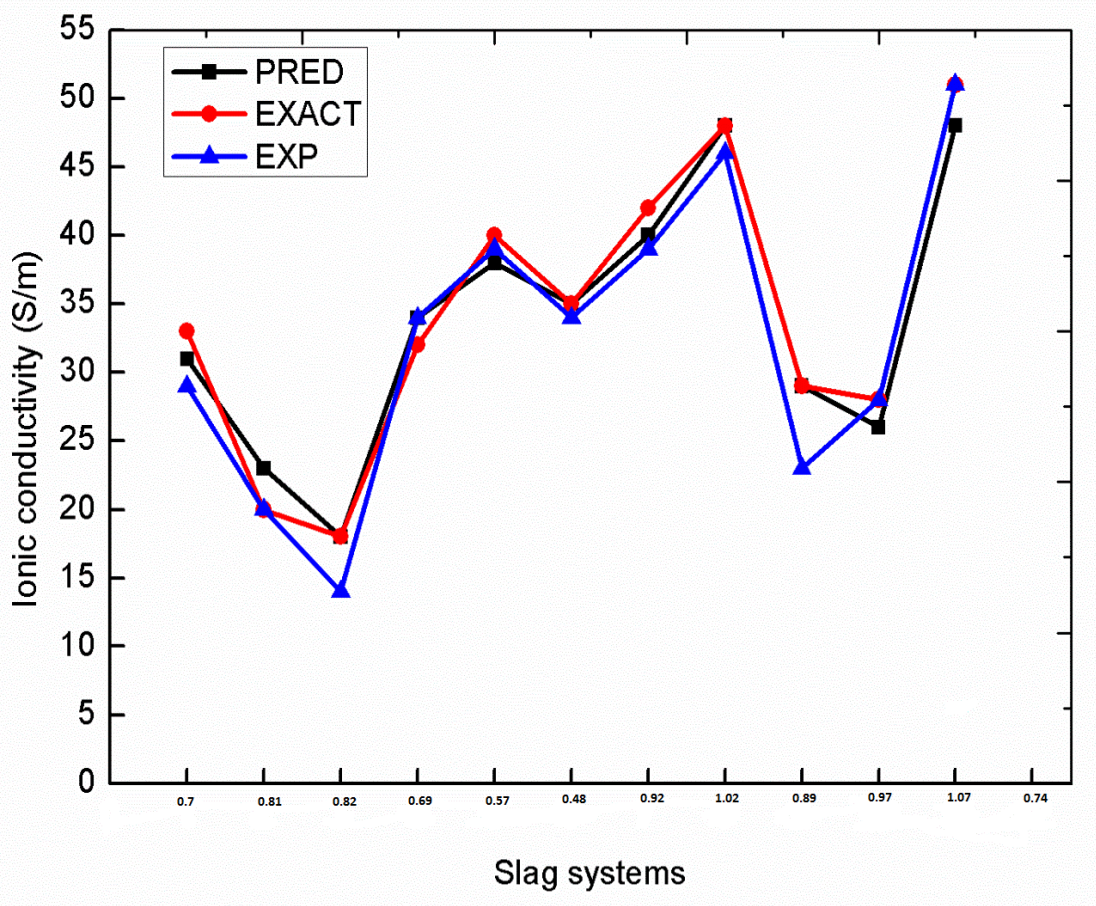

Figure 59. Electrical conductivities predicted using ANN1, MD calculated and the experimental measured conductivity. The x-axis are presented in terms of basicity.

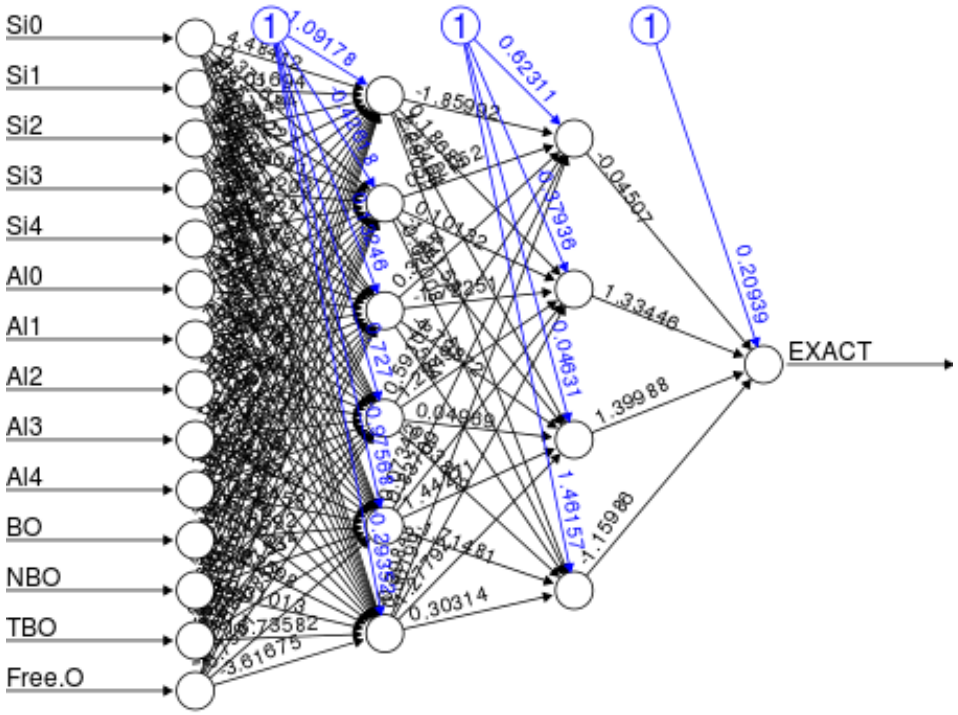

Figure 60: Example of a neural network with nine input parameters Si (Q^0 - Q^4), Al (Q^0 - Q^4), BO, NBO, TBOs and free oxygens) and one output parameter (exact conductivity), which has two hidden layers for the ANN2 model.

Models using slags from the work of Nesterenko and Khomenko (Nesterenko and Khomenko 1985) were also developed. The models are shown in Table 44 and Figures 62 – 64 in Appendix A. The developed ANN models used different system sizes and architectures and were able to predict the MD electrical conductivity with reasonable accuracy. Interestingly, the models predicts that the electrical conductivities increases with increasing basicity for all the slag systems. This is a departure from experimental measured conductivities for N7 – N9, which decrease at higher basicities.

7. CONCLUSIONS

In this work, two force fields that can be used to predict the physical properties of slag, such as densities and transport properties were first benchmarked. The Buckingham potential overestimated the density of selected compositions when compared to those simulated using a Morse type potential. The former potential also showed faster dynamics when calculating diffusion coefficients and electrical conductivities. The Morse type potential of Pedone (Pedone, Malavasi et al. 2006) was thus used throughout this work to calculate both structural and transport properties. Next, structural properties of calcium and magnesium oxide aluminosilicate slags (CMAS) were calculated using MD simulations and compared to the same properties calculated from composition data alone. The basicity was found to be a good measure of polymerisation and the number of NBO atoms increase with increasing basicity. Both the number of NBO atoms and consequently the distribution of BO atoms around a tetrahedral $[SiO_4]^{4-}$ unit, as characterised by the average *Q* distribution, can be predicted with reasonable accuracy from theoretical expressions based on the assumption that the continuous random network (CRN) Model, is applicable. However, deviations are clearly present, more so when the proportion of structure modifying Ca^{2+} and Mg^{2+} ions increase at higher basicity. An improvement in our understanding of the role of these ions is therefore necessary in order to better predict local structure. A greater number of Si–O–Al bridges, at the expense of Si–O–Si and Al–O–Al bridges, suggest that the aluminium avoidance principle is essentially satisfied in these slag systems.

The structural properties of the material, specifically the framework disorder around $[SiO_4]^{4-}$ and $[AlO_4]^{5-}$ tetrahedra, are clearly linked to the transport properties. Generally, the diffusion coefficients and electrical conductivities increase with an increasing degree of depolymerisation. Although some correlation is evident, more work is required in order to extract relationships that can be used to predict transport properties from structure. Key to this was the quantifying the role of $[AlO_5]^{7-}$, which was found to contribute up to 13% of the $[AlO_n]^{3-2n}$ units in the compositions studied here and has been shown to be important in oxygen diffusion in melts (Stebbins 1991).

It is challenging to predict a collective property, such as conductivity, from short simulations of highly viscous systems, as can be seen from the need to average over a number of simulations. The Nernst–Einstein (NE) approximation, which assumes that ions migrate independently and

requires only knowledge of diffusion coefficients, is therefore often used. Although this approximation gives the correct broad trend, care must be taken, since conductivity is usually over predicted in the process for systems similar to those considered here. It is, however, important to recognise that MD simulations, particularly here employing the potential of Pedone et al. (Pedone et al. 2006), are able to match experimental values.

Artificial neural networks models for predicting electrical conductivities were developed using the R statistical software and the `neuralnet` package. The models used slag structural properties as input parameters. The key motivators behind this choice are that structural properties should provide a unified view of slags, independent of the nature of the structure breaking cations; structural properties intrinsically respond to temperature changes and are thus more general descriptors, avoiding the need to take temperature explicitly into account; finally, some structural properties (e.g., NBO percentage) can be estimated from composition and if the ANN models were shown to be effective, could lay the foundation to also extend these models to use as input, composition data alone. Different combinations of parameters were used during model development and those that could not give accurate electrical conductivities values were eliminated. The models were further optimised by trying different number of hidden neurons, distributed into two layers. The ANN predicted results were found to be in good agreement with both the MD calculated and the experimental measured values for some of the models. However, attention needs to be paid to the quantity and accuracy of MD simulated input data. Although model development started with 14 input parameters, not all these parameters resulted in a good model, implying that not all the input parameters contribute with equal importance (and independently) to the electrical conductivities.

This study has paved the way towards further development of ANN models that can be used to predict transport properties of silicate melts without calculating them from first principles, as was done using MD simulations. It can even serve as a starting point for the development of ANNs that cover a wide range of compositions, based on the fact that structural properties of slags are related to their composition. It should be noted that these results have only been demonstrated for a limited range of compositions, i.e., CMAS systems, and further work is required to show that this approach can be extended to other more complex slag systems and also slag systems based on South African ores. Overall, it can be concluded that artificial neural network based computation holds much promise for prediction of electrical conductivities of molten slag melts. This opens possibilities for applying this technique when empirical and theoretical models are inadequate.

APPENDIX A

Table 44. Models with different architectures using Si (Q^0–Q^4), Al (Q^0–Q^4), NBO, BOs and free oxygens as input parameters

	System size	Correlations (R^2)	MSE $(S/m)^2$	HD
NE Validation set	171	0.73	129.7	6,4
NE Validation set	161	0.74	87.5	6,4
NE Validation set	161	0.68	269.6	5,4

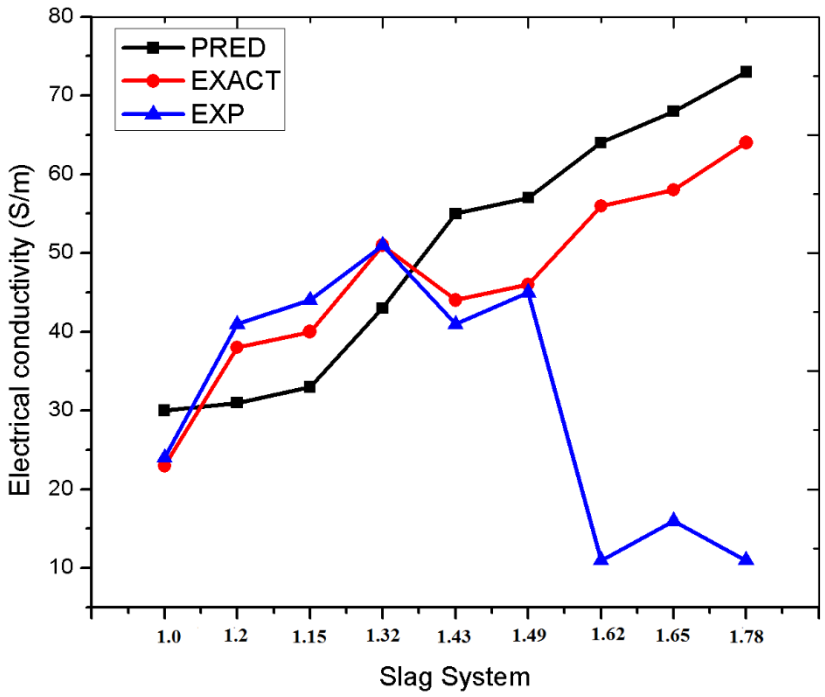

Figure 61. Electrical conductivities predicted using Si (Q^0–Q^4), Al (Q^0–Q^4), BO, NBO, TBO, and free oxygen as input parameters using 171system sizes 6 by 4 hidden layers. The x-axis are presented in terms of basicity.

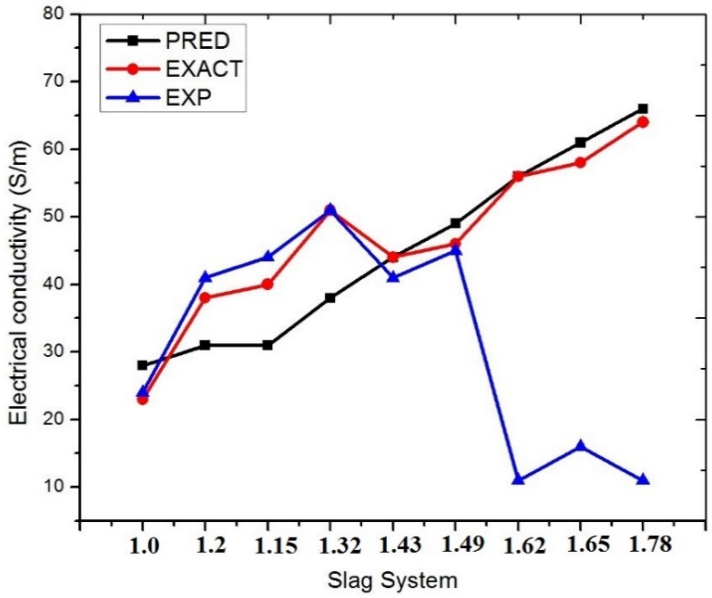

Figure 62. Electrical conductivities predicted using Si (Q^0–Q^4), Al (Q^0–Q^4), BO, NBO, TBO, and free oxygen as input parameters using 161system sizes 6 by 4 hidden layers. The x-axis are presented in terms of basicity.

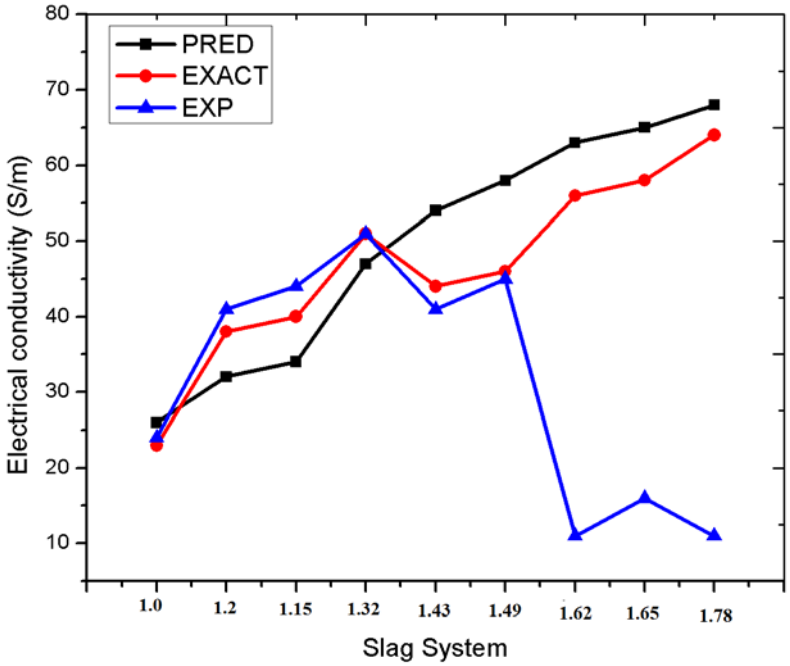

Figure 63. Electrical conductivities predicted using Si (Q^0–Q^4), Al (Q^0–Q^4), BO, NBO, TBO, and free oxygen as input parameters using 161 system sizes and 5 by 4 hidden layers. The x-axis are presented in terms of basicity.

APPENDIX B

Table 45. Slag compositions used for model development

	Number of atoms					
Slag systems	Al	Ca	Mg	Si	O	Total
M1	60	55	76	865	1951	3007
M2	120	55	76	815	1154	2220
M3	180	55	76	764	1154	2229
M4	240	55	76	713	1916	3000
M5	300	55	76	662	1904	2997
M7	420	55	76	560	1880	2991
M8	480	55	76	509	1869	2989
M9	540	55	76	458	1857	2986
M10	600	55	76	407	407	1545
M11	660	55	76	356	1833	2980
M12	720	55	76	305	1821	2977
M13	780	55	76	255	1810	2976
M14	840	55	76	204	1798	2973
M15	900	55	76	153	1786	2970
M16	960	55	76	102	1774	2967
M17	1020	55	76	51	1762	2964
M18	1080	55	76	0	1750	2961
M19	60	55	38	382	964	1499
M20	90	55	38	356	940	1479
M21	120	55	38	331	934	1478
M22	150	55	38	305	928	1476
M23	180	55	38	280	922	1475
M24	210	55	38	255	917	1475
M25	240	55	38	229	911	1473
M26	270	55	38	204	905	1472
M27	300	55	38	178	899	1470
M28	330	55	38	153	893	1469
M29	360	55	38	127	887	1467
M30	390	55	38	102	881	1466
M31	420	55	38	76	875	1464
M32	450	55	38	51	869	1463
M33	480	55	38	25	863	1461
M34	60	55	152	815	1925	3007
M35	120	55	152	764	1914	3005
M36	180	55	152	713	1902	3002
M37	240	55	152	662	1890	2999
M38	300	55	152	611	1878	2996
M39	360	55	152	560	1866	2993

M40	420	55	152	509	1855	2991
M41	480	55	152	458	1843	2988
M42	540	55	152	407	1831	2985
M43	600	55	152	356	1819	2982
M44	660	55	152	305	1807	2979
M45	720	55	152	255	1795	2977
M46	780	55	152	204	1784	2975
M47	840	55	152	153	1772	2972
M48	900	55	152	102	1760	2969
M49	960	55	152	51	1748	2966
M50	60	55	152	815	1925	3007
M51	60	55	228	764	1900	3007
M52	60	55	304	713	1874	3006
M53	60	55	379	662	1848	3004
M54	60	55	455	611	1822	3003
M55	60	55	531	560	1796	3002
M56	60	55	607	509	1770	3001
M57	60	55	683	458	1744	3000
M58	60	55	759	407	1718	2999
M59	60	55	835	356	1692	2998
M60	60	55	1063	204	1614	2996
M61	60	55	987	255	1640	2997
M62	60	55	1063	204	1614	2996
M63	60	55	1138	153	1588	2994
M64	60	55	1214	102	1562	2993
M65	60	55	1290	51	1537	2993
M66	60	109	76	815	1904	2964
M67	60	164	76	764	1857	2921
M68	60	218	76	713	1810	2877
M69	60	327	76	611	1715	2789
M70	60	327	76	611	1715	2789
M71	60	382	76	560	1668	2746
M72	60	436	76	509	1620	2701
M73	60	491	76	458	1573	2658
M74	60	545	76	407	1526	2614
M75	60	600	76	356	1479	2571
M76	60	655	76	305	1431	2527
M77	60	709	76	255	1384	2484
M78	60	764	76	204	1337	2441
M79	60	818	76	153	1290	2397
M80	60	873	76	102	1242	2353
M81	60	927	76	51	1195	2309
M82	60	982	76	0	1148	2266
M83	60	82	38	356	922	1458

M84	90	82	38	331	917	1458
M85	120	82	38	305	911	1456
M86	150	82	38	280	905	1455
M87	180	82	38	255	899	1454
M88	210	82	38	229	893	1452
M89	240	82	38	204	887	1451
M90	270	82	38	178	881	1449
M91	120	55	228	713	1888	3004
M92	180	55	228	662	1876	3001
M93	240	55	228	611	1864	2998
M94	300	55	228	560	1852	2995
M95	360	55	228	509	1840	2992
M97	480	55	228	407	1817	2987
M98	540	55	228	356	1805	2984
M99	600	55	228	305	1793	2981
M100	300	82	38	153	875	1448
M101	330	82	38	127	869	1446
M102	360	82	38	102	863	1445
M103	390	82	38	76	857	1443
M104	420	82	38	51	852	1443
M105	450	82	38	25	846	1441
M106	660	55	228	255	1781	2979
M107	720	55	228	204	1770	2977
M108	780	55	228	153	1758	2974
M109	840	55	228	102	1746	2971
M110	900	55	228	51	1734	2968
M111	0	218	76	713	1810	2817
M112	120	218	76	662	1798	2874
M113	180	218	76	611	1786	2871
M114	240	218	76	560	1774	2868
M115	300	218	76	509	1762	2865
M116	360	218	76	458	1750	2862
M117	420	218	76	407	1739	2860
M118	480	218	76	356	1727	2857
M119	540	218	76	305	1715	2854
M120	600	218	76	255	1703	2852
M121	660	218	76	204	1691	2849
M122	720	218	76	153	1680	2847
M123	780	218	76	102	1668	2844
M125	60	55	304	713	1874	3006
M126	120	55	304	662	1862	3003
M127	180	55	304	611	1850	3000
M128	240	55	304	560	1838	2997
M129	300	55	304	509	1826	2994

M130	360	55	304	458	1814	2991
M131	420	55	304	407	1803	2989
M132	480	55	304	356	1791	2986
M133	540	55	304	305	1779	2983
M134	600	55	304	255	1767	2981
M135	660	55	304	204	1755	2978
M136	720	55	304	153	1744	2976
M138	840	55	304	51	1720	2970
M139	528	30	42	56	976	1632
M140	495	30	42	84	982	1633
M141	462	30	42	112	989	1635
M142	429	30	42	140	995	1636
M143	396	30	42	168	1002	1638
M144	363	30	42	196	1008	1639
M145	330	30	42	224	1015	1641
M146	297	30	42	252	1021	1642
M147	264	30	42	280	1028	1644
M148	231	30	42	308	1034	1645
M149	198	30	42	336	1041	1647
M150	165	30	42	364	1047	1648
M151	132	30	42	392	1054	1650
M152	99	30	42	420	1060	1651
M153	66	30	42	448	1067	1653
M154	33	30	42	476	1073	1654
M155	60	273	76	662	1762	2833
M156	120	273	76	611	1750	2830
M157	180	273	76	560	1739	2828
M158	240	273	76	509	1727	2825
M159	300	273	76	458	1715	2822
M162	480	273	76	305	1680	2814
M163	540	273	76	255	1668	2812
M164	600	273	76	204	1656	2809
M165	660	273	76	153	1644	2806
M166	720	273	76	102	1632	2803
M168	60	55	379	662	1848	3004
M169	120	55	379	611	1836	3001
M170	180	55	379	560	1824	2998
M171	240	55	379	509	1812	2995
M173	360	55	379	407	1789	2990
M174	420	55	379	356	1777	2987
M175	480	55	379	305	1765	2984
M176	540	55	379	255	1753	2982
M177	600	55	379	204	1741	2979

APPENDIX C

Input files, e.g., CONFIG, CONTROL and FIELD files for each system are available electronically on request, as well as the analysis codes for calculating structural and transport properties, together with R script for model development.

Typical CONTROL files for the NPT and NVT simulations of the N1 slag system are shown below, as well as the associated FIELD file.

CONTROL FILE (NPT):

```
Slag N1
no link
integrator leapfrog
temperature      1823.00
pressure         0.001
ensemble npt ber  1.0 3.0
steps             6000000
equilibration     1000000
multiple step         1
print                100
stack                100
stats                100
rdf                   1
timestep         0.0010
cutoff           10.0
spme precision  1d-6
delr width       1.00
rvdw cutoff      10.0
print rdf
traj 1000000 1000 2
job time            600000.00
close time           36000.00
finish
```

CONTROL FILE (NVT):

```
Slag N1
no link
integrator leapfrog
temperature      1823.00
pressure         0.001
ensemble nvt nose hoover  2.0
steps             6000000
equilibration     1000000
multiple step         1
print                100
stack                100
stats                100
rdf                   1
timestep         0.0010
cutoff           10.0
```

```
spme precision  1d-6
delr width       1.00
rvdw cutoff      10.0
print rdf
traj 1000000 1000 2
job time            600000.00
close time           36000.00
finish
```

FIELD FILE:

```
Slag N1
units  eV
Molecules 5
Magnesium
nummols 72
atoms 1
Mg      24.305        1.2       1
finish
Calcium
nummols 346
atoms 1
Ca      40.078        1.2       1
finish
Silicon
nummols 396
atoms 1
Si      28.08553      2.4        1
finish
Aluminium
nummols 48
atoms 1
Al      24.134        1.8      1
finish
Oxygen
nummols 1282
atoms 1
O       15.999       -1.2       1
finish
vdw   5
Mg      O       mors   0.038908   2.586152  2.281000
Ca      O       mors   0.030211   2.92324   2.241334
Si      O       mors   0.340554   2.10000   2.006700
Al      O       mors   0.361581   2.16481   1.900442
O       O       mors   0.042395   3.61870   1.379316
close
```

REFERENCES

Adachi, A. and K. Ogino (1957). "Electrical conductivity of oxidized slags." Technology Reports of the Osaka University **7**(244): 121-126.

Agarwal, A. (2012). The flow characteristics of synthetic slags and optimizing the slag characteristics, National Institute of Technology Rourkela (BTech).

Alder, B. J. and Wainwright, T. E. (1957). "Phase Transition for a Hard Sphere System." Journal of Chemical Physics **27**(5): 1208.

Alder, B. J. and Wainwright, T. E. (1959). "Studies in Molecular Dynamics. I. General Method." Journal of Chemical Physics **31**(2): 459.

Allen, M. P. and Tildesley, D. J. (1989). Computer simulation of liquids, Oxford university press.

Arkel, A. V., Flood, E. A., and Bright, N. F. (1953). "The electrical conductivity of molten oxides." Canadian Journal of Chemistry **31**(11): 1009-1019.

Car, R. and Parrinello, M. (1985). "Unified approach for molecular dynamics and density-functional theory." Physical Review Letters **55**(22): 2471.

Bagdassarov N.S, Maumus J.É, Poe B.R, Bulatov V.K. (2004). "Pressure dependence of Tg in silicate glasses from electrical impedance measurements." Physics and Chemistry of Glasses **45**(3): 197-214.

Barczynski, R. and Murawski. L, (2002). "Mixed electronic–ionic conductivity in transition metal oxide glasses containing alkaline ions." Journal of Non-crystalline Solids **307**: 1055-1059.

Barker, K. J., Paules, J. R., Rymarchyk Jr, N., and Jancosko, R. M. (1998). "Oxygen steelmaking furnace mechanical description and maintenance considerations." The Making,

Shaping and Treating of Steel, Steelmaking and Refining Volume, Pittsburgh, PA: AISE Steel Foundation: 431-474.

Batcho, P. F., Case, D. A., & Schlick, T. (2001). "Optimized particle-mesh Ewald/multiple-time step integration for molecular dynamics simulations." Journal of Chemical Physics **115**(9): 4003.

Becker, O. M., MacKerell Jr, A. D., Roux, B., & Watanabe, M. (Eds.). (2001). Computational biochemistry and biophysics. CRC Press.

Belashchenko, D. K., Ostrovski, O. I., and Skvortsov, L. V. (2001). "Molecular dynamics simulation of binary CaO–FeO, MgO–SiO_2, FeO–SiO_2, CaO–SiO_2 and ternary CaO–FeO–SiO_2 systems." Thermochimica Acta **372**(1-2): 153-163.

Belashchenko, D. K., Ostrovski, O. I., and Saposznikova, S. Y. (1998). "Computer study of structure, thermodynamic, and electrical transport properties of Na_3AlF_6-Al_2O_3 and CaF_2-Al_2O_3 melts." Metallurgical and Materials Transactions B **29**(1): 105-110.

Benoit, M., Ispas, S., and Tuckerman, M. E. (2001). "Structural properties of molten silicates from ab initio molecular-dynamics simulations: Comparison between CaO− Al_2O_3− SiO_2 and SiO_2". Physical Review B, **64**(22), 224205.

Berendsen, H. J., Postma, J. V., van Gunsteren, W. F., DiNola, A. R. H. J., & Haak, J. R. (1984). "Molecular dynamics with coupling to an external bath." The Journal of Chemical Physics **81**(8): 3684-3690.

Birol, B., Polat, G., and Saridede, M. N. (2015). "Estimation model for electrical conductivity of molten CaF_2-Al_2O_3-CaO slags based on optical basicity." JOM, **67**(2), 427-435.

Bishop, C. M. (2006). "Pattern recognition and Machine Learning, Springer.

Biswas, R., Djomehri, M. J., Hood, R., Jin, H., Kiris, C., and Saini, S. (2005). "An application-based performance characterization of the Columbia supercluster." Proceedings of the 2005 ACM/IEEE conference on Supercomputing, IEEE Computer Society.

Bockris, J. M., Kitchener, J. A., Ignatowicz, S., and Tomlinson, J. W. (1948). "The electrical conductivity of silicate melts: systems containing Ca, Mn and Al." Discussions of the Faraday Society **4**: 265-281.

Bockris, J. M., Kitchener, J. A., Ignatowicz, S., and Tomlinson, J. W. (1952). "Electric conductance in liquid silicates." Transactions of the Faraday Society **48**: 75-91.

Car, R. and Parrinello, M. (1985). "Unified approach for molecular dynamics and density-functional theory." Physical Review Letters **55**(22): 2471.

Calas, G., Cormier, L., Galoisy, L. and Jollivet, P. (2002). "Structure–property relationships in multicomponent oxide glasses." Comptes Rendus Chimie **5**(12): 831-843.

Chakraborty, S. (1995). "Diffusion in silicate melts." Reviews in Mineralogy and Geochemistry **32**(1): 411-503.

Clay, A.T., Kuntz, C.M., Johnson, K.E. and East, A.L. (2012). "The origin of the conductivity maximum in molten salts. I. Bismuth chloride." The Journal of Chemical Physics **136**(12): 124504.

Cormack, A.N. and Cao, Y. (1996). "Molecular dynamics simulation of silicate glasses." Molecular Engineering **6**(1-2): 183-227.

Cormier, L. and Neuville, D. (2004). "Ca and Na environments in Na_2O–CaO–Al_2O_3–SiO_2 glasses: influence of cation mixing and cation-network interactions." Chemical Geology **213**(1): 103-113.

Courtial, P. and Dingwell, D. B. (1999). "Densities of melts in the CaO-MgO-Al_2O_3-SiO_2 system." American Mineralogist **84**(4): 465-476.

de Koker, N.P., Stixrude, L. and Karki, B.B. (2008). "Thermodynamics, structure, dynamics, and freezing of Mg_2SiO_4 liquid at high pressure." Geochimica et Cosmochimica Acta **72**(5): 1427-1441.

Delaye, J. M., Louis-Achille, V. and Ghaleb, D. (1997). "Modeling oxide glasses with Born–Mayer–Huggins potentials: effect of composition on structural changes." Journal of Non-crystalline Solids, **210**(2-3), 232-242.

Dickson, W. R. and E. B. Dismukes (1962). "Electrolysis of FeO-CaO-SiO_2 melts." Transactions of the Metallurgical Society of AIME **224**(3): 505.

Dingwell, D.B. and Webb, S.L. (1990). "Relaxation in silicate melts." European Journal of Mineralogy **2**(4): 427-449.

Dislich, H. (1971). "New routes to multicomponent oxide glasses." Angewandte Chemie International Edition in English **10**(6): 363-370.

Du, J. and Xiang, Y. (2012). "Effect of strontium substitution on the structure, ionic diffusion and dynamic properties of 45S5 bioactive glasses." Journal of Non-crystalline Solids, **358**(8), 1059-1071.

Duchesne, M.A., Macchi, A., Lu, D.Y., Hughes, R.W., McCalden, D. and Anthony, E.J. (2010). "Artificial neural network model to predict slag viscosity over a broad range of temperatures and slag compositions." Fuel Processing Technology **91**(8): 831-836.

Ducret, A. and W. Rankin (2002). "Liquidus temperatures and viscosities of FeO-Fe_2O_3-SiO_2-CaO-MgO slags at compositions relevant to nickel matte smelting." Scandinavian Journal of Metallurgy **31**(1): 59-67.

Dufils, T., Folliet, N., Mantisi, B., Sator, N. and Guillot, B. (2017). "Properties of magmatic liquids by molecular dynamics simulation: The example of a MORB melt." Chemical Geology **461**: 34-46.

Einstein, A. (1905). "The theory of the brownian movement." Annalen der Physik **17**: 549.

Elsafi, S. H. (2014). "Artificial neural networks (ANNs) for flood forecasting at Dongola Station in the River Nile, Sudan." Alexandria Engineering Journal **53**(3): 655-662.

Erkoç, Ş. (1997). "Empirical many-body potential energy functions used in computer simulations of condensed matter properties." Physics Reports **278**(2): 79-105.

Evans, D. J. and Holian, B. L. (1985). "The Nose–Hoover thermostat." The Journal of Chemical Physics **83**(8): 4069-4074.

Fay, H. (1966). "The electrical conductivity of liquid Al_2O_3 (molten corundum and ruby)." The Journal of Physical Chemistry **70**(3): 890-893.

Field, M.J., Bash, P.A. and Karplus, M. (1990). "A combined quantum mechanical and molecular mechanical potential for molecular dynamics simulations." Journal of Computational Chemistry **11**(6): 700-733.

Fleischer, M. (1962). Data of Geochemistry, US Govt. Printing Office.

Frauenheim, T., Seifert, G., Elsterner, M., Hajnal, Z., Jungnickel, G., Porezag, D., Suhai, S. and Scholz, R. (2000). "A self-consistent charge density-functional based tight-binding method for predictive materials simulations in physics, chemistry and biology." Physica Status Solidi (b) **217**(1): 41-62.

Frenkel, D. and Smit, B. (2001). Understanding molecular simulation: from algorithms to applications, Academic press.

Gaillard, F. (2004). "Laboratory measurements of electrical conductivity of hydrous and dry silicic melts under pressure." Earth and Planetary Science Letters **218**(1): 215-228.

Geerdes, M., Chaigneau, R. and Kurunov, I. (2015). Modern Blast Furnace Ironmaking: An Introduction, Ios Press.

Goto, K.S., Sasabe, M. and Kawakami, M. (1977). " The relationship between tracer diffusivity and electrical conductivity of multicomponent oxide slags at 900 degress to 1600 degrees C." Transactions of the Iron and Steel Institute of Japan **17**(4): 212-214.

Greaves, G. (1985). "EXAFS and the structure of glass." Journal of Non-crystalline Solids **71**(1): 203-217.

Guignard, M. and Cormier, L. (2008). "Environments of Mg and Al in $MgO–Al_2O_3–SiO_2$ glasses: A study coupling neutron and X-ray diffraction and Reverse Monte Carlo modeling." Chemical Geology **256**(3–4): 111-118.

Guillot, B. and Sator, N. (2007). "A computer simulation study of natural silicate melts. Part I: Low pressure properties." Geochimica et Cosmochimica Acta **71**(5): 1249-1265.

Haile, J. (1992). Molecular dynamics simulation, Wiley, New York.

Hansen, J. P. and McDonald, I. R. (2006). Theory of Simple Liquids, Third Edition, Academic Press.

Haven, Y. and Verkerk, B. (1965). "Diffusion and electrical conductivity of sodium ions in sodium silicate glasses." Physics and Chemistry of Glasses **6**(2): 38.

Henderson, G. S. (2005). "The structure of silicate melts: a glass perspective." The Canadian Mineralogist **43**(6): 1921-1958.

Hernández, E. R. (2008). Molecular Dynamics: from basic techniques to applications (A Molecular Dynamics Primer). AIP Conference Proceedings.

Hoover, W. G. (1985). "Canonical dynamics: Equilibrium phase-space distributions." Physical Review A **31**(3): 1695-1697.

Huaiwei, Z., Fei, S., Xiaoyan, S., Bo, Z. and Xin, H. (2012). "The Viscous and Conductivity Behavior of Melts Containing Iron Oxide in the FeO_t-SiO_2-CaO-Cu_2O System for Copper Smelting Slags." Metallurgical and Materials Transactions B **43**(5): 1046-1053.

Hundermark, R. (2003). The electrical conductivity of melter type slags, University of Cape Town (MSc).

Huang, C., and Cormack, A. N. (1991). Structural differences and phase separation in alkali silicate glasses. Journal of Chemical Physics, **95**(5), 3634-3642.

Isard, J.O. (1999). "The Haven ratio in glasses." Journal of Non-crystalline Solids **246**(1): 16-26.

Jahanshahi, L. (2004). "Recent developments in physico-chemical characterization and modelling of ferroalloy slag systems." Journal of the Southern African Institute of Mining and Metallurgy **104**(9): 529-540.

Jahn, S. and Madden, P. A. (2007). "Modeling Earth materials from crustal to lower mantle conditions: A transferable set of interaction potentials for the CMAS system." Physics of the Earth and Planetary Interiors **162**(1): 129-139.

Janežič, D., Praprotnik, M. and Merzel, F. (2005). "Molecular dynamics integration and molecular vibrational theory. I. New symplectic integrators." Journal of Chemical Physics **122**(17): 174101.

Jiao, Q. and Themelis, N. (1988). "Correlations of electrical conductivity to slag composition and temperature." Metallurgical Transactions B **19**(1): 133-140.

Jones, R.T., Reynolds, Q.G., Curr, T.R. and Sager, D., (2011). "Some myths about DC arc furnaces." Journal of the Southern African Institute of Mining and Metallurgy **111**(10): 665-674.

Jones, R. T. (2016). Fundamental aspects of alloy smelting in a DC arc furnace, University of the Witwatersrand.

Kang, Y. and Morita, K. (2006). "Thermal conductivity of the CaO-Al_2O_3-SiO_2 system." ISIJ International **46**(3): 420-426.

Keene, B.J., Mills, K.C. and Susa, M. (1995). "Slag Atlas." Dusseldorf, Germany: Verlag Stahleisen.

Kim, H., Kim, W.H., Sohn, I. and Min, D.J. (2010). "The Effect of MgO on the Viscosity of the CaO-SiO_2-20 wt% Al_2O_3-MgO Slag System." Steel Research International **81**(4): 261-264.

Kondratiev, A., Jak, E. and Hayes, P.C. (2002). "Predicting slag viscosities in metallurgical systems." JOM **54**(11): 41-45.

Köuppel, H., Domcke, W. and. Cederbaum, L. S. (1984). "Multimode Molecular Dynamics Beyond the Born-Oppenheimer Approximation." Advan ces in Chemical Physics, **57**: 59-246.

Kuo, I. F. W., Mundy, C. J., McGrath, M. J., and Siepmann, J. I. (2006). Time–dependent properties of liquid water: A comparison of Car–Parrinello and Born–Oppenheimer molecular dynamics simulations. Journal of chemical theory and computation, **2**(5), 1274-1281.

Lacks, D.J, Rear, D.B and Van Orman J.A. (2007). "Molecular dynamics investigation of viscosity, chemical diffusivities and partial molar volumes of liquids along the MgO–SiO_2 join as functions of pressure." Geochimica et Cosmochimica Acta **71**(5): 1312-1323.

Lacy, E. D. (1963). "Aluminum in glasses and melts." Physics and Chemistry of Glasses **4**(6): 234-238.

Laumonier, M., Gaillard, F., and Sifre, D. (2015). "The effect of pressure and water concentration on the electrical conductivity of dacitic melts: Implication for magnetotelluric imaging in subduction areas." Chemical Geology **418**: 66-76.

Le Claire, A. D. (1970). Physical Chemistry, Vol. 10. Solid State, Ed. W. Jost, Academic Press, New York.

Leach, A. R. (2001). Molecular modelling: principles and applications, Pearson education.

Lee, S. H., Park, D. K., and Kang, D. B. (2003). "Molecular dynamics simulations for transport

coefficients of liquid argon: new approaches." Bulletin of the Korean Chemical Society **24**(2): 178-182.

Li, Z. S. Whitwood, M., Millman, S. and van Boggelen, J. (2014). "Dissolution of lime in BOS slag: from laboratory experiment to industrial converter." Ironmaking & Steelmaking **41**(2): 112-120.

Liang, D., Yan, Z., Lv, X., Zhang, J., and Bai, C. (2017). Transition of Blast Furnace Slag from Silicate-Based to Aluminate-Based: Structure Evolution by Molecular Dynamics Simulation and Raman Spectroscopy. Metallurgical and Materials Transactions B, 48(1), 573-581.

Liang, Y., Richter, F. M., Davis, A. M., and Watson, E. B. (1996). "Diffusion in silicate melts: I. Self diffusion in CaO-Al_20_3-SiO_2 at 1500°C and 1 GPa." Geochimica et Cosmochimica Acta **60**(22): 4353-4367.

Lim, T. C. (2003). "The relationship between Lennard-Jones (12-6) and Morse potential functions." Zeitschrift für Naturforschung A **58**(11): 615-617.

Lowenstein, W. (1954). "The distribution of aluminium in the tetrahedra of silicates and aluminates." American Mineralogist **39**: 92-96.

Mackenzie, J. (1962). "Oxide Melts." Advances in Inorganic Chemistry and Radiochemistry **4**: 293-318.

Martin, A. and G. Derge (1943). "The electrical conductivity of molten blast-furnace slags." Trans. AIME **154**: 104-115.

Martínez, L., Andrade, R., Birgin, E. G., and Martínez, J. M. (2009). "PACKMOL: a package for building initial configurations for molecular dynamics simulations." Journal of Computational Chemistry **30**(13): 2157-2164.

Matsui, M. (1996). "Molecular dynamics simulation of structures, bulk moduli, and volume thermal expansivities of silicate liquids in the system CaO–MgO–Al_2O_3–SiO_2." Geophysical Research Letters **23**(4): 395-398.

Maumus, J., Bagdassarov, N., and Schmeling, H. (2005). "Electrical conductivity and partial melting of mafic rocks under pressure." Geochimica et Cosmochimica Acta **69**(19): 4703-4718.

McMillan, P. (1984). "Structural studies of silicate glasses and melts—applications and limitations of Raman spectroscopy." American Mineralogist **69**(7-8): 622-644.

McMillan, P. F. and M. C. Wilding (2009). "High pressure effects on liquid viscosity and glass transition behaviour, polyamorphic phase transitions and structural properties of glasses and liquids." Journal of Non-crystalline Solids **355**(10): 722-732.

Mills K., Hayashib, M., Wangc, L., and Watanabed, T. (2013). "The Structure and Properties of Silicate Slags." Treatise on Process Metallurgy, Volume 1: Process Fundamentals, *1*, 149.

Mills, K. (1984). "Thermal Conductivity and Heat Transfer in Coal Slags." Abstracts of papers of the American Chemical Society, American Chemical Society, Washington, DC.

Mills, K.C., Yuan, L. and Jones, R. T. (2011). "Estimating the physical properties of slags." Journal of the Southern African Institute of Mining and Metallurgy **111**(10): 649-658.

Mills, K. C. (1993). "The Influence of Structure on the Physico-chemical Properties of Slags." ISIJ International **33**(1): 148-155.

Mills, K. C. (1995). Electrical Conductivities of Molten Slags. Slag Atlas. V. D. Eisenhüttenleute. Düsseldorf, Verlag Stahleisen GmbH 580.

Mills, K. C. (2016). "Structure and properties of slags used in the continuous casting of steel: part 1 conventional mould powders." ISIJ International **56**(1): 1-13.

Monaghan, B. J., and Brooks, R. F. (2002). Thermophysical properties of slags for process control. Ironmaking & steelmaking, ***29***(2), 115-120.

Mongalo, L., Lopis, A. S., and Venter, G. A (2016). "Molecular dynamics simulations of the structural properties and electrical conductivities of CaO–MgO–Al_2O_3–SiO_2 melts." Journal of Non-Crystalline Solids **452**: 194-202.

Mori, K. and Y. Matsushita (1952). "The electrical conductivity of molten binary slags." Tetsu-to-Hagané **38**(5): 283-288.

Muhmood, L. and Seetharaman, S. (2010). "Density measurements of low silica CaO-SiO_2-Al_2O_3 slags." Metallurgical and Materials Transactions B **41**(4): 833-840.

Muller, J. and Erwee, M. (2011). "Blast furnace control using slag viscosities and liquidus temperatures with phase equilibria calculations." Southern African Pyrometallurgy **6**(9): 309.

Mysen, B. and Virgo, D. (1994). Structure and Properties of Silicate Glasses and Melts; Theories and Experiment. In Advanced Mineralogy, Springer**:** 238-254.

Mysen, B. O. (1987). "Magmatic silicate melts: Relations between bulk composition, structure and properties." Magmatic Processes: Physiochemical Principes: A volume in honor of Hatten S. Yoder, Jr.: 375-399.

Mysen, B. O. and P. Richet (2005). Silicate glasses and melts: properties and structure (Vol 10), Elsevier.

Mysen, B. O., Virgo, D., and Seifert, F. A. (1982). "The structure of silicate melts: implications for chemical and physical properties of natural magma." Reviews of Geophysics **20**(3): 353-383.

Mysen, B. O., Virgo, D., and Seifert, F. A. (1984). "Redox equilibria of iron in alkaline earth silicate melts; relationships between melt structure, oxygen fugacity, temperature and properties of iron-bearing silicate liquids." American Mineralogist **69**(9-10): 834-847.

Mysen, B. O., Virgo, D., and Seifert, F. A. (1985). "Relationships between properties and structure of aluminosilicate melts." American Mineralogist **70**(1-2): 88-105.

Navrotsky, A., Geisinger, K. L., McMillan, P., and Gibbs, G. V. (1985). "The tetrahedral framework in glasses and melts—inferences from molecular orbital calculations and implications for structure, thermodynamics, and physical properties." Physics and Chemistry of Minerals **11**(6): 284-298.

Navrotsky, A., Peraudeau, G., McMillan, P., and Coutures, J. P. (1982). "A thermochemical study of glasses and crystals along the joins silica-calcium aluminate and silica-sodium aluminate." Geochimica et Cosmochimica Acta **46**(11): 2039-2047.

Nesterenko, S. and V. Khomenko (1985). " Study of the effects of alkalis on the surface tension and the electrical conductivity of the slags of the CaO-MgO-SiO_2 system containing 5-percent Al_2O_3." Russian metallurgy **1**(2): 42-45.

Neuville, D. R., Cormier, L., Montouillout, V., and Massiot, D. (2007). "Local Al site distribution in aluminosilicate glasses by ^{27}Al MQMAS NMR." Journal of Non-crystalline Solids **353**(2): 180-184.

Neuville, D. R., Cormier, L., Flank, A. M., Briois, V., and Massiot, D. (2004). "Al speciation and Ca environment in calcium aluminosilicate glasses and crystals by Al and Ca K-edge X-ray absorption spectroscopy." Chemical Geology **213**(1–3): 153-163.

Neuville, D. R., Cormier, L., and Massiot, D. (2004). "Al environment in tectosilicate and peraluminous glasses: A 27 Al MQ-MAS NMR, Raman, and XANES investigation." Geochimica et Cosmochimica Acta **68**(24): 5071-5079.

Neuville, D. R., Cormier, L., and Massiot, D. (2006). "Al coordination and speciation in calcium aluminosilicate glasses: Effects of composition determined by ^{27}Al MQ-MAS NMR and Raman spectroscopy." Chemical Geology **229**(1): 173-185.

Neuville, D. R, Cormier L, Montouillout V, Florian P. I, Millot F. R, Rifflet J. C and Massiot D. O. (2008). "Structure of Mg-and Mg/Ca aluminosilicate glasses: ^{27}Al NMR and Raman spectroscopy investigations." American Mineralogist **93**(11-12): 1721-1731.

Nevins, D., and Spera, F. J. (1998). Molecular dynamics simulations of molten $CaAl_2Si_2O_8$: dependence of structure and properties on pressure. American Mineralogist, **83**(12), 1220-1230.

Ni, H., Hui, H. and Steinle-Neumann, G. (2015), Transport properties of silicate melts, Reviews of Geophysics, **53**(3), 715–744.

Ni, H., (2011). "Electrical conductivity of dry and hydrous $NaAlSi_3O_8$ glasses and liquids at high pressures." Contributions to Mineralogy and Petrology **162**(3): 501-513.

Oviedo, J., and Sanz, J. F. (1998). Molecular-dynamics simulations of $(NaO_2)_x(SiO_2)_{1-x}$ glasses: Relation between distribution and diffusive behavior of Na atoms. Physical Review B, **58**(14), 9047.

Panish, M.B. (1959). "The electrical conductivity of molten silica." The Journal of Physical Chemistry **63**(8): 1337-1338.

Park, J. H. (2012). "Structure–Property Correlations of $CaO–SiO_2–MnO$ Slag Derived from Raman Spectroscopy." ISIJ international **52**(9): 1627-1636.

Pedone, A., Gambuzzi, E., and Menziani, M. C. (2012). "Unambiguous Description of the Oxygen Environment in Multicomponent Aluminosilicate Glasses from 17O Solid State NMR Computational Spectroscopy." The Journal of Physical Chemistry C **116**(27): 14599-14609.

Pedone, A., Gambuzzi, E., and Menziani, M. C. (2006). "A new self-consistent empirical interatomic potential model for oxides, silicates, and silica-based glasses." The Journal of Physical Chemistry B **110**(24): 11780-11795.

Pfleiderer, P., Horbach, J., and Binder, K. (2006). "Structure and transport properties of amorphous aluminium silicates: Computer simulation studies." Chemical Geology **229**(1): 186-197.

Praprotnik, M. and D. Janezic (2005). "Molecular dynamics integration and molecular vibrational theory. II. Simulation of nonlinear molecules." The Journal of Chemical Physics

122(17): 174102.

Prikhodko, E. V., Togobitskaya, D. N., Petrov, A. F., Khamkhotko, A. F., & Grekov, S. V. (2010). "Physic-Chemical Properties Forecasting for Manganese Ferroalloy Production Slag." Metallurgical and Mining Industry, **2**, 186-192.

Rahman, A. (1964). "Correlations in the motion of atoms in liquid argon." Physical Review **136**: A405.

Rahman, A. and F. H. Stillinger (1971). "Molecular dynamics study of liquid water." The Journal of Chemical Physics **55**(7): 3336-3359.

Rapaport, D. C. (2004). The art of molecular dynamics simulation, Cambridge university press.

Reid, J. E., Suzuki, A., Funakoshi, K. I., Terasaki, H., Poe, B. T., Rubie, D. C., and Ohtani, E. (2003). "The viscosity of $CaMgSi_2O_6$ liquid at pressures up to 13GPa." Physics of the Earth and Planetary Interiors **139**(1): 45-54.

Rennie, M.S., Howat, D.D., and Jochens, P.R. (1972). Effects of chromium oxide, iron oxide, and calcium oxide on the liquidus temperature, viscosities, and electrical conductivities of slags in the system MgO-Al_2O_3-SiO_2, National Inst. for Metallurgy, Johannesburg (South Africa).

Rey-Castro, C. and L. F. Vega (2006). "Transport properties of the ionic liquid 1-ethyl-3-methylimidazolium chloride from equilibrium molecular dynamics simulation. The effect of temperature." The Journal of Physical Chemistry B **110**(29): 14426-14435.

Riebling, E. (1966). "Structure of sodium aluminosilicate melts containing at least 50 mole% SiO_2 at 1500 °C." The Journal of Chemical Physics **44**(8): 2857-2865.

Rlebling, E. (1964). Structure of magnesium aluminosilicate liquids at 1700° C." Canadian Journal of Chemistry **42**(12): 2811-2821.

Robiette, A. G. E. (1973). Electric smelting processes, Halsted Press.

Rosenqvist, T. (2004). Principles of extractive metallurgy, Tapir Academic Press.

Rydzewski, J. and W. Nowak (2016). "Molecular Dynamics Simulations of Large Systems in Electronic Excited States." Handbook of Computational Chemistry, Ed. J. Leszczynski, Springer.

Saheb, V. (2012). Studies on Blast Furnace Slag Flow Characteristics, National Institute of Technology, Rourkela (MTech).

Salanne, M., Rotenberg, B., Jahn, S., Vuilleumier, R., Simon, C., Madden, P. A. (2012). "Including many-body effects in models for ionic liquids." Theoretical Chemistry Accounts **131**(3): 1143.

Santhy, K., Sowmya, T, Sankaranarayanan, S. R. (2005). "Effect of oxygen to silicon ratio on the viscosity of metallurgical slags." ISIJ International **45**(7): 1014-1018.

Sarkar, S. (1989). "Electrical conductivity of molten high-alumina blast furnace slags." ISIJ International **29**(4): 348-351.

Schaible, M. (1999). "Empirical molecular dynamics modeling of silicon and silicon dioxide: a review." Critical Reviews in Solid State and Materials Sciences **24**(4): 265-323.

Schiefelbein, S. L. and Sadoway, D. R. (1997). "A high-accuracy, calibration-free technique for measuring the electrical conductivity of molten oxides." Metallurgical and materials transactions B **28**(6): 1141-1149.

Schulz, R., Lindner, B., Petridis, L., and Smith, J. C. (2009). "Scaling of multimillion-atom biological molecular dynamics simulation on a petascale supercomputer." Journal of Chemical Theory and Computation **5**(10): 2798-2808.

Seetharaman, S. (2005). Fundamentals of metallurgy, Elsevier.

Segers, L., Fontana, A., and Winand, R. (2013). "Electrical conductivity of molten slags of the system SiO_2–Al_2O_3–MnO–CaO–MgO." Canadian Metallurgical Quarterly.

Shackelford, J. F. and Doremus, R. H. (2008). "Ceramic and glass materials." Structure, properties and processing, Springer.

Shimoda, K., Nemoto, T., and Saito, K. (2008). "Local structure of magnesium in silicate glasses: A ^{25}Mg 3QMAS NMR study." The Journal of Physical Chemistry B **112**(22): 6747-6752.

Shimoda, K. and Saito, K. (2007). "Detailed structure elucidation of the blast furnace slag by molecular dynamics simulation." ISIJ International **47**(9): 1275-1279.

Shimoda, K., Tobu, Y., Kanehashi, K., Nemoto, T., and Saito, K. (2008). "Total understanding of the local structures of an amorphous slag: Perspective from multi-nuclear (^{29}Si, ^{27}Al, ^{17}O, ^{25}Mg, and ^{43}Ca) solid-state NMR." Journal of Non-crystalline Solids **354**(10): 1036-1043.

Shu, Q. F, Zhang, X., and Chou, K. C. (2015). "Structural viscosity model for aluminosilicate slags." Ironmaking & Steelmaking **42**(9): 641-647.

Smith, W. and Forester, T. (1996). "DL_POLY_2. 0: A general-purpose parallel molecular dynamics simulation package." Journal of Molecular Graphics **14**(3): 136-141.

Spera, F. J., Nevins, D., Ghiorso, M., and Cutler, I. (2009). "Structure, thermodynamic and transport properties of $CaAl_2Si_2O_8$ liquid. Part I: Molecular dynamics simulations." Geochimica et Cosmochimica Acta **73**(22): 6918-6936.

Sridhar, S., Afrange, O. D. C., Lörz , H. P., & Carli, R. (2000). "Break temperatures of mould fluxes and their relevance to continuous casting." Ironmaking & Steelmaking **27**(3): 238-242.

Stebbins, J. F. (1991). "NMR evidence for five-coordinated silicon in a silicate glass at atmospheric pressure." Nature **351**(6328): 638-639.

Stebbins, J. F., Kroeker, S., Lee, S. K., and Kiczenski, T. J. (2000). "Quantification of five- and six-coordinated aluminum ions in aluminosilicate and fluoride-containing glasses by high-

field, high-resolution 27 Al NMR." Journal of Non-crystalline Solids **275**(1): 1-6.

Stebbins, J. F., Lee, S. K., and Oglesby, J. V. (1999). "Al-O-Al oxygen sites in crystalline aluminates and aluminosilicate glasses: High-resolution oxygen-17 NMR results." American Mineralogist **84**(5-6): 983-986.

Stebbins, J. F. and Z. Xu (1997). "NMR evidence for excess non-bridging oxygen in an aluminosilicate glass." Nature **390**(6655): 60-62.

Stein, D. and Spera, F. (1996). "Molecular dynamics simulations of liquids and glasses in the system $NaAlSiO_4$-SiO_2: Physical properties and transport mechanisms." American Mineralogist **81**(3-4): 284-302.

Steinhauser, M. (2007). Computational multiscale modeling of fluids and solids: theory and applications, Springer Science & Business Media.

Steinhauser, M. O. and Hiermaier, S. (2009). "A review of computational methods in materials science: examples from shock-wave and polymer physics." International Journal of Molecular Sciences **10**(12): 5135-5216.

Stolwijk, N. and Obeidi, S. (2009). "Combined analysis of self-diffusion, conductivity, and viscosity data on room temperature ionic liquids." Electrochimica Acta **54**(5): 1645-1653.

Tadmor, E. B. and Miller, R. E. (2011). Modeling materials: continuum, atomistic and multiscale techniques, Cambridge University Press.

Tandia, A., Timofeev, N. T., Mauro, J. C., and Vargheese, K. D. (2011). "Defect-mediated self-diffusion in calcium aluminosilicate glasses: A molecular modeling study." Journal of Non-crystalline Solids **357**(7): 1780-1786.

Tangney, P. and Scandolo, S. (2002). "An ab initio parametrized interatomic force field for silica." The Journal of Chemical Physics **117**(19): 8898-8904.

Taniguchi, T., Okuno, M., and Matsumoto, T. (1997). "X-ray diffraction and EXAFS studies

of silicate glasses containing Mg, Ca and Ba atoms." Journal of Non-crystalline Solids **211**(1): 56-63.

R Core Team, (2013). "R: A language and environment for statistical computing."

Tikunoff, D. and Spera, F. J. (2014). "Thermal conductivity of molten and glassy $NaAlSi_3O_8$, $CaMgSi_2O_6$, and Mg_2SiO_4 by non-equilibrium molecular dynamics at elevated temperature and pressure." American Mineralogist **99**(11-12): 2328-2336.

Tilocca, A., Cormack, A. N., and de Leeuw, N. H. (2007). "The structure of bioactive silicate glasses: new insight from molecular dynamics simulations." Chemistry of Materials **19**(1): 95-103.

Toplis, M. J. and Dingwell, D. B. (2004). "Shear viscosities of CaO-Al_2O_3-SiO_2 and MgO-Al_2O_3-SiO_2 liquids: Implications for the structural role of aluminium and the degree of polymerisation of synthetic and natural aluminosilicate melts." Geochimica et Cosmochimica Acta **68**(24): 5169-5188.

Toplis, M. J., Kohn, S. C., Smith, M. E., and Poplett, I. J. (2000). "Fivefold-coordinated aluminum in tectosilicate glasses observed by triple quantum MAS NMR." American Mineralogist **85**(10): 1556-1560.

Tossell, J. and Horbach, J. (2005). "O triclusters revisited: classical MD and quantum cluster results for glasses of composition $(Al_2O_3)2(SiO_2)$." The Journal of Physical Chemistry B **109**(5): 1794-1797.

van der Spoel, D., Lindahl, E., Hess, B., Van Buuren, A. R., Apol, E., Meulenhoff, P. J., and Berendsen, H. J. (2008). Gromacs User Manual version 3.3

Van Der Colf, J. and Howat, D. D. (1979). "Viscosities, electrical resistivities, and liquidus temperatures of slags in the system CaO-MgO." Journal of the African institute of mining and metallurgy: 255.

Verlet, L. (1967). "Computer "Experiments" on Classical Fluids. I. Thermodynamical

Properties of Lennard-Jones Molecules." Physical Review **159**(1): 98-103.

Vuilleumier, R., Sator, N., and Guillot, B. (2009). "Computer modeling of natural silicate melts: What can we learn from *ab initio* simulations." Geochimica et Cosmochimica Acta **73**(20): 6313-6339.

Warren, B. and Biscob, J. (1938). "Fourier analysis of x–ray patterns of soda-silica glass." Journal of the American Ceramic Society **21**(7): 259-265.

Winkler, A., Horbach, J., Kob, W., and Binder, K. (2004). Structure and diffusion in amorphous aluminum silicate: a molecular dynamics computer simulation. The Journal of chemical physics, **120**(1), 384-393.

Winterhager, H., Greiner, L., and Kammel, R. (1966). Investigations of the density and electrical conductivity of melts in the system CaO-Al_2O_3-SiO_2 and CaO-MgO-Al_2O_3-SiO_2, Westdeutscher Verlag, Cologne.

Wright, A. C. (1994). "Neutron scattering from vitreous silica. V. The structure of vitreous silica: What have we learned from 60 years of diffraction studies?" Journal of Non-crystalline Solids **179**: 84-115.

Wright, A. C. (2014). "The Great Crystallite Versus Random Network Controversy: A Personal Perspective." International Journal of Applied Glass Science **5**(1): 31-56.

Wu, T., He, S., Liang, Y., and Wang, Q. (2015). "Molecular dynamics simulation of the structure and properties for the CaO–SiO_2 and CaO–Al_2O_3 systems." Journal of non-crystalline solids **411**(0): 145-151.

Xiang, Y. and Du, J. (2011). "Effect of strontium substitution on the structure of 45S5 bioglasses." Chemistry of Materials **23**(11): 2703-2717.

Xiang, Y., Du, J., Smedskjaer, M. M., and Mauro, J. C. (2013). Structure and properties of sodium aluminosilicate glasses from molecular dynamics simulations. The Journal of Chemical Physics, **139**(4), 044507.

Yao, T. H., He, S. P., Wu, T., and Wang, Q. (2017). Molecular dynamics simulations of microstructural properties of $CaO–SiO_2–TiO_2$ fluorine-free slag systems. Ironmaking and Steelmaking, **44**(8), 551-558.

Zachariasen, W. H. (1932). "The atomic arrangement in glass." Journal of the American Chemical Society **54**(10): 3841-3851.

Zanotto, E. D. (1992). "Crystallization of liquids and glasses." Braz. J. Phys **22**(2): 77-84.
Zarzycki, J. (1991). Glasses and the vitreous state, Cambridge University Press.

Zhang, S., Zhang, X., Peng, H., Wen, L., Qiu, G., Hu, M., and Bai, C. (2014). Structure Analysis of $CaO–SiO_2–Al_2O_3–TiO2$ Slag by Molecular Dynamics Simulation and FT-IR Spectroscopy. ISIJ International, **54**(4), 734-742.

Zhang, G.-H. and Chou, K.-C. (2013). "Influence of Al_2O_3/SiO_2 Ratio on Viscosities of $CaO–Al_2O_3–SiO_2$ Melt." ISIJ international **53**(1): 177-180.

Zhang, G. H., Chou, K. C., and Li, F. S. (2009). "A new model for evaluating the electrical conductivity of nonferrous slag." International Journal of Minerals, Metallurgy and Materials **16**(5): 500-504.

Zhang, G. H., Yan, B. J., Chou, K. C., and Li, F. S. (2011). "Relation between viscosity and electrical conductivity of silicate melts." Metallurgical and Materials Transactions B **42**(2): 261-264.

Zhang, G., Patuwo, B. E., and Hu, M. Y. (1998). "Forecasting with artificial neural networks: The state of the art." International journal of forecasting **14**(1): 35-62.

Zhang, Z. (2006). Synthesis and Characterization of MgA1ON-BN refractories, KTH (PhD).

Zhang, L., Sun, S., and Jahanshahi, S. (2001). Molecular dynamics simulations of silicate slags and slag–solid interfaces. Journal of Non-crystalline Solids, **282**(1), 24-29.

Zheng, K., Yang, F., Wang, X., and Zhang, Z. (2014). Investigation of self-diffusion and structure in calcium aluminosilicate slags by molecular dynamics simulation. Materials Sciences and Applications, **5**(02), 73.

Zhang, Y.; Ni, H.; Chen, Y., (2010). Diffusion Data in Silicate Melts. Reviews in Minerology and Geomchemistry, **72**, 311-408.